

**TOWARD THE RATIONAL DESIGN OF MULTIFUNCTIONAL  
NANOMATERIALS: SYNTHESIS AND CHARACTERIZATION OF  
FUNCTIONALIZED METAL-ORGANIC FRAMEWORKS**

A Dissertation  
Presented to  
The Academic Faculty

by

Yang Cai

In Partial Fulfillment  
of the Requirements for the Degree  
Doctorate of Philosophy in the  
School of Chemical and Biomolecular Engineering

Georgia Institute of Technology  
December 2013

**COPYRIGHT © YANG CAI 2013**

**TOWARD THE RATIONAL DESIGN OF MULTIFUNCTIONAL  
NANOMATERIALS: SYNTHESIS AND CHARACTERIZATION OF  
FUNCTIONALIZED METAL-ORGANIC FRAMEWORKS**

Approved by:

Dr. Krista S. Walton, Advisor  
School of Chemical & Biomolecular  
Engineering  
*Georgia Institute of Technology*

Dr. Carsten Sievers  
School of Chemical & Biomolecular  
Engineering  
*Georgia Institute of Technology*

Dr. David S. Sholl  
School of Chemical & Biomolecular  
Engineering  
*Georgia Institute of Technology*

Dr. Seung Soon Jang  
School of Materials Science and  
Engineering  
*Georgia Institute of Technology*

Dr. J. Carson Meredith  
School of Chemical & Biomolecular  
Engineering  
*Georgia Institute of Technology*

Date Approved: August 02, 2013

## ACKNOWLEDGEMENTS

First and foremost, I would like to express the deepest appreciation to my advisor, Associate Professor Krista S. Walton for all her help and for allowing me to transition to Georgia Tech. with her. I have been fortunate to have her as my PhD advisor. I appreciate all her contributions of time, ideas, and funding to make my Ph.D. experience productive and stimulating. The joy and enthusiasm she has for her research was contagious and motivational for me, even during tough times in the Ph.D. pursuit. I am also thankful for the excellent example she has provided as a successful woman professor. Her guidance has made this a thoughtful and rewarding journey.

I would like to thank Dr. David Sholl, Dr. Carson Meredith, Dr. Carsten Sievers and Dr. Seung Soon Jang for their support over the past three years as I moved from an idea to a completed study. I especially would like to thank Dr. Sholl for his valuable comments and suggestions.

I would like to thank Dr. Yougui Huang for their helps in solving the single crystal x-ray diffraction data for all my new crystals. I would like to acknowledge Paul Shoenecker for his help in using the Intelligent Gravimetric Analyser and the Vapor Sorption Apparatus. Dr. Yadong Zhang, (Marder Group in Chemistry and Biochemistry College of Sciences) spent countless hours for helping me with the synthesis of the organic ligands. I would like to thank Ambarish Kulkarni (Sholl Group) for his collaborative work on control of MOFs structure via functionalization in this work. Wei Mu collected the microscopy images presented in this work. I am grateful to all the present and former members of Walton Group (Dr. Yougui Huang, Dr. Bogna Brabicka,

Dr. Paul Schoenecker, Dr. Bin Mu, Dr. Jagadeswara Reddy Karra, Himanshu Jasuja, Greg Cmarik, Christine Flemming, Katrina Stults, Micheal Mangarella, Nicholas Burtch, Karen Tulig, Michael Dutzer, Yang Jiao, William Mounfield, and Ken Onubogu) for their helpful comments, discussions and encouragements during my Ph.D study. I would like to acknowledge National Science Foundation for financial support of this work.

Last but not least, I would like to thank my husband for his support in the last three years since we started our family, and my parents for giving me a constant source of love and concern all these years.

# TABLE OF CONTENTS

	Page
ACKNOWLEDGEMENTS	iv
LIST OF TABLES	xi
LIST OF FIGURES	xii
LIST OF SYMBOLS AND ABBREVIATIONS	xvii
SUMMARY	xx
 <u>CHAPTER</u>	
1 INTRODUCTION	1
1.1 Introduction to Porous Materials	2
1.1.1 Activated Carbons	2
1.1.2 Zeolites	3
1.2 Introduction to Porous Metal-Organic Frameworks	3
1.2.1 Construction of MOFs	4
1.2.2 Classification of MOFs	6
1.2.3 Synthesis Methods of MOFs	7
1.3 Potential Application of MOFs	8
1.3.1 Gas Separation in MOFs	9
1.3.2 Catalysis Application in MOFs	9
1.4 Functionalization of MOFs	10
1.4.1 Pre-functionalization of MOFs	11
1.4.2 Post-synthetic Modification of MOFs	12
1.5 Overview of This Dissertation	13
1.6 References	17

2	EXPERIMENTAL METHODS	22
2.1	Materials Characterization	22
2.1.1	Single-Crystal X-Ray Crystallography	22
2.1.2	Powder X-Ray Diffraction (pXRD)	23
2.1.3	Thermal Gravimetric Analysis	23
2.1.4	Nuclear Magnetic Resonance Spectroscopy (NMR)	24
2.1.5	Fourier Transform Infrared Spectroscopy (FTIR)	24
2.1.6	Scanning Electron Microscope (SEM)	24
2.2	Gas Adsorption Study	25
2.2.1	Specific Surface Area Characterization	25
2.2.2	Single Component Adsorption Isotherms	26
2.2.3	Water Vapor Adsorption Isotherms	26
2.3	References	27
3	SYNTHESIS OF ISOSTRUCTURAL MOFS OF HKUST-1 VIA FUNCTIONALIZATION OF ORGANIC LIGANDS	28
3.1	Introduction	28
3.2	Synthesis Results and Sample Activation	30
3.2.1	Ligands Synthesis	31
3.2.2	MOF Synthesis Procedures	34
3.2.3	Activation Procedure for MOFs	36
3.3	Thermal Gravimetric Analysis for MOFs	36
3.4	Structure Characterization of tbo Series MOFs	37
3.5	Characterization of the Functionality of MOFs	42
3.6	Surface Area Analysis of MOFs	43
3.7	Conclusions	47
3.8	References	49

4	SYNTHESIS OF ISOSTRUCTURAL CU-BTC MOFS WITH FUNCTIONALIZED ORGANIC LIGANDS	51
4.1	Introduction	51
4.2	Synthesis Results and Sample Activation	53
4.2.1	Ligands Synthesis	53
4.2.2	MOF Synthesis Procedures	56
4.2.3	Activation Procedure for MOFs	58
4.3	Thermal Gravimetric Analysis	58
4.4	Structure Characterization of fmj Series MOFs	60
4.4.1	Description of Structure for fmj Series MOFs	60
4.4.2	Characterization of the Functionality of fmj-methoxy	67
4.4.3	Characterization of Powder Form Materials	71
4.5	Surface Area Analysis of MOFs	76
4.6	Conclusions	79
4.7	References	81
5	TUNING THE GAS ADSORPTION BEHAVIOR VIA FUNCTIONALIZATION OF BTC PRECURSORS	83
5.1	Introduction	83
5.2	Experimental Details	85
5.2.1	Materials Synthesis and Activation	85
5.2.2	Experimental Methods and Procedures	85
5.3	Results and Discussion	86
5.3.1	Gas Adsorption Analysis	86
5.3.2	Heat of Adsorption	92
5.3.3	CO <sub>2</sub> /CH <sub>4</sub> Selectivity	96
5.4	Conclusions	101

5.5	References	103
6	ADJUSTING HYDROTHERMAL STABILITY VIA FUNCTIONALIZATION OF BTC PRECURSORS	107
6.1	Introduction	107
6.2	Experimental Details	108
6.2.1	Materials Synthesis and Activation	108
6.2.2	Experimental Methods and Procedures	109
6.3	Results and Discussion	109
6.3.1	Water Adsorption Measurements	109
6.3.2	Structural Stability	110
6.4	Conclusions	117
6.5	References	119
7	PURIFICATION OF MIXED-PHASE MATERIALS VIA SYNTHESIS CONDITION MODIFICATION	121
7.1	Introduction	121
7.2	Synthesis and Characterization of Multi-Phase Materials	122
7.3	Optimization of MOF Synthesis Condition	126
7.3.1	Influence of pH Value on fmj-methoxy Synthesis	126
7.3.2	Influence of Temperature on fmj-methoxy Synthesis	129
7.4	Conclusions	134
7.5	References	135
8	CONCLUSIONS AND RECOMMENDATION	137
8.1	Synthesis of Isostructural MOFs with Functionalized Organic Ligands (Chapter 3 and Chapter 4)	137
8.2	Functional Groups Effect on Gas Adsorption Isotherms (Chapter 5)	139
8.3	The Hydrothermal Stability Changes Based on the Topology (Chapter 6)	139

8.4 Optimization of fmj-methoxy Synthesis (Chapter 7)	140
8.5 References	143
APPENDIX A THE ADSORPTION PROPERTIES OF FMJ-METHOXY MATERIAL	145
Introduction	145
Adsorption Properties of fmj-methoxy	145
Conclusions	149
APPENDIX B THE FORMATION OF OTHER MOFS	150
Introduction	150
Ligands Syntheses	151
MOFs Syntheses	154
Structure Description	155
Conclusions	158
References	160
APPENDIX C RAW DATA	161
Chapter 5: Tuning the Gas Adsorption Behaviors via Functionalization of BTC Precursors	161
Chapter 6: Adjusting Hydrothermal Stability via Functionalization of BTC Precursors	181

## LIST OF TABLES

	Page
Table 3.1: Summary of Synthesis Solvents, Decomposition Temperatures and Activation Procedures of All Materials	35
Table 3.2: Observed Structure Topology, Synthesis Solvents, Accessible Surface Areas, and N <sub>2</sub> BET Surface Areas of HKUST-1 and Four Tagged HKUST-1 Materials Made with Functionalized Ligands	47
Table 4.1: Summary of Synthesis Solvents, Decomposition Temperatures and Activation Procedures of all materials	58
Table 4.2: Crystallographic Data for fmj-methoxy. <sup>a</sup> $R = \frac{\sum   F_0  -  F_c  }{\sum  F_0 }$ , <sup>b</sup> $wR = \frac{ \sum w(F_0 - F_c)^2 }{\sum w(F_0)^2}^{1/2}$	60
Table 4.3: The $\theta$ and $\phi$ Values of fmj-methyl, fmj-ethyl, and fmj-methoxy	65
Table 4.4: Observed Structure Topology, Synthesis Solvents, Accessible Surface Areas, and N <sub>2</sub> BET Surface Areas of <b>fmj</b> series MOFs	76
Table 5.1: The Ratio of Henry's Constants for CO <sub>2</sub> /CH <sub>4</sub> Binary Gas Mixture at 298, 308, and 318 K	98
Table 6.1: Accessible and BET Surface Areas Comparison Before and After Water Exposure	117
Table 7.1: BET Surface Areas of Samples under Different Synthesis Conditions	133
Table C.1: Adsorption Data for HKUST-1 CO <sub>2</sub> and CH <sub>4</sub> Isotherm at 298 K	161
Table C.2: Adsorption Data for tbo-bromo CO <sub>2</sub> and CH <sub>4</sub> Isotherm at 298 K	162
Table C.3: Adsorption Data for tbo-acetamide CO <sub>2</sub> and CH <sub>4</sub> Isotherm at 298 K	162
Table C.4: Adsorption Data for fmj-methyl CO <sub>2</sub> and CH <sub>4</sub> Isotherm at 298 K	163
Table C.5: Adsorption Data for fmj-ethyl CO <sub>2</sub> and CH <sub>4</sub> Isotherm at 298 K	164
Table C.6: Adsorption Data for fmj-methoxy CO <sub>2</sub> and CH <sub>4</sub> Isotherm at 298 K	164
Table C.7: Isothermic Heats of Adsorption Data for HKUST-1 as a Function of CO <sub>2</sub> or CH <sub>4</sub> Loading	165
Table C.8: Isothermic Heats of Adsorption Data for tbo-bromo as a Function of CO <sub>2</sub> or CH <sub>4</sub> Loading	166

Table C.9: Isothermic Heats of Adsorption Data for tbo-acetamide as a Function of CO <sub>2</sub> or CH <sub>4</sub> Loading	166
Table C.10: Isothermic Heats of Adsorption Data for fmj-methyl as a Function of CO <sub>2</sub> or CH <sub>4</sub> Loading	167
Table C.11: Isothermic Heats of Adsorption Data for fmj-ethyl as a Function of CO <sub>2</sub> or CH <sub>4</sub> Loading	168
Table C.12: Selectivity CO <sub>2</sub> :CH <sub>4</sub> Data for HKUST-1	168
Table C.13: Selectivity CO <sub>2</sub> :CH <sub>4</sub> Data for tbo-bromo	171
Table C.14: Selectivity CO <sub>2</sub> :CH <sub>4</sub> Data for tbo-acetamide	174
Table C.15: Selectivity CO <sub>2</sub> :CH <sub>4</sub> Data for fmj-methyl	176
Table C.16: Selectivity CO <sub>2</sub> :CH <sub>4</sub> Data for fmj-ethyl	179
Table C.17: Water Adsorption and Desorption Data for tbo-bromo	181
Table C.18: Water Adsorption and Desorption Data for tbo-acetamide	182
Table C.19: Water Adsorption and Desorption Data for fmj-methyl	182
Table C.20: Water Adsorption and Desorption Data for fmj-ethyl	183
Table C.21: Water Adsorption Data for fmj-methoxy	183

## LIST OF FIGURES

	Page
Figure 1.1: Neutral organic ligands	5
Figure 1.2: Anionic organic ligands	6
Figure 1.3: A general scheme illustrating the concept of post-synthetic modification of porous MOF	12
Figure 1.4: The crystal structure of HKUST-1 along the [100] direction	13
Figure 3.1: The crystal structure of HKUST-1 along the [100] direction	30
Figure 3.2: Functionalized ligands used for crystallizing functionalized HKUST-1 materials	31
Figure 3.3: Visualization of the components and crystal structure of series functionalized HKUST-1 materials under <b>tbo</b> topology (R=acetamide, bromo, or nitro)	31
Figure 3.4: Synthesis of acetamide-BTC	32
Figure 3.5: Synthesis of bromo-BTC	33
Figure 3.6: Synthesis of nitro-BTC	33
Figure 3.7: TGA curves of as-synthesized tbo-bromo, tbo-nitro, and tbo-acetamide in nitrogen flux	37
Figure 3.8: pXRD diffractograms of nitro, acetamide, bromo functionalized MOF in the <b>tbo</b> topology and comparison with parent HKUST-1	38
Figure 3.9: pXRD diffractograms of as-synthesized (top) and activated (bottom) tbo-acetamide	39
Figure 3.10: pXRD diffractograms of as-synthesized (top) and activated (bottom) tbo-bromo	40
Figure 3.11: pXRD diffractograms of as-synthesized (top) and activated (bottom) tbo-nitro	41
Figure 3.12: FTIR spectra of tbo-X (X=H, nitro, bromo, acetamide) activated at 120 <sup>0</sup> C in vacuum	42
Figure 3.13: Nitrogen isotherm of activated tbo-acetamide at 77K (closed symbols – adsorption, open symbols – desorption)	44

Figure 3.14: Nitrogen isotherm of activated tbo-bromo at 77K (closed symbols – adsorption, open symbols – desorption)	45
Figure 3.15: Nitrogen isotherm of activated tbo-nitro at 77K (closed symbols – adsorption, open symbols – desorption)	46
Figure 4.1: Functionalized ligands used for crystallizing novel functionalized CuBTC	52
Figure 4.2: Visualization of the components and crystal structure of new series CuBTC materials under the <b>fmj</b> topology	52
Figure 4.3: Synthesis of methyl-BTC	54
Figure 4.4: Synthesis of ethyl-BTC	55
Figure 4.5: Synthesis of methoxy-BTC	56
Figure 4.6: TGA curves of as-synthesized fmj-methyl, fmj-ethyl, and fmj-methoxy in nitrogen flux	59
Figure 4.7: Two different dicopper (II) tetracarboxylate building blocks of fmj-methyl	62
Figure 4.8: Secondary building unit and the view of fmj-methyl MOF in [001] direction	63
Figure 4.9: The pore structure (a) and windows (b) which make the pores form 1D channels (b) of fmj-methyl	63
Figure 4.10: View of the metal-organic frameworks fmj-ethyl(a) and fmj-methoxy(b) in the [001] direction	64
Figure 4.11: (a) Schematic of the BTC linker showing the $sp^2$ $C_1-C_2-C_3$ angle, $\theta$ (red) and carboxylate torsion angle, $\phi$ (blue). For unfunctionalized BTC linkers, X = H while for functionalized BTC linkers, X is replaced by the corresponding functional group. Representative images for secondary building units (SBU) are shown for the (b) <b>tbo</b> , (c) <b>fmj</b>	66
Figure 4.12: Polymer frameworks of fmj-methoxy viewed down the [100] (a) and [010] (b) direction	68
Figure 4.13: Comparison among simulated pXRD, experimental pXRD of bulk phase materials for fmj-methoxy before and after the modification of the synthesis condition.	69
Figure 4.14: NMR data of single crystal (a) of fmj-methoxy and powder material (b) of fmj-methoxy	70

Figure 4.15: Comparison of pXRD patterns and simulated pXRD patterns from single crystal data for as-synthesized fmj-methoxy (top), fmj-methyl (middle), and fmj-ethyl (bottom)	72
Figure 4.16: pXRD diffractograms of as-synthesized (top) and activated (bottom) fmj-methyl	73
Figure 4.17: pXRD diffractograms of as-synthesized (top) and activated (bottom) fmj-ethyl	74
Figure 4.18: pXRD diffractograms of as-synthesized (top) and activated (bottom) fmj-methoxy	75
Figure 4.19: Nitrogen isotherm of activated fmj-methyl at 77K (closed symbols – adsorption, open symbols – desorption)	77
Figure 4.20: Nitrogen isotherm of activated fmj-ethyl at 77K (closed symbols – adsorption, open symbols – desorption)	78
Figure 4.21: Nitrogen isotherm of activated fmj-methoxy at 77K (closed symbols – adsorption, open symbols – desorption)	79
Figure 5.1: CO <sub>2</sub> adsorption isotherms for samples at 25°C	88
Figure 5.2: CO <sub>2</sub> adsorption isotherms for samples at 25°C between 0-5 bar	89
Figure 5.3: CH <sub>4</sub> adsorption isotherms for samples at 25°C	91
Figure 5.4: CH <sub>4</sub> adsorption isotherms for samples at 25°C between 0-5 bar	92
Figure 5.5: Isothermic heats of adsorption as a function of CO <sub>2</sub> loading	95
Figure 5.6: Isothermic heat of adsorption as a function of CH <sub>4</sub> loading	96
Figure 5.7: Selectivity by applying IAST for a 50:50 CO <sub>2</sub> /CH <sub>4</sub> gas mixture at 25°C	100
Figure 5.8: Selectivity by applying IAST for a 5:95 CO <sub>2</sub> /CH <sub>4</sub> gas mixture at 25°C	101
Figure 6.1: Water adsorption isotherms for samples	110
Figure 6.2: pXRD Patterns for As-synthesized, Activated and After-exposure-to-water fmj-methyl Samples	112
Figure 6.3: pXRD Patterns for As-synthesized, Activated and After-exposure-to-water fmj-ethyl Samples	113
Figure 6.4: pXRD Patterns for As-synthesized, Activated and After-exposure-to-water fmj-methoxy Samples	114

Figure 6.5: pXRD Patterns for As-synthesized, Activated and After-exposure-to-water tbo-acetamide Samples	115
Figure 6.6: pXRD Patterns for As-synthesized, Activated and After-exposure-to-water tbo-bromo Samples	116
Figure 7.1: Polymer frameworks of fmj-methoxy viewed down the [100] (a) and [010] (b) direction	123
Figure 7.2: (a) Cu(HOBTC) structure unit; (b) View of layers in an ABAB manner of Cu(HOBTC)	124
Figure 7.3: Comparison between simulated pXRD of MeOCuBTC and Cu(HOBTC), and as-synthesized pXRD	125
Figure 7.4: Comparison among simulated pXRD from the fmj-methoxy and Cu(HOBTC) and as-synthesized pXRD of samples made with the different amount of 0.05 ml, 0.15 ml, and 0.25 ml 1M HCl aqueous solution at 80 °C for 72h	128
Figure 7.5: Comparison among simulated pXRD from the fmj-methoxy and Cu(HOBTC) and as-synthesized pXRD of resultant products at 70 °C, 80 °C, and 90 °C	131
Figure 7.6: NMR on as-synthesized samples before (a) and after (b) modification	132
Figure 7.7: SEM micrographs of as-synthesized samples before (a) and after (b) modification	133
Figure A.1: Isothermic heat of adsorption as a function of CO <sub>2</sub> loading including fmj-methoxy	146
Figure A.2: Isothermic heat of adsorption as a function of CH <sub>4</sub> loading including fmj-methoxy	147
Figure A.3: Selectivity by applying IAST for a 50:50 CO <sub>2</sub> /CH <sub>4</sub> gas mixture at 25°C including fmj-methoxy	148
Figure A.4: Selectivity by applying IAST for a 5:95 CO <sub>2</sub> /CH <sub>4</sub> gas mixture at 25°C including fmj-methoxy	149
Figure B.1: The structures of hydroxyl-BTC and trimethyl-BTC	151
Figure B.2: Synthesis procedure of hydroxyl-BTC	152
Figure B.3: Synthesis procedure of trimethyl-BTC	154
Figure B.4: (a) Cu(HOBTC) (or Cu(HOBTC)-2) structure unit; (b) View of layers stacked in an ABAB manner of Cu(HOBTC) (or CuHOBTC-2)	155

Figure B.5: (a) CuBrBTC structure unit; (b) View of layers stacked in an ABAB manner of CuBrBTC 156

Figure B.6: The simulated pXRD patterns for Cu(HOBTC) (top), Cu(HOBTC)-2 (middle), and CuBrBTC (bottom) 157

## LIST OF SYMBOLS AND ABBREVIATIONS

### Symbols

$n$	Integer Values
$P$	Pressure
$P_0$	Vapor Pressure
$Q_{st}$	Isosteric Heat of Adsorption
$R$	Ideal Gas Constant
$S_{i/j}$	Selectivity of Material for component $i$ over $j$
$T$	Temperature
$x_i$	Mole Fraction of $i$ in Adsorbed Phase
$y_i$	Mole Fraction of $i$ in Gas Phase
$\lambda$	Wavelength
$\mu$	Viscosity
$\nu$	Kinematic Viscosity
$\rho$	Density
$\theta$	Angle of Incidence
$\tau$	Retention Time

## Abbreviations

BDC	Benzene Dicarboxylic Acid
BET	Brunauer Emmett Teller
BTC	Benzene Tricarboxylic Acid
.cif	Crystallographic Information File
g	gram
h	Hour(s)
IAST	Ideal Adsorbed Solution Theory
IGA	Intelligent Gravimetric Adsorption
IRMOF	IsoReticular Metal-Organic Framework
K	Kelvin
kJ	kilo-Joule
m	meter
MFC	Mass-Flow Controller
min	Minute(s)
mL	Milliliter
MOF	Metal-Organic Framework
mol	gram-mole
NMR	Nuclear Magnetic Resonance
PSM	Post-Synthetic Modification
PXRD	Powder X-Ray Diffraction
%RH	Percent Relative Humidity
S.A.	Surface Area
SEM	Scanning Electron Microscopy
Vol.	Volume

XRD

X-ray Diffraction

ZIF

Zeolitic Imidazolate Framework

## SUMMARY

Metal-organic frameworks (or coordination polymers) are a recently-identified class of porous polymeric materials, consisting of metal ions or clusters linked together by organic bridging ligands. The major advantage of MOFs over other traditional materials, such as zeolites or activated carbons, is that their synthesis methods have provided an extensive class of crystalline materials with high stability, tunable metrics, and organic functionality. The ability to modify the physical environment of the pores and cavities within MOFs allow tuning of the interactions with guest species, and serves as a route to tailor the chemical stability and/or reactivity of the frameworks for specific applications.

The classical way to incorporate functional groups into a MOF is the modification of the organic precursor with specific substituents before synthesizing the MOF itself; we call this approach pre-functionalization method. Functionalization of organic precursors is the initial and necessary step to obtaining functionalized isostructural MOFs and also provides the possibility for the post-synthetic modification of MOFs. However, in some cases, the functional groups may interfere with MOF synthesis and alter the topology of desired MOF.

The goal of this proposed research is to explore the possibilities of metal-organic frameworks (MOFs) as novel porous structures, to study the effect of functional groups on the topologies and adsorption behavior of MOFs, and to understand how the synthesis conditions affect the phase purity and the in-situ reaction of ligands.

# CHAPTER 1

## INTRODUCTION

Metal-organic frameworks (MOFs) are a new class of nanoporous materials consisting of inorganic ions coordinated to organic ligands to generate robust and often porous materials.<sup>1-5</sup> Since the first report of MOFs, the fascinating properties of this new class of materials have inspired a huge variety of potential applications, such as gas storage, catalysis, separations, drug delivery, and chemical sensors.<sup>2,4,6-8</sup> The major advantage of MOFs over other traditional materials, such as zeolites or activated carbons, is that the synthesis methods provide an extensive class of crystalline materials with good stability, tunable pore sizes, and organic functionality. In order to optimize MOFs for specialized applications and maintain the structural integrity throughout the construction process, the reticular synthesis approach has been used to modify the pore size and functionality of MOFs<sup>9</sup> to perform highly specific and cooperative functions. The reticular synthesis process can be envisioned as constructing judiciously designed rigid molecular building blocks into predetermined ordered structures.

The major goal of my Ph.D. research is to synthesize functionalized novel isostructural hybrid porous materials and understand the effect of functional groups on the resulting structure and adsorption properties. With this goal in mind a comprehensive list of tasks included in this research is as follows:

1. Synthesis of a new family MOFs with tagged BTC ligands.
2. Understanding of functional groups effect on the topology and gas adsorption behavior of new materials.
3. Evaluation of the hydrothermal stability of all materials investigated.

4. Optimization of synthesis conditions to obtain the desired material.

## **1.1 Introduction of Porous Materials**

Porous materials have always attracted the attention of chemists, physicists, material scientists, and chemical engineers because they are very useful in adsorption-based gas/vapor storage and separation, shape/size-selective catalysis, and drug storage and delivery.<sup>2,10,11</sup> The porosity of these materials allows guest molecules to diffuse into the inside of the structure. Once incorporated, physical and chemical transformations of the guests may take place. According to IUPAC notation,<sup>12</sup> the pores of porous materials are classified based on the size: microporous materials have pore diameters of less than 2 nm, mesoporous materials have pore diameters between 2 nm and 50 nm, and macroporous materials have pore diameters of greater than 50 nm.

Until the mid-1990s, there were basically two types of porous materials, inorganic and carbon-based materials, which have been used commercially as adsorbents. Carbon-based materials, such as activated carbons, have been used since the start of nineteenth century for applications such as air and water purification. The classical example of inorganic porous materials is zeolite molecular sieves including aluminosilicates, aluminophosphates, and other inorganic derivatives of zeolites, which have been dominant in the adsorbent industry since the 1950s. These materials have become a technology of choice in the petroleum and chemical industry for heterogeneously catalyzed processes, and for removing heavy metals from industrial waste.

### **1.1.1 Activated Carbon**

Activated carbon<sup>13</sup> is the most widely used sorbent. It has a high open porosity and a high specific surface area, but has a disordered structure with a broad pore size

distribution. The pore structure may be pictured as having many small pores branching off from larger ones, which are open through the entire particle. The heat of adsorption of gas molecules on activated carbon is generally lower than on other sorbents. Because of its large, accessible internal surface, activated carbon adsorbs nonpolar and weakly polar organic molecules more efficiently than other sorbents do. This is because only non-specific and van der Waals forces are available as the main forces for adsorption. Despite this lack of order and strong interaction with sorbate molecules, these porous carbon materials have been used in a variety of areas, including the separation and storage of gases, the purification of water, and solvent removal and recovery.<sup>11</sup>

### **1.1.2 Zeolites**

Zeolites<sup>13</sup> are three dimensional crystalline, hydrated alkaline or alkaline-earth aluminosilicate materials. Zeolites have a high crystallinity with regular channels or cavities but a low porosity (and in some cases high surface areas). However, due to the relatively small size of the pores and limited variety of zeolite structures, the adsorption application of zeolites is obviously limited. In addition, so far only 38 natural and 194 synthetic zeolites have been identified, which limits the application of zeolites.<sup>14</sup>

## **1.2 Introduction of Porous Metal-Organic Frameworks**

It is becoming increasingly urgent to produce novel materials designed to perform highly specific and cooperative functions. The generation of MOFs have provided a significant breakthrough in this regard.<sup>2</sup> MOFs result from the reaction between organic and inorganic species in order to build up three-dimensional frameworks with backbones constructed from metal ions as nodes or connectors and organic ligands as linkers. Besides the nomenclature of ‘metal-organic frameworks (MOFs)’, this type of material

has been variously termed as coordination polymers, hybrid organic-inorganic materials and organic zeolite analogues with unavoidable overlap.<sup>15-17</sup> The solids labeled ‘MOF’ imply some characteristics, such as strong bonding providing robustness (permanent porosity), linking units that are available for modification by organic synthesis, and a geometrically well-defined structure.

The intense current research efforts towards industrial applications of MOFs bring us several characteristics in the following respects:

- (1) High surface areas (up to 6000 m<sup>2</sup>/g),<sup>18,19</sup> large pore sizes (up to 48 Å),<sup>19</sup> low densities (from 0.21 to 1.00 g/cm).
- (2) Variety of structure. The number of possibilities of combining inorganic and organic moieties is immense.<sup>5</sup>
- (3) Adjustable pore size and functionality.<sup>20-23</sup>
- (4) In spite of these important advantages, there are several crucial weaknesses in some MOFs. For the moment, only one is apparent: the weak thermal and water stability of MOFs which rules out any application at high temperature and high humidity.<sup>24-26</sup>

### **1.2.1 Construction of MOFs**

MOFs result from the coordination reaction between organic and inorganic species in order to build up three-dimensional frameworks containing metal ions as nodes or connectors and ligands as linkers. Transition metal ions are usually used as the nodes or connectors. Depending on the metal and its oxidation state, the coordination numbers of transition metal ions range from 2 to 7. The different coordination numbers can result in different geometries, such as linear, T- or Y-shaped, tetrahedral, square-planar,

trigonal-bipyramidal, and the corresponding distorted forms. Besides transition metal ions, the lanthanide ions with 7 to 12 coordination numbers also have been used to generate MOFs with the new and unusual network topologies. In some cases, some coordinated sites in metal ions are coordinated with solvent molecules.<sup>8,27,28</sup> After the removal of coordinated solvent molecules, the coordinatively unsaturated metal ion centers in the MOFs can be used in chemical adsorption, heterogeneous catalysis and sensors. There are a wide variety of choices for organic linkers. The most frequently used linkers are neutral organic ligands and anionic organic ligands,<sup>1</sup> showed in Figure 1.1 and Figure 1.2.

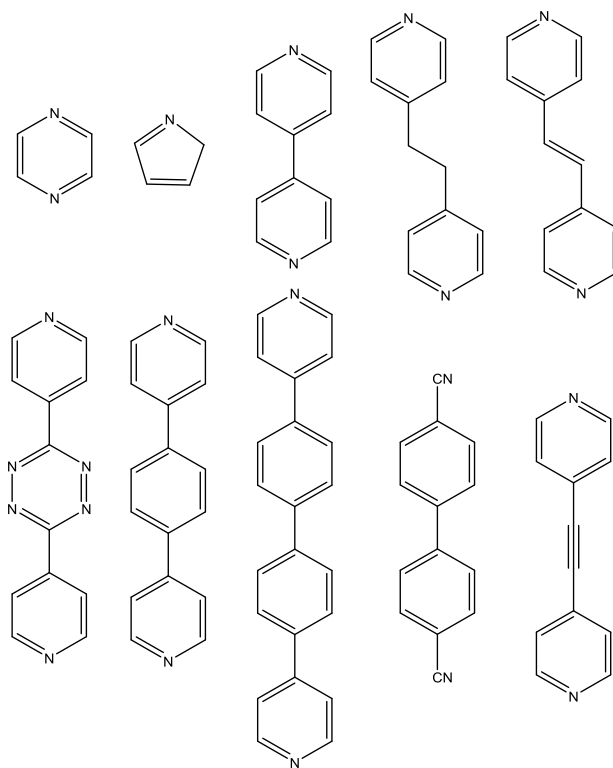


**Figure 1.1** Neutral organic ligands

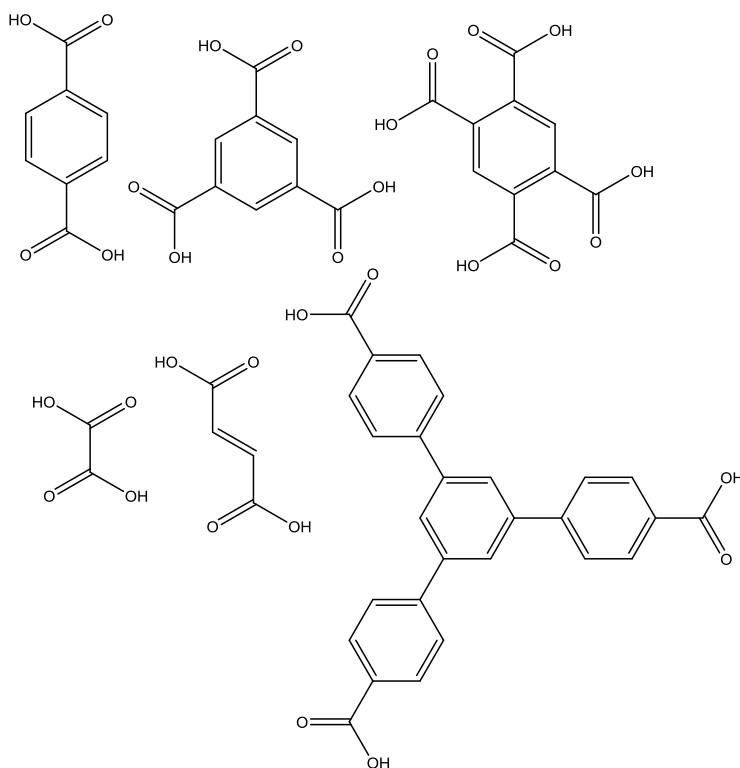


**Figure 1.2** Anionic organic ligands

### 1.2.2 Classification of MOFs

Following a suggestion in 1998, MOFs were classified in three categories,<sup>1</sup> 1st, 2nd, 3rd generation. 1st generation MOFs collapse during the extraction of guest molecules owing to the strong electrostatic host-guest interaction; 2nd generation MOFs have permanent porosity with stable and robust porous frameworks, in which the solvents have weaker interactions with the framework, and therefore can be easily removed from the structure at low temperature, often keeping the framework intact and providing a readily accessible porosity; 3rd generation have flexible and dynamic frameworks, respond to external stimuli, such as light, electric field, guest molecules and change their channels or pores reversibly.

### 1.2.3 Synthesis Methods of MOFs

There are many materials synthesis methods which have been used for MOF synthesis, including as hydro- or solvothermal synthesis under conventional oven, microwave irradiation and ultrasonic irradiation,<sup>29</sup> ionothermal synthesis,<sup>30</sup> and solvent free synthesis,<sup>31</sup> such as mechanochemical synthesis. Solvothermal synthesis under microwave irradiation (or microwave synthesis),<sup>29,30,32</sup> provides an efficient way to synthesize MOFs with short crystallization times, narrow particle size distribution, facile morphology control, and efficient evaluation of process parameters. However, the microwave method cannot be used to synthesize high quality crystals that are large enough for single crystal X-ray crystallography. Thus, it is difficult to discover novel materials using microwave synthesis methods. Mechanochemical synthesis offers a solvent-free method for the preparation of MOFs, which leads directly to products in powder form.

Other MOF synthesis techniques can also address some specific goals. However, MOFs, especially their phases having stable structures, have mainly been synthesized by solvothermal synthesis at relatively high temperatures using conventional electrical heating.<sup>1,2</sup> In solvothermal synthesis,<sup>33</sup> the metal precursors and organic ligands are typically combined in polar solvents such as water, alcohols, acetone, acetonitrile or dialkyl formamides and heated in sealed vessels such as Teflon-lined stainless steel bombs or glass vials, generating autogenous pressure. The hydro- or solvothermal synthesis method is usually utilized for the discovery of novel MOF materials. Developing new MOFs often requires a combinatorial approach, and it has often been observed that subtle changes in the compositional parameters (such as the counter ions of

metal salts, reagent concentrations, solvents, and pH) as well as process parameters (temperature, time, reaction time) can lead to poorer quality crystals, reduced yields, or the formation of entirely new phases.<sup>34-37</sup>

As mentioned above, the coordination of the metallic species and organic linkers strongly depends on the temperature of reaction. For example, seven different cobalt succinates solids were obtained under the same starting mixture and only via changing temperature.<sup>35</sup> Another example is the effect of the counter ions of metal salts on the synthesis of MOF materials. For a given system, the nature of the counter ions of metal salts also greatly influences both the nature of the resulting products and their crystal growth.<sup>37</sup> Beside temperature and the counter ions of metal salts, the other parameters, such as pH and synthetic solvents, will have a strong impact on the resulting materials, the yield, and the morphology. The synthesis condition for each MOF is an individual case that depends on the chemical nature and the acido-basic characteristics of precursors and solvents. Some effort must be expended to identify and modify synthetic conditions that allow the assembly of the building units in the intended fashion.

### **1.3 Potential Application of MOFs**

Pores are formed within MOFs upon the removal of guest or solvent molecules.<sup>38</sup> For any adsorption application, pores are advantageous for conducting host-guest chemistry such as heterogeneous catalysis, or providing strong interaction between gas molecules and the pore walls making them good candidates for gas/vapor storage and separation application.<sup>2,4,6-8</sup> Gas separations have been the target of most intense study, but recent developments in catalytic applications of MOFs have brought increased attention to this area.

### 1.3.1 Gas Separation in MOFs

Gas separation by adsorption is a very broad field. Here, particular attention is directed towards the latest developments in adsorption-based CO<sub>2</sub> separations using MOFs. Solid physical adsorbents possess significant advantages for energy efficient CO<sub>2</sub> capture compared with chemical and physical absorption approaches. For example, the separation of CO<sub>2</sub> from a low pressure gas stream through chemisorption by amines is an effective technology for removal of CO<sub>2</sub>, but amine degradation and the energy intensive nature of the regeneration process motivates the search for alternative approaches including adsorptive separation. So far, many MOF materials have been explored for applications in CO<sub>2</sub>/N<sub>2</sub> (postcombustion), CO<sub>2</sub>/H<sub>2</sub> (precombustion) or CO<sub>2</sub>/CH<sub>4</sub> (natural gas sweetening) separation. For example, the incorporation of hydroxyl functional groups into DMOF-1 induce its stronger interaction with CO<sub>2</sub> than CH<sub>4</sub>.<sup>39</sup> CO<sub>2</sub>/CH<sub>4</sub> separation selectivity in hydroxyl functionlized DMOF-1 (UTSA-25a) of 17.2 at 273 K is much higher than one of 4.4 in DMOF-1, which demonstrates the potential for UTSA-25a to be a good candidate for the industrially important separation of CO<sub>2</sub>/CH<sub>4</sub>. Couck et al. showed that the successful separation of CO<sub>2</sub>/CH<sub>4</sub> gases using amino-functionalized MIL-53 (Al), in which CO<sub>2</sub> has a high affinity for the amino groups, due to the quadruple moment of sorbent molecules.<sup>40</sup>

### 1.3.2 Catalysis in MOFs

Catalysis is potentially one of the most important applications of MOF materials, as was the case in zeolites and activated carbons. The high surface area, tunable porosity, and structure diversity of MOFs make them suitable for use as catalysts. For the catalytic applications of MOFs, there are five types of active sites: (a) metal ions or metal

cluster,<sup>41</sup> (b) functional ligands,<sup>42</sup> (c) coordinatively unsaturated metal centers,<sup>43</sup> (d) homochiral MOFs,<sup>44</sup> and (e) catalysis with dispersed metal or metal oxide nanoparticles loaded onto porous structure.<sup>45</sup> Catalytic application of MOFs is not the focus of this work, so only one example is given here. Kaskel and coworkers showed that HKUST-1 functions primarily as a Lewis acid catalyst.<sup>46,47</sup> The open Cu(II) sites of HKUST-1 were able to catalyze the cyanosilylation of benzaldehyde or acetone.

#### **1.4 Functionalization of MOFs**

MOFs represent a new direction in porous materials research that could lead to the creation of designer-specific multifunctional materials. The rich field of coordination chemistry provides a versatile platform on which these materials may be assembled using an almost infinite set of building blocks. This provides unprecedented control over pore connectivity, structure, and dimension by varying linkers, ligands, or metals in the materials. This type of “rational design” of pore structures has been elusive in the development of more traditional microporous materials. A variety of organic linker molecules and metal ions or cluster can be used to create an entire family of materials having different pore sizes and containing different chemical functionalities of the internal pore surface within the linkers but all with the same basic framework topology, to perform highly specific and cooperative functions. Two different strategies have been employed to achieve MOF functionalization. The first involves the use of functionalized ligands as the organic building block(pre-functionalization). The second approach incorporates functional groups within MOFs after the formation of MOF materials (post-synthetic modification). My work will focus on the first approach, but I will introduce the various concepts in this chapter.

### 1.4.1 Pre-functionalization of MOFs

The first strategy involves the functionalization of MOFs before synthesizing the MOF itself, called 'pre-functionalization'. The first strategy is the simplest and classic way to incorporate functional groups into a MOF, modifying the organic ligands directly with the specific substituent. Yaghi and co-workers pioneered the synthesis of cubic IRMOFs with different functional groups, and with increased dimensions.<sup>46</sup> Pre-functionalization of functional groups into organic linkers has been successfully applied to many MOF system, including UMCM-1,<sup>47</sup> UiO-66,<sup>21-23,48</sup> MIL-53,<sup>40</sup> DMOF,<sup>49</sup> and others.

The pre-functionalization of functional groups still has several challenges that must be overcome:

1. *The functional groups may interfere with the formation of the desired MOF.* The predictability associated with MOF crystal structures is complicated in situations where ligand functionalization leads to new crystal structures. In one example of this type, using the H<sub>3</sub>BTB-[MeO]<sub>3</sub> ligand and Zn(II) allows the formation of methoxy-functionalized analogue of MOF-177, while the combination of H<sub>3</sub>BTB-[OH]<sub>3</sub> and Zr(II) generate an interpenetrated framework with a different topology.<sup>50</sup>
2. *Finding the appropriate reaction conditions for forming a particular MOF with functional group is challenging.* Following the reaction conditions similar to that of MOF-5, researchers obtained doubly interpenetrated MOFs IRMOF-9, -11, and -15 by extending the linear ditopic ligands. Through the use of more dilute reaction solutions, the noninterpenetrated counterparts IRMOF-10, -12, -14 and -

16 were obtained,<sup>46</sup> which have the same topology with parent material MOF-5. Therefore, any minor changes in the synthetic conditions of MOFs can lead to different MOF structures and significant efforts must be contributed to the discovery of the appropriate synthetic condition.

### 1.4.2 Post-synthetic Modification of MOFs

Post-synthetic modification (PSM) of MOFs can be broadly defined as chemical derivation of MOFs after their formation, mostly involving covalent bond formation with the framework, generating a greater range of physical and chemical properties than could be achieved by direct synthesis alone (Figure 1.3). This approach allows access to materials containing functionalities incompatible with conventional MOF synthetic methodologies. However this approach requires that the MOFs are sufficiently robust and porous to allow late-stage transformations without compromising overall framework integrity; and it also needs specific modification sites for post-synthetic modification.

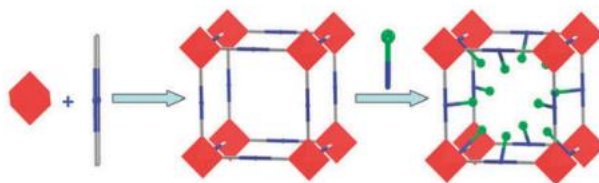


**Figure 1.3** A general scheme illustrating the concept of post-synthetic modification of porous MOF<sup>51</sup>

In principle, there exist at least two different types of post-synthetic modification of MOF materials. The first one is based on PSM of MOFs with metal-ligand interactions. PSM of HKUST-1 introduces accessible secondary amine functionalities by targeting the exposed metal sites of HKUST-1 and diamine drafting onto unsaturated

metal centers.<sup>52</sup> The second one is the covalent modification of MOFs, which is the main approach in MOF post-synthetic modification, including amide coupling, isocyanate condensations, ‘click’ chemistry and other reactions. For example, IRMOF-3,<sup>53,54</sup> HKUST-1-NH<sub>2</sub>,<sup>55</sup> DOMF-1-NH<sub>2</sub>, and UMCM-1-NH<sub>2</sub><sup>51</sup> with the presence of non-coordinating amino groups on the organic linkers, can be readily modified by linear and branched alkyl anhydrides. pXRD can be used to reveal the well-retained crystallinity.

### 1.5 Overview of This Dissertation

Since the first discovery of MOF materials, a variety of MOF structures have been synthesized and studied in the past several years. HKUST-1 (CuBTC), first reported by Chui et al.,<sup>33</sup> is one of the most widely studied MOFs. Adsorption properties of HKUST-1 for a variety of sorbate molecules have been extensively studied since the first report over a decade ago.<sup>8,56-59</sup>

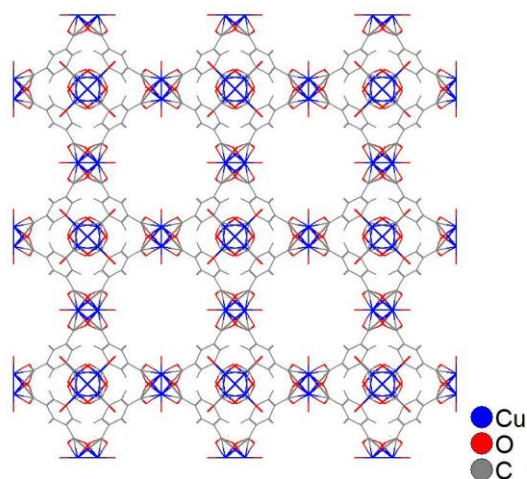


**Figure 1.4** The crystal structure of HKUST-1 along the [100] direction

The goal of this research is to explore the possibilities of HKUST-1 as a parent structure from which an isostructural family of MOFs can be created with functional

groups to attain molecule-specific adsorption properties. Three synergistic research objectives were explored to obtain the project goal: (1) synthesize a new family of MOFs based on functionalization of trimesic acid (1,3,5- benzenetricarboxylic acid, BTC) to yield structures that exhibit responsive adsorption behavior, (2) evaluate the effect of functional groups on structure and physical properties of materials, (3) assess the effect of the synthetic parameters on the formation of MOF materials.

The following work is designed to understand how functional groups affect the MOFs construction, the adsorption properties, and the MOFs stability. Chapter 2 describes the experimental methods used in this work. Single-crystal X-ray crystallography was used to obtain the MOF structures. Powder X-ray diffraction data were collected and directly compared to previously published results or simulated pXRD data from CIF files to confirm crystal structure congruency. Scanning electron microscope was used to examine the crystal morphology. Thermal gravimetric analyses were used to examine the degradation temperatures of MOF materials.

Chapter 3 shows the successful syntheses of functionalized BTC ligands with acetamide, bromo, and nitro groups and the isostructural MOFs with HKUST-1 with these tagged functional groups. Ligand structures can be confirmed by NMR test. The structure of the resulting MOFs is probed by comparing their pXRD patterns with HKUST-1 material. The chemical functionality of the isostructural MOFs can be confirmed by FTIR, thermal and structural stability is examined by using thermogravimetric analysis (TGA) and pXRD, and N<sub>2</sub> BET adsorption at 77 K was used to examine porosity.

In Chapter 4, I report the synthesis of another three functionalized BTC ligands with methyl, ethyl, and methoxy tags. Instead of forming the isostructural MOFs of HKUST-1, another new series of isostructural MOFs under **fmj** topology are synthesized, in which no material had previously observed to form this structure. Methyl-BTC, ethyl-BTC, and methoxy-BTC are confirmed by NMR test. The structures and chemical functionality of the resulting MOFs was probed by single crystal X-ray crystallographic study, pXRD, and NMR. Similar with Chapter 3, thermal and structural stability was examined using thermogravimetric analysis (TGA) and pXRD, and N<sub>2</sub> BET adsorption at 77 K was used to examine porosity.

Following the successful syntheses of the six derivatives of HKUST-1, the gas adsorption properties are investigated and reported in Chapter 5. The CO<sub>2</sub> and CH<sub>4</sub> adsorption isotherms are tested on HKUST-1, fmj-methyl, fmj-ethyl, fmj-methoxy, tbo-acetamide, and tbo-bromo. Additionally, isosteric heats of adsorption are calculated for each of the pure-component gases by using the Clausius-Clapyeron equation. Ideal selectivity is also calculated for each material based on Henry's constants and Ideal Adsorbed Solution Theory.

In Chapter 6, I focus on the hydrothermal stability of these two series of MOFs. Water adsorption isotherms are collected for each sample, and the structure crystallinity from before and after water exposure is examined via pXRD comparison. After reactivation, the porosity retention is examined via BET modeling of N<sub>2</sub> isotherms at 77 K. The **fmj** series of MOFs loss their crystallinity and porosity after water isotherm measurement, while the **tbo** series of MOFs have more stable structure which retains their crystallinity and most of the porosity.

There are multiple phases coexisting in the one-pot reaction for synthesizing fmj-methoxy. Systematic modification of synthesis parameters for fmj-methoxy materials is performed in Chapter 7 in order to obtain pure materials. The phase purity is examined via pXRD and SEM. The functionality of materials is monitored by NMR experiments.

The conclusions from specific studies presented in each chapter are summarized in Chapter 8. This work is mainly focused on the functionalization of MOF materials, and the physical and chemical properties changes via functionalization of materials. Meanwhile, the influences of the reaction conditions on MOF synthesis are examined as well. The suggestions for further work of MOFs and the difficulties for the development of MOFs are also provided, especially for the functionalization of MOFs.

## 1.6 References

- 1 Kitagawa, S., Kitaura, R. & Noro, S. Functional porous coordination polymers. *Angew. Chem. Int. Ed.* **43**, 2334-2375 (2004).
- 2 Ferey, G. Hybrid porous solids: past, present, future. *Chem. Soc. Rev.* **37**, 191-214 (2008).
- 3 James, S. L. Metal-organic frameworks. *Chem. Soc. Rev.* **32**, 276-288 (2003).
- 4 Czaja, A. U., Trukhan, N. & Muller, U. Industrial applications of metal-organic frameworks. *Chem. Soc. Rev.* **38**, 1284-1293 (2009).
- 5 Meek, S. T., Greathouse, J. A. & Allendorf, M. D. Metal-organic frameworks: a rapidly growing class of versatile nanoporous materials. *Adv. Mater.* **23**, 249-267 (2011).
- 6 Mueller, U. *et al.* Metal-organic frameworks—prospective industrial applications. *J. Mater. Chem.* **16**, 626-636 (2006).
- 7 Kuppler, R. J. *et al.* Potential applications of metal-organic frameworks. *Coord. Chem. Rev.* **253**, 3042-3066 (2009).
- 8 Wu, H. *et al.* Metal-organic frameworks with exceptionally high methane uptake: where and how is methane stored? *Chem. Eur. J.* **16**, 5205-5214 (2010).
- 9 Yaghi, O. M. *et al.* Reticular synthesis and the design of new materials. *Nature* **423**, 705-714 (2003).
- 10 Li, J. R., Kuppler, R. J. & Zhou, H. C. Selective gas adsorption and separation in metal-organic frameworks. *Chem. Soc. Rev.* **38**, 1477-1504 (2009).
- 11 Manocha, L. M. High performance carbon-carbon composites. *Sadhana* **28**, 349-358 (2003).
- 12 Rouquerol, J. *et al.* Recommendations for the characterization of porous solids (Technical Report). *Pure Appl. Chem.* **66**, 1739-1758 (1994).
- 13 Yang, R. T. *Adsorbents: fundamentals and applications*. (Wiley-Interscience, 2003).
- 14 Walton, K. S., Abney, M. B. & Douglas LeVan, M. CO<sub>2</sub> adsorption in Y and X zeolites modified by alkali metal cation exchange. *Microporous Mesoporous Mater.* **91**, 78-84 (2006).
- 15 Li, H., Eddaoudi, M., Groy, T. L. & Yaghi, O. Establishing microporosity in open metal-organic frameworks: Gas sorption isotherms for Zn (BDC)(BDC= 1, 4-benzenedicarboxylate). *J. Am. Chem. Soc.* **120**, 8571-8572 (1998).

- 16 Hagrman, P. J., Hagrman, D. & Zubieta, J. Organic–inorganic hybrid materials: from “simple” coordination polymers to organodiamine-templated molybdenum oxides. *Angew. Chem. Int. Ed.* **38**, 2638-2684 (1999).
- 17 Moulton, B. & Zaworotko, M. J. Coordination polymers: toward functional transition metal sustained materials and supermolecules: Molecular crystals. *Curr. Opin Solid State Mater. Sci.* **6**, 117-123 (2002).
- 18 Holst, J. R. & Cooper, A. I. Ultrahigh surface area in porous solids. *Adv. Mater.* **22**, 5212-5216 (2010).
- 19 Furukawa, H. *et al.* Ultrahigh porosity in metal-organic frameworks. *Science* **329**, 424-428 (2010).
- 20 Frost, H., Düren, T. & Snurr, R. Q. Effects of surface area, free volume, and heat of adsorption on hydrogen uptake in metal-organic frameworks. *J. Phys. Chem. B* **110**, 9565-9570 (2006).
- 21 Kandiah, M. *et al.* Synthesis and stability of tagged UiO-66 Zr-MOFs. *Chem. Mater.* **22**, 6632-6640 (2010).
- 22 Cmarik, G. E., Kim, M., Cohen, S. M. & Walton, K. S. Tuning the adsorption properties of UiO-66 via ligand functionalization. *Langmuir* **28**, 15606-15613 (2012).
- 23 Yang, Q. *et al.* Functionalizing porous zirconium terephthalate UiO-66(Zr) for natural gas upgrading: a computational exploration. *Chem. Commun.* **47**, 9603-9605 (2011).
- 24 Kaye, S. S., Dailly, A., Yaghi, O. M. & Long, J. R. Impact of preparation and handling on the hydrogen storage properties of  $Zn_4O(1,4\text{-benzenedicarboxylate})_3$  (MOF-5). *J. Am. Chem. Soc.* **129**, 14176-14177 (2007).
- 25 Schoenecker, P. M., Carson, C. G., Jasuja, H., Flemming, C. J. J. & Walton, K. S. Effect of water adsorption on retention of structure and surface area of metal-organic frameworks. *Ind. Eng. Chem. Res.* **51**, 6513-6519 (2012).
- 26 Greathouse, J. A. & Allendorf, M. D. The interaction of water with MOF-5 simulated by molecular dynamics. *J. Am. Chem. Soc.* **128**, 10678-10679 (2006).
- 27 Karra, J. R. & Walton, K. S. Effect of open metal sites on adsorption of polar and nonpolar molecules in metal–organic framework Cu-BTC. *Langmuir* **24**, 8620-8626 (2008).
- 28 Chen, B., Ockwig, N. W., Millward, A. R., Contreras, D. S. & Yaghi, O. M. High  $H_2$  adsorption in a microporous metal-organic framework with open metal sites. *Angew. Chem. Int. Ed.* **44**, 4745-4749 (2005).

- 29 Haque, E., Khan, N. A., Park, J. H. & Jung, S. H. Synthesis of a metal-organic framework material, iron terephthalate, by ultrasound, microwave, and conventional electric heating: a kinetic study. *Chem. Eur. J.* **16**, 1046-1052 (2010).
- 30 Lin, Z., Wragg, D. S. & Morris, R. E. Microwave-assisted synthesis of anionic metal-organic frameworks under ionothermal conditions. *Chem. Commun.*, 2021-2023 (2006).
- 31 Klimakow, M., Klobes, P., Thünemann, A. F., Rademann, K. & Emmerling, F. Mechanochemical synthesis of metal-organic frameworks: a fast and facile approach toward quantitative yields and high specific surface areas. *Chem. Mater.* **22**, 5216-5221 (2010).
- 32 Lu, C.-M., Liu, J., Xiao, K. & Harris, A. T. Microwave enhanced synthesis of MOF-5 and its CO<sub>2</sub> capture ability at moderate temperatures across multiple capture and release cycles. *Chem. Eng. J.* **156**, 465-470 (2010).
- 33 Chui, S. S. A chemically functionalizable nanoporous material [Cu<sub>3</sub>(TMA)<sub>2</sub>(H<sub>2</sub>O)<sub>3</sub>]<sub>n</sub>. *Science* **283**, 1148-1150 (1999).
- 34 Schlechte, L. *et al.* Structural diversity of cobalt(II) coordination compounds involving bent imidazole ligand: A route from 0D dimer to 3D coordination polymer. *Polyhedron* **44**, 179-186 (2012).
- 35 Forster, P. M., Burbank, A. R., Livage, C., Férey, G. & Cheetham, A. K. The role of temperature in the synthesis of hybrid inorganic-organic materials: the example of cobalt succinates. *Chem. Commun.*, 368-369 (2004).
- 36 Forster, P. M., Stock, N. & Cheetham, A. K. A high-throughput investigation of the role of pH, temperature, concentration, and time on the synthesis of hybrid inorganic-organic materials. *Angew. Chem. Int. Ed.* **44**, 7608-7611 (2005).
- 37 Biemmi, E., Christian, S., Stock, N. & Bein, T. High-throughput screening of synthesis parameters in the formation of the metal-organic frameworks MOF-5 and HKUST-1. *Microporous Mesoporous Mater.* **117**, 111-117 (2009).
- 38 Sing, K. *et al.* Physical and biophysical chemistry division commission on colloid and surface chemistry including catalysis. *Pure Appl. Chem.* **57**, 603-619 (1985).
- 39 Chen, Z. *et al.* Significantly enhanced CO<sub>2</sub>/CH<sub>4</sub> separation selectivity within a 3D prototype metal-organic framework functionalized with OH Groups on pore surfaces at room temperature. *Eur. J. Inorg. Chem.* **2011**, 2227-2231 (2011).
- 40 Couck, S. *et al.* An amine-functionalized MIL-53 metal-organic framework with large separation power for CO<sub>2</sub> and CH<sub>4</sub>. *J. Am. Chem. Soc.* **131**, 6326-6327 (2009).

- 41 Ravon, U., Domine, M. E., Gaudillere, C., Desmartin-Chomel, A. & Farrusseng, D. MOFs as acid catalysts with shape selectivity properties. *New J. Chem.* **32**, 937-940 (2008).
- 42 Hasegawa, S. *et al.* Three-dimensional porous coordination polymer functionalized with amide groups based on tridentate ligand: selective sorption and catalysis. *J. Am. Chem. Soc.* **129**, 2607-2614 (2007).
- 43 Henschel, A., Gedrich, K., Kraehnert, R. & Kaskel, S. Catalytic properties of MIL-101. *Chem. Commun.*, 4192-4194 (2008).
- 44 Hu, A., Ngo, H. L. & Lin, W. Remarkable 4,4'-Substituent effects on binap: highly enantioselective Ru catalysts for asymmetric hydrogenation of  $\beta$ -aryl ketoesters and their immobilization in room-temperature ionic liquids. *Angew. Chem. Int. Ed.* **43**, 2501-2504 (2004).
- 45 Schröder, F. *et al.* Ruthenium nanoparticles inside porous  $[\text{Zn}_4\text{O}(\text{bdc})_3]$  by hydrogenolysis of adsorbed  $[\text{Ru}(\text{cod})(\text{cot})]$ : a solid-state reference system for surfactant-stabilized ruthenium colloids. *J. Am. Chem. Soc.* **130**, 6119-6130 (2008).
- 46 Eddaoudi, M. *et al.* Systematic design of pore size and functionality in isorecticular MOFs and their application in methane storage. *Science* **295**, 469-472 (2002).
- 47 Kim, M., Boissonault, J. A., Allen, C. A., Dau, P. V. & Cohen, S. M. Functional tolerance in an isorecticular series of highly porous metal-organic frameworks. *Dalton Trans.* **41**, 6277-6282 (2012).
- 48 Huang, Y., Qin, W., Li, Z. & Li, Y. Enhanced stability and  $\text{CO}_2$  affinity of a UiO-66 type metal-organic framework decorated with dimethyl groups. *Dalton Trans.* **41**, 9283-9285 (2012).
- 49 Jasuja, H., Huang, Y.-g. & Walton, K. S. Adjusting the stability of metal-organic frameworks under humid conditions by ligand functionalization. *Langmuir* **28**, 16874-16880 (2012).
- 50 Dau, P. V., Tanabe, K. K. & Cohen, S. M. Functional group effects on metal-organic framework topology. *Chem. Commun.* **48**, 9370-9372 (2012).
- 51 Wang, Z. & Cohen, S. M. Postsynthetic modification of metal-organic frameworks. *Chem. Soc. Rev.* **38**, 1315-1329 (2009).
- 52 Ingleson, M. J., Heck, R., Gould, J. A. & Rosseinsky, M. J. Nitric oxide chemisorption in a postsynthetically modified metal-organic framework. *Inorg. Chem.* **48**, 9986-9988 (2009).
- 53 Wang, Z. & Cohen, S. M. Postsynthetic covalent modification of a neutral metal-organic framework. *J. Am. Chem. Soc.* **129**, 12368-12369 (2007).

- 54 Tanabe, K. K., Wang, Z. & Cohen, S. M. Systematic functionalization of a metal-organic framework via a postsynthetic modification approach. *J. Am. Chem. Soc.* **130**, 8508-8517 (2008).
- 55 Peikert, K., Hoffmann, F. & Froba, M. Amino substituted  $\text{Cu}_3(\text{btc})_2$ : a new metal-organic framework with a versatile functionality. *Chem. Commun.* **48**, 11196-11198 (2012).
- 56 Liu, J. *et al.*  $\text{CO}_2/\text{H}_2\text{O}$  adsorption equilibrium and rates on metal-organic frameworks: HKUST-1 and Ni/DOBDC. *Langmuir* **26**, 14301-14307 (2010).
- 57 Farrusseng, D. *et al.* Heats of adsorption for seven gases in three metal-organic frameworks: systematic comparison of experiment and simulation. *Langmuir* **25**, 7383-7388 (2009).
- 58 Guerrero, V. V., Yoo, Y., McCarthy, M. C. & Jeong, H.-K. HKUST-1 membranes on porous supports using secondary growth. *J. Mater. Chem.* **20**, 3938 (2010).
- 59 Moellmer, J., Moeller, A., Dreisbach, F., Glaeser, R. & Staudt, R. High pressure adsorption of hydrogen, nitrogen, carbon dioxide and methane on the metal-organic framework HKUST-1. *Microporous Mesoporous Mater.* **138**, 140-148 (2011).

## **CHAPTER 2**

### **EXPERIMENTAL METHODS**

#### **2.1 Material Characterization**

Single-crystal X-ray crystallography was used to obtain the MOF structures. Powder X-ray diffraction data were collected and directly compared to previously published results or simulated pXRD data from CIF files to confirm crystal structure congruency. Scanning electron microscope was used to examine the crystal morphology. Thermal gravimetric analyses were used to examine the degradation temperature of MOF materials.

##### **2.1.1 Single-crystal X-ray crystallography**

The most detailed structural information of MOF materials will be obtained from single crystal X-ray crystallography. The atoms of crystalline materials cause a beam of X-rays to diffract into many specific directions. By measuring the angles and intensities of these diffracted beams, a three-dimensional picture of the density of electrons within the crystal can be produced. From this electron density, the mean position of the atoms in the crystal can be determined, as well as their chemical bonds, their disorder and various other information. Indeed, without knowing the crystal structure, it will be quite difficult to interpret any subsequently observed properties. Therefore, synthesis in this area is strongly directed toward obtaining X-ray quality single crystals. Single-crystal XRD data of compounds in this work were collected on a single-crystal Bruker APEX CCD diffraction system with  $\text{CuK}\alpha$  radiation. The structures were solved by direct methods with the help of SHELX-97 and refined by full-matrix least-squared techniques using SHELXL-97.

### 2.1.2 Powder X-Ray Diffraction (pXRD)

Powder X-ray diffraction (pXRD) is a rapid analytical technique primarily used for phase identification of crystalline materials.<sup>1</sup> X-ray diffraction is based on constructive interference of monochromatic X-rays and a crystalline sample. The interaction of the incident rays with the sample produces constructive interference (and a diffracted ray) when conditions satisfy Bragg's Law ( $n\lambda = 2d \sin \theta$ , where  $n$  is an integer,  $\lambda$  is the wavelength of incident wave,  $d$  is the spacing between the planes in the atomic lattice, and  $\theta$  is the angle between the incident ray the scattering planes).<sup>2</sup> This law relates the wavelength of electromagnetic radiation to the diffraction angle and the lattice spacing in a crystalline sample. These diffracted X-rays are then detected, processed and counted. By scanning the sample through a range of  $2\theta$  angles, all possible diffraction directions of the lattice should be attained due to the random orientation of the powdered material. pXRD data are usually presented as a diffractogram in which the diffracted intensity  $I$  is shown as function of the scattering angle  $2\theta$ . X-ray diffraction experiments were conducted using an X'Pert pro PANalytical X-Ray Diffractometer. pXRD data were collected to verify the structures of materials. Powder X-ray diffraction analysis is also the most common method for examining the stability of a MOF. The analysis is done by performing powder X-ray diffraction experiments on the bulk materials after heating and/or evacuation, or water exposure, and comparing the result to the pXRD pattern of as-synthesized materials.

### 2.1.3 Thermal Gravimetric Analysis

Thermal gravimetric analysis (TGA) is a method of thermal analysis in which the mass of a substance is monitored as a function of temperature or time as the sample is subjected to a controlled temperature program in a controlled atmosphere.<sup>3</sup> A NETSZCH STA 449 F1 Jupiter was used to examine the thermal degradation of synthesized MOFs. Samples of ca. 10-20 mg were loaded in an alumina crucible with lid and placed on the

microbalance within the furnace. Thermogravimetry analyses (TGA) data were collected over a temperature range of 25-800 °C under N<sub>2</sub> with a heating rate of 5 °C min<sup>-1</sup>.

#### **2.1.4 Nuclear Magnetic Resonance Spectroscopy (NMR)**

Nuclear magnetic resonance spectroscopy, commonly referred to as NMR, is a preeminent technique for determining the structure of organic compounds. All NMR experiments were conducted in liquid state using Varian Mercury 300 MHz NMR spectrometer. Ligand structures can be verified by using the <sup>1</sup>H-NMR test. <sup>1</sup>H-NMR spectra for digested MOF crystals in DCl/D<sub>2</sub>O were obtained for estimation on the crystal composition. Approximately 5 mg of samples were digested by sonication in 1 ml of D<sub>2</sub>O and 100 μL DCl (35% DCl in D<sub>2</sub>O).

#### **2.1.5 Fourier Transform Infrared Spectroscopy (FTIR)**

FTIR is a technique which is used to obtain an infrared spectrum of absorption and emission of a sample. In infrared spectroscopy, IR radiation is passed through a sample. Some of the infrared radiation is absorbed by the sample and some of it is transmitted. The resulting spectrum represents the molecular absorption and transmission, creating a molecular fingerprint of the sample. Here, we use FTIR to verify the functionality of MOF surfaces. Infrared (IR) spectra were recorded with Perkin Elmer Spectrum One as a KBr pellet in range 4000-400 cm<sup>-1</sup>.

#### **2.1.6 Scanning Electron Microscope (SEM)**

A scanning electron microscope (SEM) is a type of electron microscope that produces images of a sample by scanning it with a focused beam of electrons. The electron beam is generally scanned in a raster scan pattern, and the beam's position is combined with the detected signal to produce an image. SEM can achieve resolution

better than 1 nm.<sup>4</sup> The Hitachi S-800 Field Emission Gun Scanning Electron Microscope (SEM) was used to examine crystalline morphology of MOFs materials.

## **2.2 Gas Adsorption Study**

Aside from these preliminary characterization analyses, the establishment of a material as porous requires studies of the reversible flow of guests into and out of the void volume. The measurement of nitrogen or argon isotherms has allowed the apparent surface areas of these materials to be quantified, typically assuming BET multilayer coverage. Single component gas isotherms of CO<sub>2</sub>, CH<sub>4</sub>, and N<sub>2</sub> were used to test the gas adsorption capacity of MOF materials and predict mixture adsorption behaviors. Water vapor adsorption was examined in the presence of humidity to test the water uptake and degradation of materials under humid conditions.

### **2.2.1 Specific Surface Area Characterization**

The surface area is one of the most important quantities for characterizing the porous materials. The BET analysis is the standard method for determining surface areas by applying the theory of Brunauer, Emmett, and Teller (BET) to nitrogen adsorption isotherms measured at 77K and was originally derived from multilayer gas adsorption onto flat surfaces.<sup>5</sup> The BET surface areas of MOF materials were calculated from the experimental nitrogen isotherms at 77K in the range  $0.007 < P/P_0 < 0.05$ .<sup>6</sup> The experimental surface area can be adversely affected by incomplete solvent removal or crystal collapse during activation. The accessible surface area is calculated by considering the center of mass of an adsorbate molecule rolling over the surface of the MOF, which can be used to assess the activation procedure of MOF materials.<sup>7</sup> The nitrogen adsorption isotherms were measured at 77K using a QUADRASORB<sup>TM</sup> SI volumetric analyzer manufactured by Quantachrome Instruments. Samples of ca. 20-

40mg were loaded into sample tubes and evacuated at 170 °C under  $10^{-5}$  Torr dynamic vacuum for 8h.

### **2.2.2 Single Component Adsorption Isotherms**

Single component gas isotherms were obtained using an Intelligent Gravimetric Analyser (IGA-001) from Hiden Isochema, which uses the gravimetric technique to study general gas sorption processes from vacuum to high pressure. Each adsorption/desorption step was allowed to approach equilibrium over a period of 20-30minutes.

### **2.2.3 Water Vapor Adsorption Isotherms**

Water vapor adsorption isotherms were collected using an IGA-003, which was designed to study multi-component gas and/or vapor sorption processes. The system incorporates a multiple inlet mass flow control system which can control the composition of the gases and the concentration of a vapor generated in the vapor generator.

## 2.3 References

- 1 Cullity, B. D. & Stock, S. R. *Elements of x-ray diffraction*. (Prentice Hall, 2001).
- 2 Bragg, W. L. The structure of some crystals as indicated by their diffraction of X-rays. *Proceedings of the Royal Society of London. Series A, Containing Papers of a Mathematical and Physical Character* **89**, 248-277 (1913).
- 3 Coats, A. W. & Redfern, J. P. Thermogravimetric analysis. A review. *Analyst* **88**, 906-924 (1963).
- 4 McMullan, D. Scanning electron microscopy 1928–1965. *Scanning* **17**, 175-185 (1995).
- 5 Brunauer, S., Emmett, P. H. & Teller, E. Adsorption of gases in multimolecular layers. *J. Am. Chem. Soc.* **60**, 309-319 (1938).
- 6 Walton, K. S. & Snurr, R. Q. Applicability of the BET method for determining surface areas of microporous metal–organic frameworks. *J. Am. Chem. Soc.* **129**, 8552-8556 (2007).
- 7 Düren, T., Millange, F., Férey, G., Walton, K. S. & Snurr, R. Q. Calculating geometric surface areas as a characterization tool for metal-organic frameworks. *J. Phys. Chem. C* **111**, 15350-15356 (2007).

## CHAPTER 3

# SYNTHESIS OF ISOSTRUCTURAL MOFs OF HKUST-1 VIA FUNCTIONALIZATION OF ORGANIC LIGANDS

### 3.1 Introduction

MOF materials are nanoporous crystals that have attracted intense interest for fundamental and applied purposes.<sup>1-4</sup> MOFs are interesting in part because of the concept of reticular synthesis, which allows families of isostructural crystals to be developed by varying ligand length and functionality.<sup>5,6</sup> Demonstrations of isostructural families are available for IRMOFs,<sup>7</sup> UiO-66,<sup>8-10</sup> and MIL-53,<sup>11,12</sup> among others. The first example of isostructural MOFs was the IRMOF series, in which the MOF-5 ligand (benzene-dicarboxylic acid, BDC) was functionalized with the organic groups -Br, -NH<sub>2</sub>, -OC<sub>3</sub>H<sub>7</sub>, -OC<sub>5</sub>H<sub>11</sub> and -C<sub>2</sub>H<sub>4</sub>, and its pore size was expanded with long molecular struts biphenyl, tetrahydropyrene, pyrene, and terphenyl without changing the underlying topology. Another recent example is the UiO-66 family of microporous materials based on a 3-D structure of zirconium-oxo clusters. Compared to most MOF materials, UiO-66 possesses an unprecedented thermal stability with high surface area. The successful incorporation of active functional groups, such as amino, nitro, bromo functional groups, into UiO-66 without losing its exceptionally high thermal and chemical stability demonstrate the possibility to modify the functionality of the adsorbent surface via the functionalization of organic ligands.<sup>10</sup>

HKUST-1 (also known as CuBTC), first reported by Chui et al.,<sup>13</sup> is one of these most widely studied MOFs. HKUST-1 is comprised of Cu<sup>2+</sup> paddlewheel clusters coordinated to 1,3,5-benzenetricarboxylate (H<sub>3</sub>BTC) organic linkers in a twisted boracite

(**tbo**) topology, forming an exceptionally rigid and highly porous network, shown in Figure 3.1. H<sub>3</sub>BTC is a multidentate linker that allows for the formation of rigid frameworks through aggregation of metal ions into M-O-C clusters. After synthesis, the remaining coordination sites (one per Cu atom) are occupied by water molecules, which can be removed by heating under vacuum. The removal of coordinated water reveals the open-metal sites, which are known to enhance the ability of the materials to adsorb particular molecules.<sup>14</sup> Many other copper based MOFs containing m-benzenedicarboxylate moieties possess open metal sites that have a strong affinity with specific gas molecules.<sup>15-17</sup> Adsorption properties of HKUST-1 for a variety of sorbate molecules including N<sub>2</sub>, O<sub>2</sub>, CO, CO<sub>2</sub>, N<sub>2</sub>O, CH<sub>4</sub>, C<sub>2</sub>H<sub>6</sub>, C<sub>2</sub>H<sub>4</sub>, n-dodecane, and water have been studied since the first report over a decade ago.<sup>14,18,19</sup> Compared with other MOFs that do not possess open-metal sites, HKUST-1 has exhibited high adsorption selectivity for CO<sub>2</sub> over CO and N<sub>2</sub> at low pressure.<sup>14</sup> However, the open-metal sites also have a strong affinity for water, which will decrease the capacity for other gases when present in a mixture.<sup>20</sup> Although HKUST-1 has been well studied, limited work has been done to modify the H<sub>3</sub>BTC ligand or functionalize HKUST-1 to optimize its properties for more specific applications. Few works have focused on the post-synthetic modification of HKUST-1 to introduce accessible secondary amine functionalities that react with nitric oxide (NO). However, the open metal coordination sites of the derivation are occupied by the functionalities.<sup>21</sup> Recently, Peikert et al. reported an amino-functionalized HKUST-1 material that is isostructural to the parent material.<sup>22</sup> In this project, in order to form isostructural MOFs of HKUST-1, I synthesized three polar

functionalized BTC ligands with acetamide, bromo, and nitro groups (Figure 3.2), in order to form the isostructural MOFs of HKUST-1 under **tbo** topology.

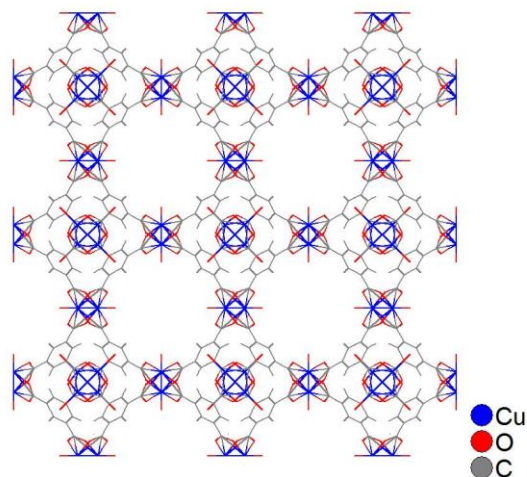


**Figure 3.1** The crystal structure of HKUST-1 along the [100] direction

### 3.2 Synthesis Results and Sample Activation

All chemicals were obtained commercially (Fisher and Sigma Aldrich) and used without further purification. There are three functionalized BTC ligands synthesized: acetamide-BTC, bromo-BTC, and nitro-BTC (Figure 3.2). By using these functionalized BTC ligands, three isostructural MOFs with HKUST-1 (tbo-acetamide, tbo-bromo, and tbo-nitro) were successfully synthesized, shown in Figure 3.3. The following are the synthesis details for the ligands and MOFs. The organic ligands and MOFs are stored in sealed vials prior to use.



**Figure 3.2** Functionalized ligands used for crystallizing functionalized HKUST-1 materials

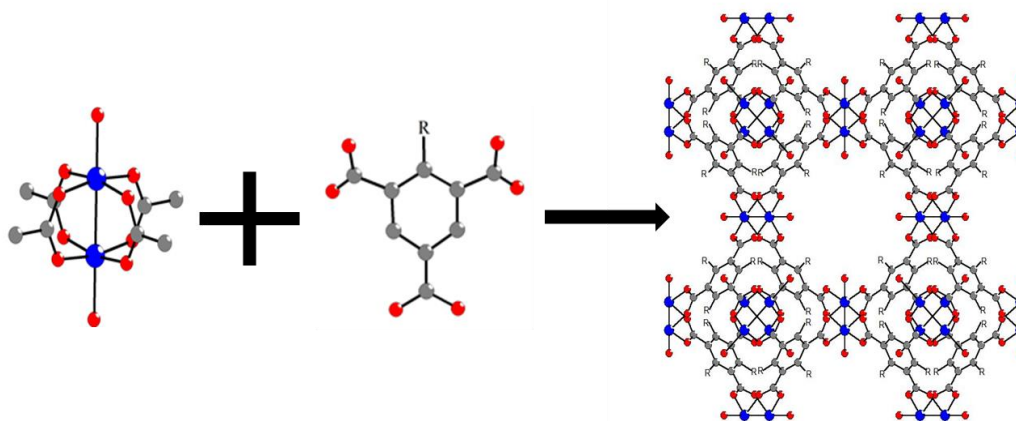


**Figure 3.3** Visualization of the components and crystal structure of series functionalized HKUST-1 materials under **tbo** topology (R=acetamide, bromo, or nitro)

### 3.2.1 Ligands Synthesis

**Preparation of acetamide-1,3,5-benzenetricarboxylic acid (acetamide-BTC, Figure 3.4):** A solution of 2,4,6-trimethyl-phenylamine (20 g) in  $\text{CH}_2\text{Cl}_2$  (200 mL) was cooled to  $0\text{ }^\circ\text{C}$  (ice-water bath). Acetyl chloride (AcCl, 11.92g) was added in to this solution during 5 minutes via an addition funnel followed with portion-wise addition of triethylamine ( $\text{Et}_3\text{N}$ , 15.4 g). The ice-bath was removed and the solution was allowed to warm to RT and stirred for 2 h. The resultant ivory colored solid was collected by

filtration and dried in vacuo. To remove the residual  $\text{Et}_3\text{NHCl}$ , the solid was suspended in water  $\text{H}_2\text{O}$  (240 mL) stirred for 0.5 h, and collected by filtration and dried to a constant weight, which results in 15 g of compound **1**. Sodium hydroxide ( $\text{NaOH}$ , 0.55 g) was added to a mixture of compound **1** (5 g) and water (165 mL) in a 500 mL flask equipped with magnetic stirrer and oil bath. Potassium permanganate ( $\text{KMnO}_4$ , 34 g) was added in several batches to the solution over 2 h with stirring at RT, and the final solution was heated to  $85\text{ }^\circ\text{C}$  with stirring for 3 days. The resultant brown slurry was then filtered to remove the large amount of  $\text{MnO}_2$ , and the filtrate was acidified with concentrated  $\text{HCl}$ . The aqueous solution is continuously extracted with ethyl ether. Removal of the solvent (ethyl ether) in vacuo affords product acetamide-BTC.  $^1\text{H NMR}$  (300 MHz,  $\text{D}_2\text{O}$ ): 8.47 (s, 2H), 2.21 (s, 3H).

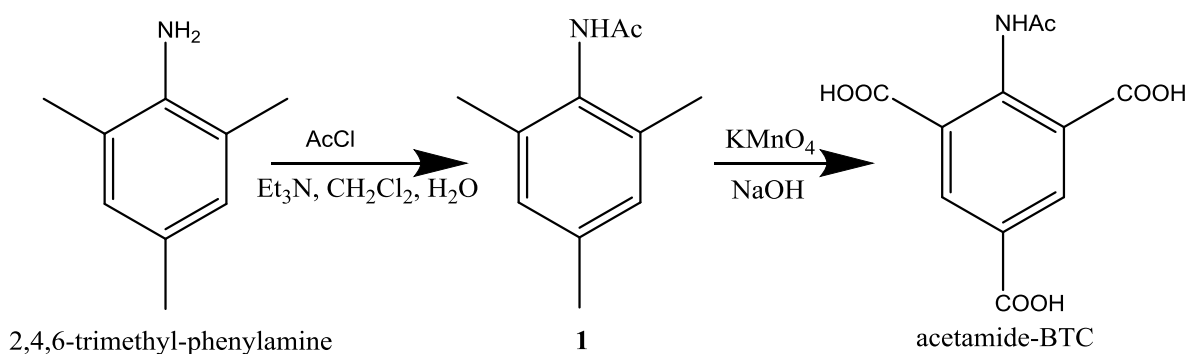


**Figure 3.4** Synthesis of acetamide-BTC

**Preparation of bromo-1,3,5-benzenetricarboxylic acid (bromo-BTC, Figure 3.5):** 2-bromomesitylene (20 g) was added in an aqueous (250 mL) solution of  $\text{NaOH}$  (5 g). Potassium permanganate ( $\text{KMnO}_4$ , 85 g) was added in several batches to the solution over 2 h with stirring at RT. The solution was heated to  $95\text{ }^\circ\text{C}$  with stirring for 3 days. The resultant brown slurry was then filtered to remove the large amount of  $\text{MnO}_2$ , and the

filtrate was acidified with concentrated HCl. The aqueous solution is continuously extracted with ethyl ether. Removal of the solvent (ethyl ether) in vacuo affords product bromo-BTC (7.8 g).  $^1\text{H NMR}$  (300 MHz, DMSO): 8.14 (s, 2H).

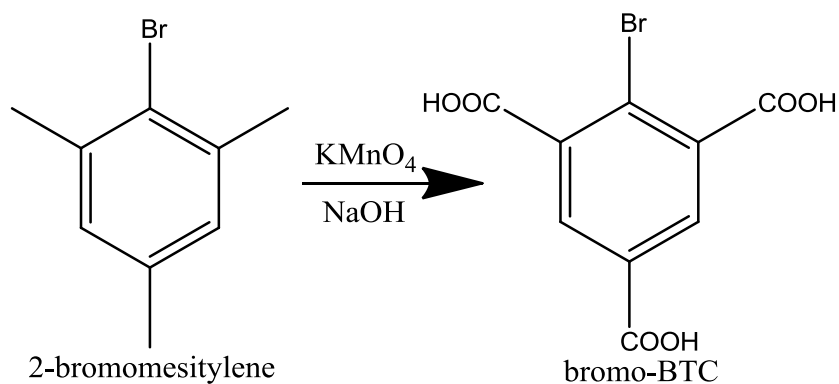


**Figure 3.5** Synthesis of bromo-BTC

**Preparation of nitro-1,3,5-benzenetricarboxylic acid (nitro-BTC, Figure 3.6):**

2-nitromesitylene (20 g) was added in an aqueous (250 mL) solution of NaOH (5 g). Potassium permanganate ( $\text{KMnO}_4$ , 85 g) was added in several batches to the solution over 2 h with stirring at RT. The solution was heated to 90 °C with stirring for 3 days. The resultant brown slurry was then filtered to remove the large amount of  $\text{MnO}_2$ , and the filtrate was acidified with concentrated HCl. The aqueous solution is continuously extracted with ethyl ether. Removal of the solvent (ethyl ether) in vacuo affords product nitro-BTC (5 g).  $^1\text{H NMR}$  (300 MHz, DMSO): 8.27 (s, 2H).



**Synthesis of tbo-acetamide:** A mixture of  $\text{Cu}(\text{NO}_3)_2 \cdot 3\text{H}_2\text{O}$  (72.48 mg), acetamide-BTC (53.4 mg), and DMF with 1M HCl aqueous solution (0.15 mL) was placed in a 20 mL glass vial, and the resulting mixture was heated in a conventional oven at 100 °C for 72 h and cooled to RT. The green product was obtained by filtration and washed with DMF. The yield was 57 mg.

**Synthesis of tbo-bromo:** A mixture of  $\text{Cu}(\text{NO}_3)_2 \cdot 3\text{H}_2\text{O}$  (72.48 mg), bromo-BTC (58 mg), and DMF with 15 equivalents formic acid (with respect to  $\text{Cu}(\text{NO}_3)_2 \cdot 3\text{H}_2\text{O}$ ) was placed in a 20 mL glass vial, and the resulting mixture was heated in a conventional oven at 90 °C for 48 h and cooled to RT. The green crystal was obtained by filtration and washed with DMF. The yield was 52 mg.

**Synthesis of tbo-nitro.:** A mixture of  $\text{Cu}(\text{NO}_3)_2 \cdot 3\text{H}_2\text{O}$  (72.48 mg), nitro-BTC (51 mg), and DMF with 1M HCl aqueous solution (0.15 mL) was placed in a 20 mL glass vial, and the resulting mixture was heated in a conventional oven at 120 °C for 60 h and cooled to RT. The green crystal was obtained by filtration and washed with DMF. The yield was 55 mg.

**Table 3.1** Summary of Synthesis Solvents, Decomposition Temperatures and Activation

Procedures of All Materials

MOFs	Synthesis Solvents	Decomposition temperatures ( °C)	Activation procedure (under vacuum)
tbo-bromo	DMF/Formic acid	300	2d methanol exchange, 170 °C, 8h
tbo-nitro	DMF/HCl sol.	280	3d ethanol exchange, 170 °C, 8h
tbo-acetamide	DMF/HCl sol.	280	2d methanol exchange, 170 °C, 8h

### 3.2.3 Activation Procedure for MOFs

The activation procedures used for MOFs are described below. The activation process has a significant impact on the adsorption capacity and surface areas are often the most difficult aspect of new MOF development. The activation procedures for all materials are summarized in the Table 3.1 as well.

**Activation of HKUST-1:** Materials were air-dried and then heated at 170 °C under vacuum for 8h.

**Activation of tbo-bromo and tbo-acetamide:** To remove the solvated DMF, the material was soaked in 20 mL of methanol for 2 days, with the solvent decanted and refreshed daily. The material was air-dried and was then heated at 170 °C under vacuum for 8h.

**Activation of tbo-nitro:** To remove the solvated DMF, the material was soaked in 20 mL of ethanol for 3 days, with the solvent decanted and refreshed daily. The material was air-dried and finally heated at 170 °C under vacuum for 8h.

### 3.3 Thermal Gravimetric Analysis for MOFs

Figure 3.7 shows a comparison among the TGA analysis performed on the tagged HKUST-1 materials. The decomposition temperatures for all materials are summarized in Table 3.1. In the TGA curve of tbo-bromo, a solvent loss step (30%) from RT up to 300 °C is observed. Thermogravimetric traces of tbo-acetamide and tbo-nitro show a weight loss of 28 % and 40%, respectively, in the temperature range 30-280 °C. Compared with HKUST-1, there is no obvious plateau of compositional stability observed for all tagged HKUST-1 materials. This result indicates that the solvent is removed as the temperature increases up to decomposition temperature, which may be

attributed the strong interaction between solvated DMF molecules and the polar functional groups. The tagged **tbo** series of MOFs have the similar decomposition temperature with the parent HKUST-1 material.<sup>13</sup>

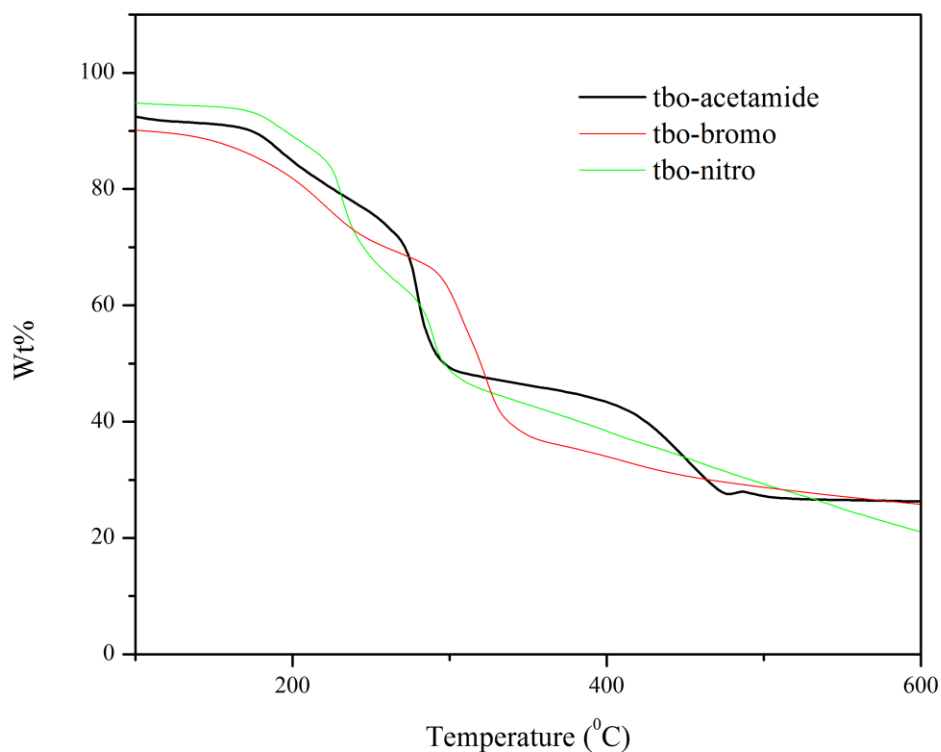


**Figure 3.7** TGA curves of as-synthesized tbo-bromo, tbo-nitro, and tbo-acetamide in nitrogen flux

### 3.4 Structure Characterization of tbo Series MOFs

Despite numerous synthesis attempts by varying synthesis temperature, time, pH value, stoichiometry, and solvents, we were unable to obtain single crystals of functionalized **tbo** series MOFs suitable for single-crystal XRD measurements. Thus, pXRD patterns are used to confirm the structures of these tagged materials. As shown in

Figure 3.8, the pXRD patterns of tbo-bromo, tbo-nitro, and tbo-acetamide are consistent with the HKUST-1 patterns.<sup>13</sup> This result indicates that the acetamide, bromo, and nitro functionalized products are isostructural with parent HKUST-1 under **tbo** topology. The crystallinity of the activated samples also has been examined via pXRD, in Figure 3.9- Figure 3.11. These pXRD patterns show the consistency between the activated samples and as-synthesized samples, which indicate that the **tbo** series of MOFs, including HKUST-1,<sup>20</sup> have a relatively high thermal stability and retain their crystallinity after the activation.

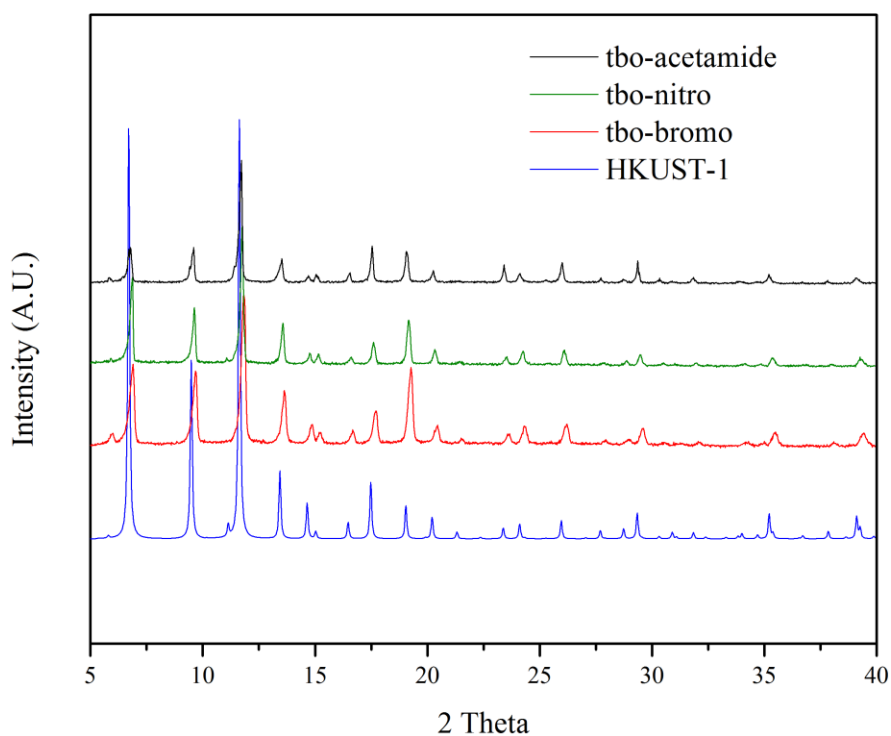


**Figure 3.8** pXRD diffractograms of nitro, acetamide, bromo functionalized MOF in the **tbo** topology and comparison with parent HKUST-1<sup>13</sup>

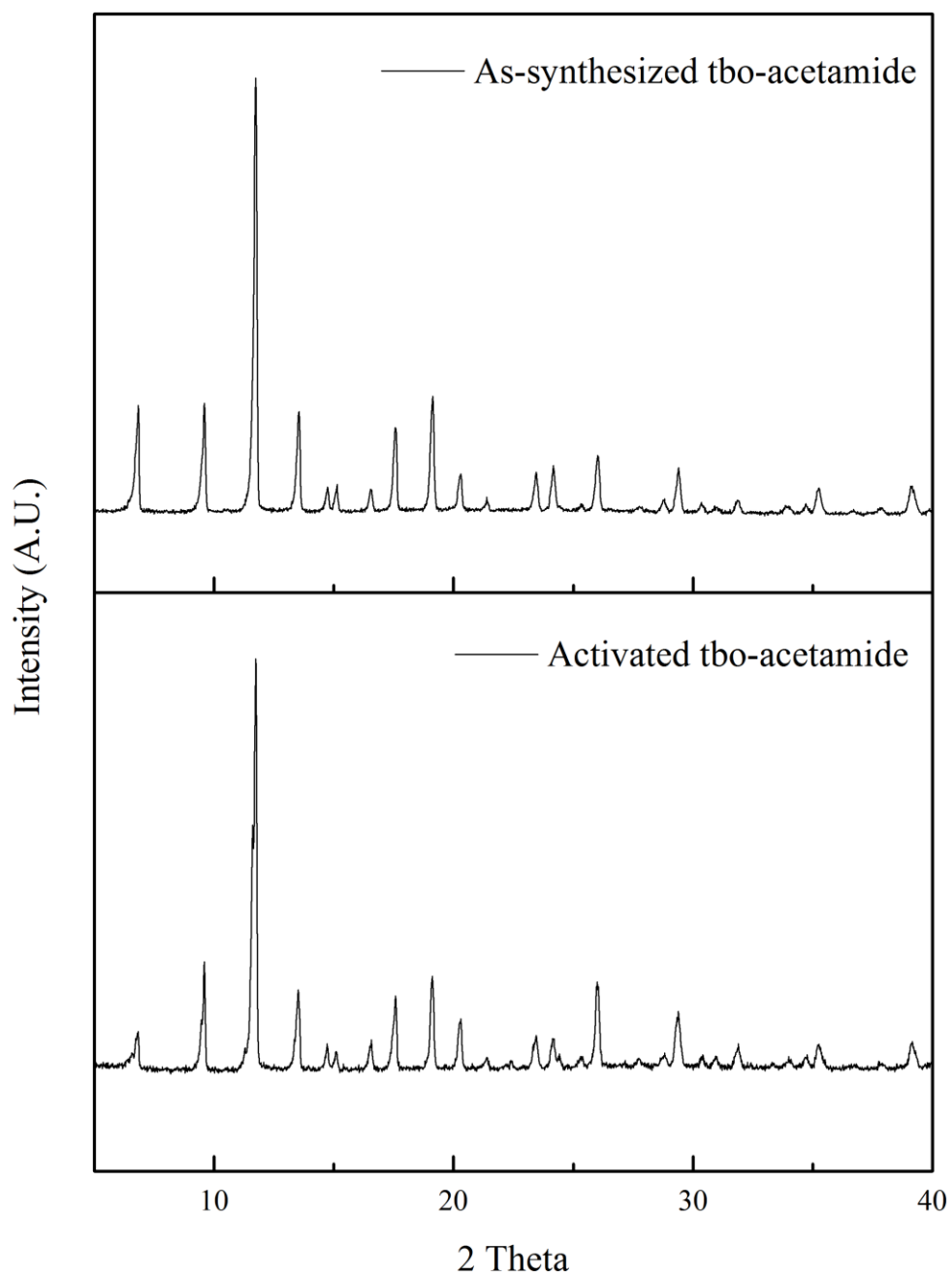


**Figure 3.9** pXRD diffractograms of as-synthesized (top) and activated (bottom) tbo-acetamide

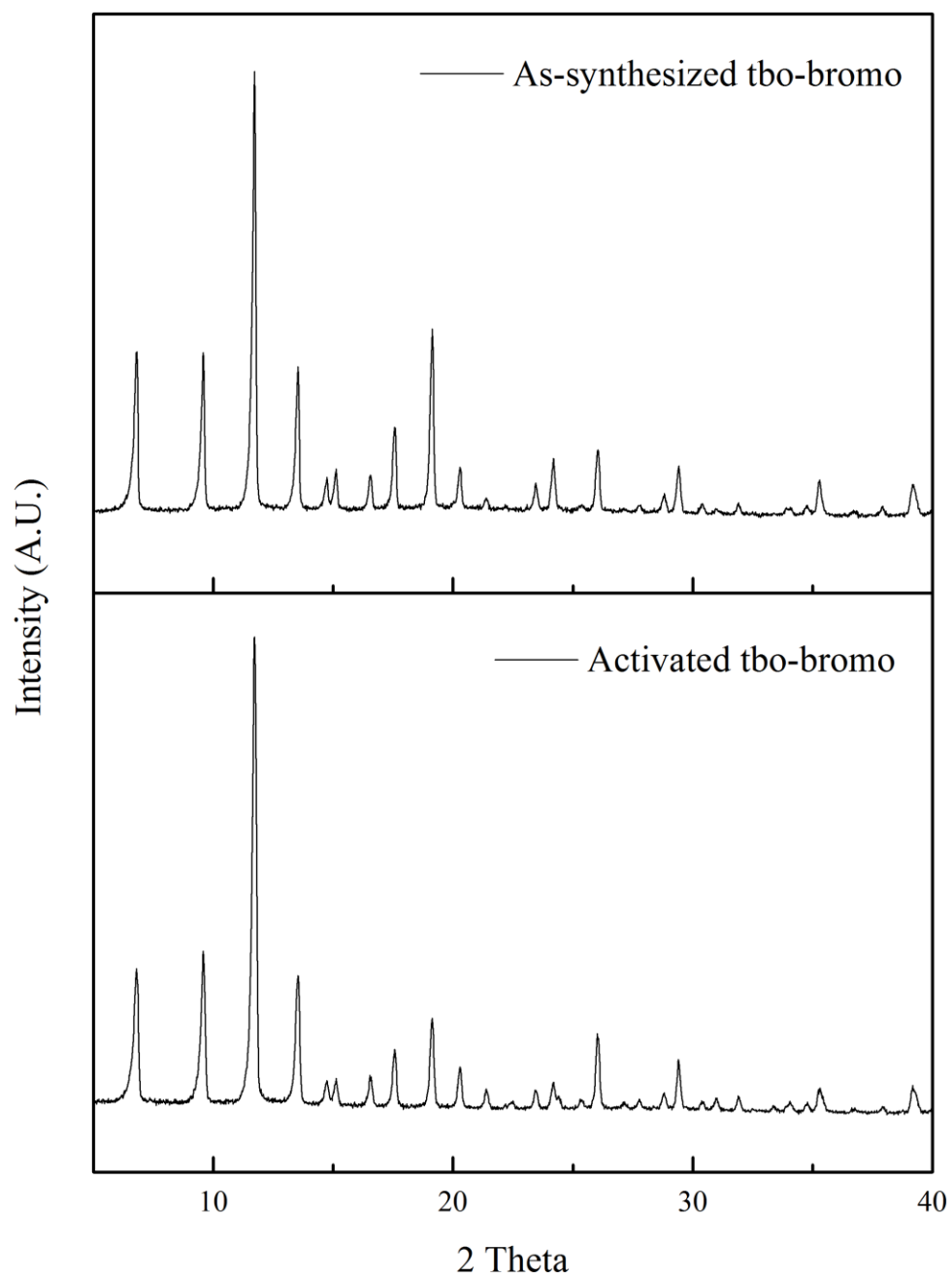


**Figure 3.10** pXRD diffractograms of as-synthesized (top) and activated (bottom) tbo-bromo

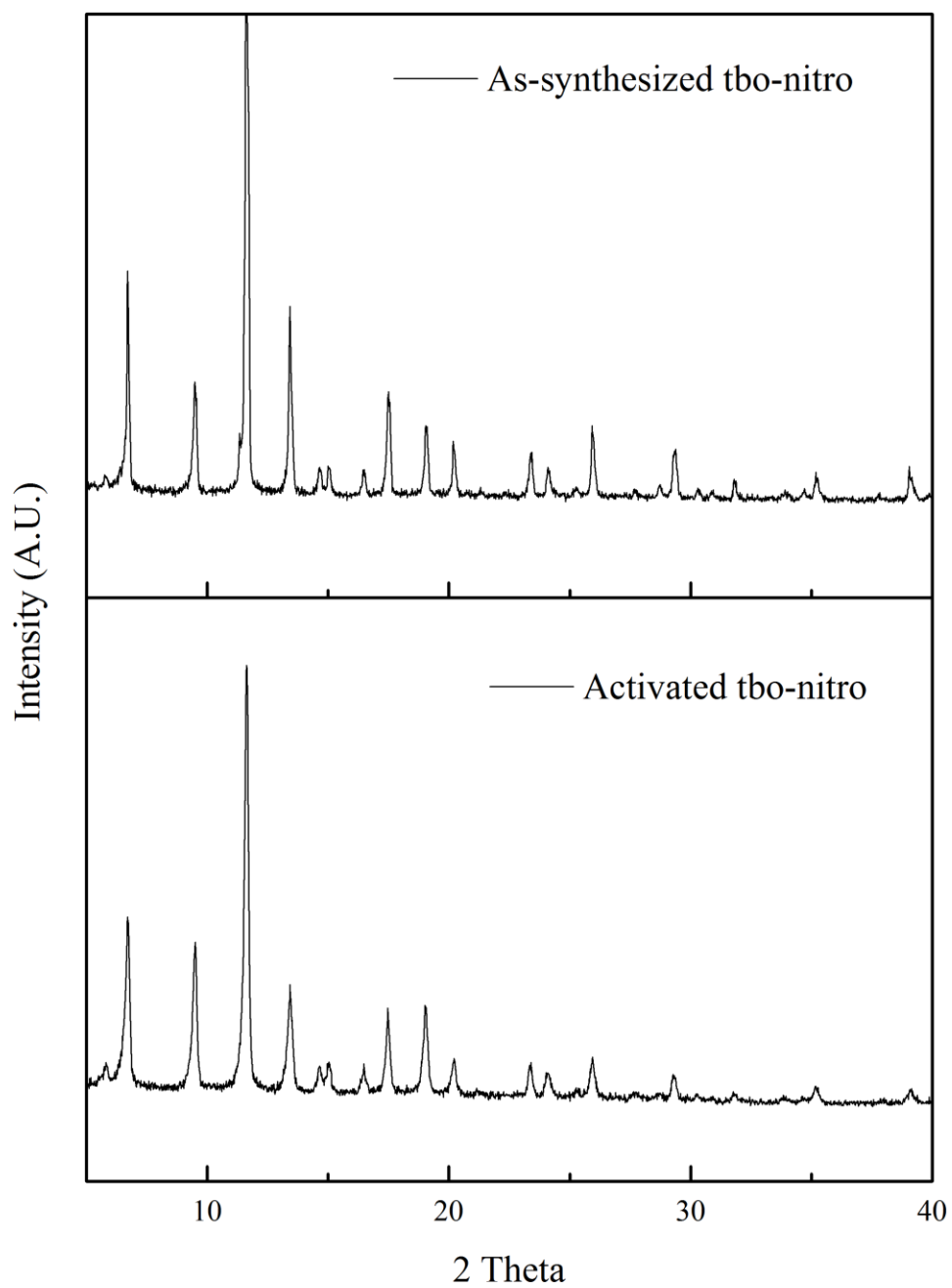


**Figure 3.11** pXRD diffractograms of as-synthesized (top) and activated (bottom) tbo-nitro

### 3.5 Characterization of the Functionality of MOFs

The presence of the functional groups (nitro, bromo, and acetamide) on the linkers was further investigated by means of FTIR spectroscopy. Before acquiring the spectra, the samples were activated under vacuum to remove the residual solvent and then prepared as a KBr pellet. From Figure 3.12, the typical absorption modes of the nitro, bromo, and acetamide groups are clearly visible in the functionalized MOFs, which confirm the effective functionalization of the internal pore surface. The IR spectra of the unfunctionalized parent HKUST-1 is also shown for comparison.

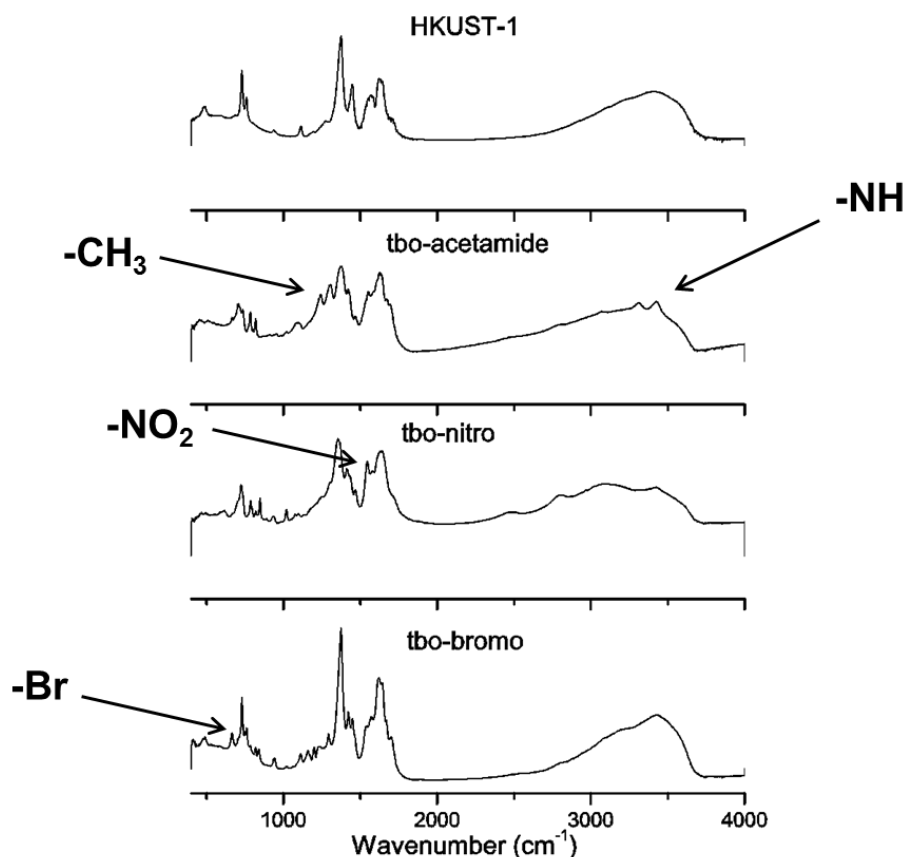


**Figure 3.12** FTIR spectra of tbo-X (X=H, nitro, bromo, acetamide) activated at 120<sup>0</sup>C in vacuum

### 3.6 Surface Area Analysis of MOFs

The accessible surface area is calculated theoretically by rolling the probe particle (such as nitrogen molecule) along the surface of MOFs.<sup>23</sup> All values reported in this dissertation for nitrogen were calculated with a probe diameter of 3.681 Å. The accessible surface areas are the values that could be obtained for a perfect MOF sample. If the experimental values are much lower than the calculated values, it can be assumed that the MOF was not properly activated or that the MOF sample has low crystallinity. Nitrogen adsorption isotherms for tbo-acetamide, tbo-bromo, and tbo-nitro at 77 K shown in Figures 3.13-Figure 3.15 were used to obtain the BET surface areas of activated MOFs. The measured surface areas and the accessible surface areas are summarized in Table 3.2. The BET surface areas of all the materials are close to the calculated accessible surface areas, except for tbo-nitro materials. This result means that tbo-acetamide and tbo-bromo were obtained in relatively pure phases and were properly activated. There are two reasons for low BET surface area of tbo-nitro: the existence of impure phases due to incorrect synthesis conditions or the improper activation procedure. More effort needs to be made for getting purer phase or proper activation procedure to obtain the maximum BET surface area of tbo-nitro material. The key observations from these experiments are summarized in Table 3.2, which also lists the experimental crystal structure of each material and their BET surface areas. In addition to the ligands presented in Figure 3.2, Table 3.2 also includes the amino functionalized material reported by Peikert et al.<sup>22</sup>

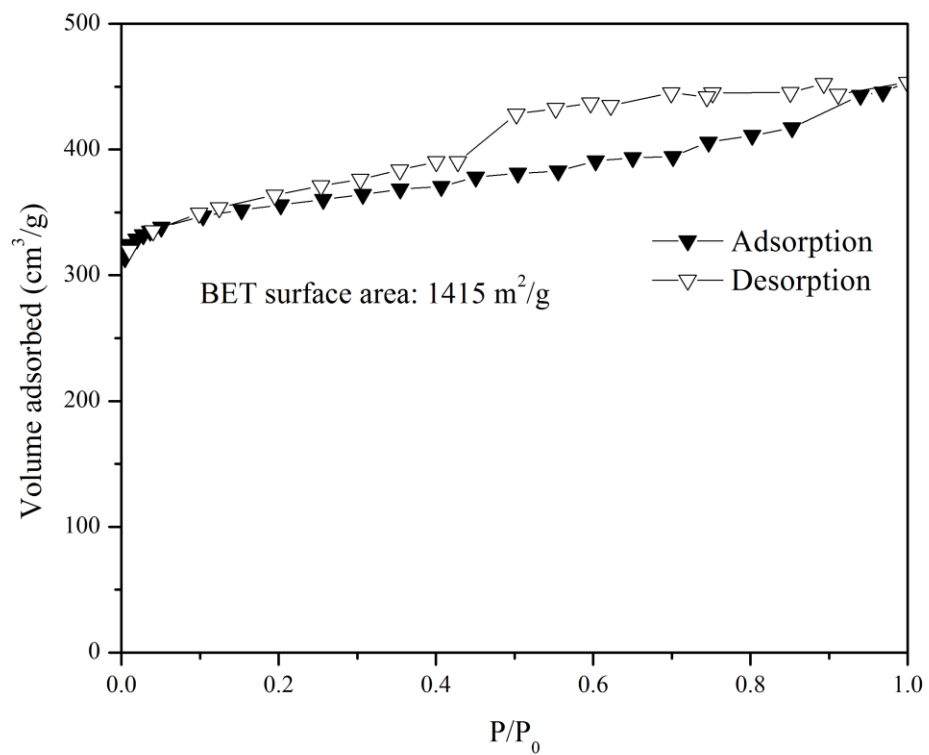


**Figure 3.13** Nitrogen isotherm of activated tbo-acetamide at 77K (closed symbols – adsorption, open symbols – desorption)

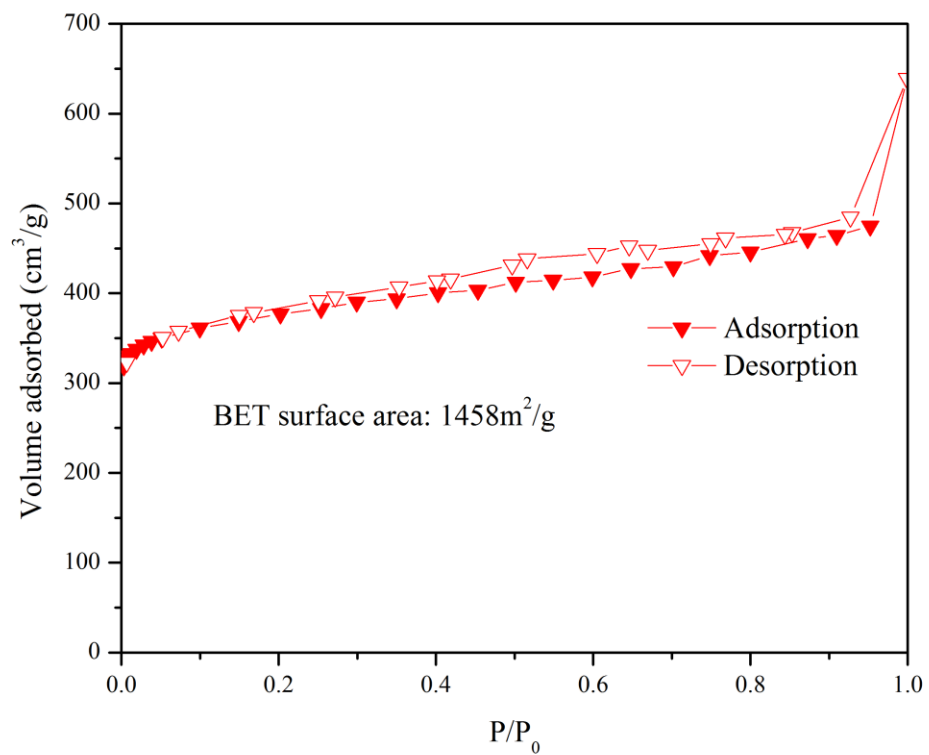


**Figure 3.14** Nitrogen isotherm of activated tbo-bromo at 77K (closed symbols – adsorption, open symbols – desorption)

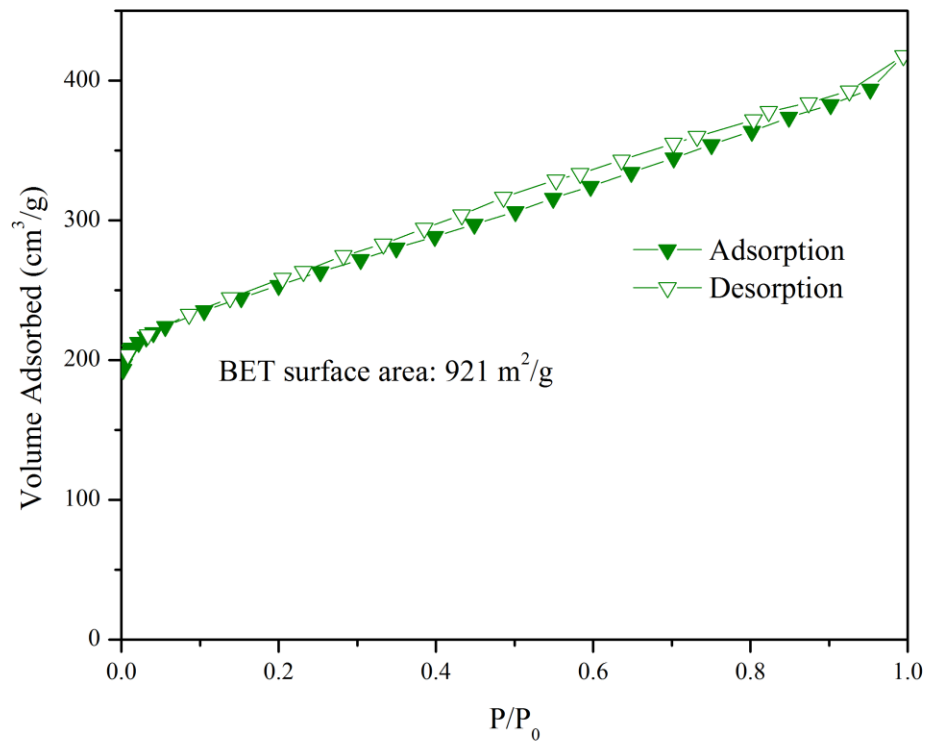


**Figure 3.15** Nitrogen isotherm of activated tbo-nitro at 77K (closed symbols – adsorption, open symbols – desorption)

**Table 3.2** Observed Structure Topology, Synthesis Solvents, Accessible Surface Areas, and N<sub>2</sub> BET Surface Areas of HKUST-1 and Four Tagged HKUST-1 Materials Made with Functionalized Ligands

Linker	Solvent	Topology	Surface Area (m <sup>2</sup> /g)	
			Accessible <sup>23</sup>	BET
<b>H-BTC</b> <sup>13*</sup>	H <sub>2</sub> O/EtOH	<b>tbo</b>	2224	1800, <sup>24</sup> 1509
<b>bromo</b>	DMF/ Formic acid	<b>tbo</b>	1929	1458
<b>nitro</b>	DMF/HCl sol.	<b>tbo</b>	1998	921
<b>acetamide</b>	DMF/HCl sol.	<b>tbo</b>	1680	1415
<b>amino</b> <sup>22</sup> *	DMA	<b>tbo</b>	2015	1834 <sup>22</sup>

\* Single crystal XRD structure has been solved

### 3.7 Conclusions

In this chapter, I have successfully constructed three functionalized HKUST-1 with acetamide, bromo, and nitro polar functional groups under **tbo** topology via solvothermal synthesis. So far, four of the functionalized materials (bromo, nitro, acetamide, and amino) retain the same **tbo** topology as the parent HKUST-1 structure. However, the synthesis procedure adopted for each new, tagged MOF is slightly different with each other and also differs with respect to the one for HKUST-1.<sup>14</sup> Even for isostructural MOFs, the synthesis conditions are not same with each other, which indicate that the functional groups have a significant effect on the synthesis environment. This result also has been found in other series of isostructural MOFs.<sup>8,25,26</sup> These tagged HKUST-1 materials show the similar decomposition temperature with the HKUST-1 material. In TGA curves on these tagged materials, the missing of the plateau of composition stability indicates the strong interaction between solvated DMF molecules and functional groups, which is not observed in HKUST-1. The pXRD patterns of

activated samples indicate that the tagged MOFs have the same thermal stability with HKUST-1 and retain their crystallinity after the activation. This chapter shows that the successful incorporation of active functional groups, such as acetamide, bromo, nitro functional groups, into HKUST-1 without losing its thermal stability demonstrate the possibility to modify the functionality of HKUST-1 via the functionalization of organic ligands.

### 3.8 References

- 1 Ferey, G. Hybrid porous solids: past, present, future. *Chem. Soc. Rev.* **37**, 191-214 (2008).
- 2 James, S. L. Metal-organic frameworks. *Chem. Soc. Rev.* **32**, 276-288 (2003).
- 3 Kitagawa, S., Kitaura, R. & Noro, S. Functional porous coordination polymers. *Angew. Chem. Int. Ed.* **43**, 2334-2375 (2004).
- 4 Czaja, A. U., Trukhan, N. & Muller, U. Industrial applications of metal-organic frameworks. *Chem. Soc. Rev.* **38**, 1284-1293 (2009).
- 5 O'Keeffe, M. Design of MOFs and intellectual content in reticular chemistry: a personal view. *Chem. Soc. Rev.* **38**, 1215-1217 (2009).
- 6 Yaghi, O. M. *et al.* Reticular synthesis and the design of new materials. *Nature* **423**, 705-714 (2003).
- 7 Eddaoudi, M. *et al.* Systematic design of pore size and functionality in isorecticular MOFs and their application in methane storage. *Science* **295**, 469-472 (2002).
- 8 Cmarik, G. E., Kim, M., Cohen, S. M. & Walton, K. S. Tuning the adsorption properties of UiO-66 via ligand functionalization. *Langmuir* **28**, 15606-15613 (2012).
- 9 Huang, Y., Qin, W., Li, Z. & Li, Y. Enhanced stability and CO<sub>2</sub> affinity of a UiO-66 type metal-organic framework decorated with dimethyl groups. *Dalton Trans.* **41**, 9283-9285 (2012).
- 10 Kandiah, M. *et al.* Synthesis and stability of tagged UiO-66 Zr-MOFs. *Chem. Mater.* **22**, 6632-6640 (2010).
- 11 Biswas, S., Ahnfeldt, T. & Stock, N. New functionalized flexible Al-MIL-53-X (X = -Cl, -Br, -CH<sub>3</sub>, -NO<sub>2</sub>, -(OH)<sub>2</sub>) solids: syntheses, characterization, sorption, and breathing behavior. *Inorg. Chem.* **50**, 9518-9526 (2011).
- 12 Serra-Crespo, P. *et al.* Interplay of metal node and amine functionality in NH<sub>2</sub>-MIL-53: modulating breathing behavior through intra-framework interactions. *Langmuir* **28**, 12916-12922 (2012).
- 13 Chui, S. S. A chemically functionalizable nanoporous material [Cu<sub>3</sub>(TMA)<sub>2</sub>(H<sub>2</sub>O)<sub>3</sub>]<sub>n</sub>. *Science* **283**, 1148-1150 (1999).
- 14 Karra, J. R. & Walton, K. S. Effect of open metal sites on adsorption of polar and nonpolar molecules in metal-organic framework Cu-BTC. *Langmuir* **24**, 8620-8626 (2008).

- 15 Chen, B., Ockwig, N. W., Millward, A. R., Contreras, D. S. & Yaghi, O. M. High H<sub>2</sub> adsorption in a microporous metal-organic framework with open metal sites. *Angew. Chem. Int. Ed.* **44**, 4745-4749 (2005).
- 16 Guo, Z. *et al.* A metal-organic framework with optimized open metal sites and pore spaces for high methane storage at room temperature. *Angew. Chem. Int. Ed.* **50**, 3178-3181 (2011).
- 17 Hu, Y. *et al.* A new MOF-505 analog exhibiting high acetylene storage. *Chem. Commun.*, 7551-7553 (2009).
- 18 Wang, S., Yang, Q. & Zhong, C. Adsorption and separation of binary mixtures in a metal-organic framework Cu-BTC: A computational study. *Sep. Purif. Technol.* **60**, 30-35 (2008).
- 19 Liu, J. *et al.* CO<sub>2</sub>/H<sub>2</sub>O adsorption equilibrium and rates on metal-organic frameworks: HKUST-1 and Ni/DOBDC. *Langmuir* **26**, 14301-14307 (2010).
- 20 Schoenecker, P. M., Carson, C. G., Jasuja, H., Flemming, C. J. J. & Walton, K. S. Effect of water adsorption on retention of structure and surface area of metal-organic frameworks. *Ind. Eng. Chem. Res.* **51**, 6513-6519 (2012).
- 21 Ingleson, M. J., Heck, R., Gould, J. A. & Rosseinsky, M. J. Nitric oxide chemisorption in a postsynthetically modified metal-organic framework. *Inorg. Chem.* **48**, 9986-9988 (2009).
- 22 Peikert, K., Hoffmann, F. & Froba, M. Amino substituted Cu<sub>3</sub>(btc)<sub>2</sub>: a new metal-organic framework with a versatile functionality. *Chem. Commun.* **48**, 11196-11198 (2012).
- 23 Düren, T., Millange, F., Férey, G., Walton, K. S. & Snurr, R. Q. Calculating geometric surface areas as a characterization tool for metal-organic frameworks. *J. Phys. Chem. C* **111**, 15350-15356 (2007).
- 24 Vitillo, J. G. *et al.* Role of exposed metal sites in hydrogen storage in MOFs. *J. Am. Chem. Soc.* **130**, 8386-8396 (2008).
- 25 Uemura, K., Onishi, F., Yamasaki, Y. & Kita, H. Syntheses, crystal structures, and water adsorption behaviors of jungle-gym-type porous coordination polymers containing nitro moieties. *J. Solid State Chem.* **182**, 2852-2857 (2009).
- 26 Chen, Z. *et al.* Significantly enhanced CO<sub>2</sub>/CH<sub>4</sub> separation selectivity within a 3D prototype metal-organic framework functionalized with OH groups on pore surfaces at room temperature. *Eur. J. Inorg. Chem.* **2011**, 2227-2231 (2011).

## CHAPTER 4

# SYNTHESIS OF NEW ISOSTRUCTURAL CU-BTC MOFS WITH FUNCTIONALIZED ORGANIC LIGANDS

### 4.1 Introduction

The main functionalization method is to incorporate the functional groups into the organic linkers and then synthesize isostructural MOFs by using these functionalized ligands. This pre-functionalization method of MOF materials has been successfully applied to many MOF systems, including UMCM-1,<sup>1</sup> UiO-66,<sup>2-5</sup> MIL-53,<sup>6</sup> DMOF<sup>7</sup> and others. However, the functional groups may interfere with the formation of the desired MOF. The predictability associated with MOF crystal structures is complicated in situations where ligand functionalization leads to new crystal structures. In one example of this type, using the H<sub>3</sub>BTB-[MeO]<sub>3</sub> ligand and Zn(II) allows the formation of methoxy-functionalized analogue of MOF-177, while the combination of H<sub>3</sub>BTB-[OH]<sub>3</sub> and Zr(II) generate an interpenetrated framework with a different topology.<sup>8</sup> Different functionalized ligands are known to give different polymorphs in Zn and Cd ZIFs, and solvent assisted ligand exchange has been used to interconvert the Cd-based structures.<sup>9</sup>

Chapter 3 showed the successful synthesis of isostructural MOFs of HKUST-1 under **tbo** topology by using the acetamide, bromo, and nitro functionalized ligands. To further explore the crystal structures available with HKUST-1 derivatives, in addition to these three functionalized ligands presented in Chapter 3, I also synthesized another three functionalized ligands (Figure 4.1), methyl-BTC, ethyl-BTC, and methoxy-BTC. The original goal was to form functionalized isostructural MOFs of HKUST-1 with all functionalized BTC ligands, but instead of the formation of tagged HKUST-1 with

methyl, ethyl, and methoxy functional groups, I synthesized a completely new series of isostructural Cu-based frameworks by combining these ligands with the same Cu<sup>2+</sup> paddlewheel used in HKUST-1 (Figure 4.2). These three frameworks have a different crystal structure from HKUST-1. Topological analysis<sup>10</sup> shows that these frameworks have a **fmj** net (Figure 4.2) The **fmj** net has been constructed previously on purely topological grounds but no material had previously been observed to form this structure.

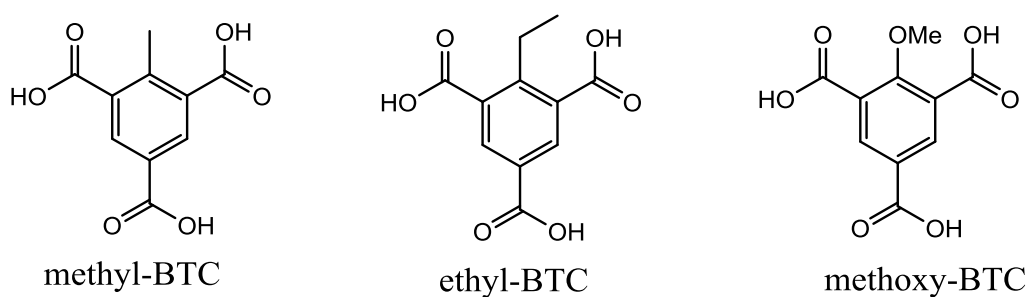


**Figure 4.1** Functionalized ligands used for crystallizing novel functionalized CuBTC

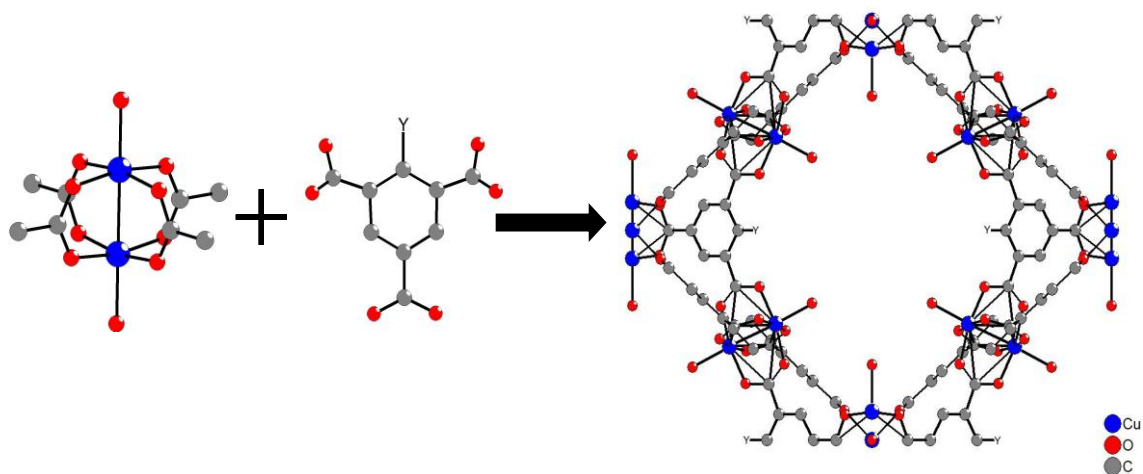


**Figure 4.2** Visualization of the components and crystal structure of new series CuBTC materials under the **fmj** topology

## 4.2 Synthesis Results and Sample Activation

All chemicals were obtained commercially (Fisher and Sigma Aldrich) and used without further purification. The following are the experimental details for synthesis procedures of another three functionalized BTC ligands: methyl-BTC, ethyl-BTC, and methoxy-BTC (Figure 4.1) and three new functionalized CuBTC materials, fmj-methyl, fmj-ethyl, and fmj-methoxy (Figure 4.2). As described in Chapter 3, the organic ligands and MOFs are stored in sealed vials prior to use. Samples are stored in sealed vials prior to use. Synthesis solvents of all materials were summarized in Table 4.1.

### 4.2.1 Ligand Synthesis

**Preparation of methyl-1,3,5-benzenetricarboxylic acid (methyl-BTC, Figure 4.3):** Coumalic acid (25.0 g, 0.179 mol) was added into a mixture of 450 mL trimethylorthoformate and 150 mL methanol with concentrated H<sub>2</sub>SO<sub>4</sub> (28.5 mL, 0.539 mol) at RT. The reaction mixture was heated at reflux temperature for 48 h after which it was cooled to 0<sup>o</sup>C and diluted with 500 mL ethyl acetate (EtOAc). The solution was then poured into saturated aqueous NaHCO<sub>3</sub>, mixed thoroughly, and the layers separated. The aqueous layer was extracted twice with 200 mL portions of EtOAc. The combined organic extract was washed with brine and dried over MgSO<sub>4</sub>. Removal of the solvent in vacuo afforded the crude products which were separated by column separator (9:1 CH<sub>2</sub>Cl<sub>2</sub>: EtOAc) to yield 20.5 g of **1**. <sup>1</sup>H NMR (300 MHz, CDCl<sub>3</sub>): 7.67 (s, 1H), 7.59 (d, 1H), 6.64 (d, 1H), 4.30 (s, 3H), 3.78 (s, 3H), 3.75 (s, 3H). **1** (20 g, 0.1 mol) and methyl acetoacetate (12 mL, 0.11 mol) were added in 500 mL of methanol with Na<sub>2</sub>CO<sub>3</sub> (powdered, 1.1 g, 0.01 mol) at RT. The reaction as stirred for 24h whereupon it was diluted with 1 L of water, extracted with CH<sub>2</sub>Cl<sub>2</sub>, and then brine was added to force

separation of its layers. The organic layer was dried with  $\text{Na}_2\text{SO}_4$ . Evaporation of the solvent in vacuo afforded the crude products which were separated by column filtration ( $\text{CH}_2\text{Cl}_2$ ) to yield 18.42 g of **2**.  $^1\text{H}$  NMR (300 MHz,  $\text{CDCl}_3$ ): 8.489 (s, 2H), 3.916 (s, 9H), 2.728 (s, 3H). A mixture of **2** with an aqueous solution (92.1 mL water) of 22 g of KOH dissolved in 92.1 mL tetrahydrofuran (THF) and 184.2 mL ethanol (1:2) was refluxed for 1 h. Acidification (concentrated HCl) produced the acid of **2**. Ethyl acetate was used to extract the product from solution. Then, water was used to extract salts from the crude product solution. Removal of the solvent (EtOAc) in vacuo afforded the crude product methyl-BTC.  $^1\text{H}$  NMR (300 MHz, Acetone): 8.59 (s, 2H), 2.81(s, 3H).

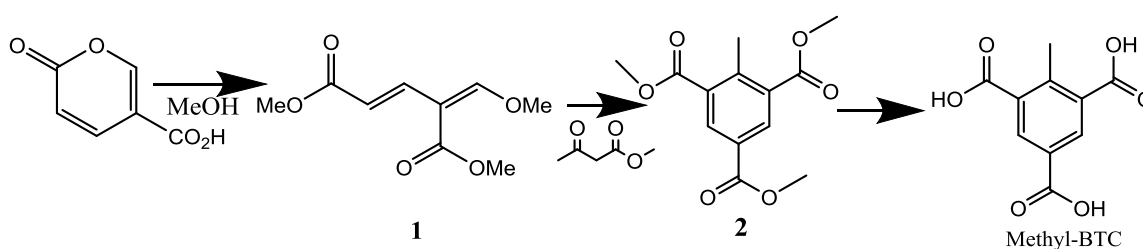


**Figure 4.3** Synthesis of methyl-BTC

**Preparation of ethyl-1,3,5-benzenetricarboxylic acid (ethyl-BTC, Figure 4.4):**

$\text{Na}_2\text{CO}_3$  (powdered, 1.1g, 0.01mol) was added to a solution of **1** (20g, 0.1mol) and methyl propionylacetate (12.76 mL, 0.11mol) in 500 mL of methanol at RT. The reaction was stirred for 24h whereupon it was diluted with 1 L of water, extracted with  $\text{CH}_2\text{Cl}_2$ , and then brine was added to force separation of its layers. The organic layer was dried with  $\text{Na}_2\text{SO}_4$ . Evaporation of the solvent in vacuo afforded the crude products which were separated by column filtration ( $\text{CH}_2\text{Cl}_2$ ) to yield 18.56 g of **3**.  $^1\text{H}$  NMR (300 MHz,  $\text{CD}_2\text{Cl}_2$ ): 8.471 (s, 2H), 3.96 (s, 9H), 3.20 (m, 2H), 1.232 (t, 3H). A mixture of **3** was refluxed for 1 h with an aqueous solution (92.1 mL water) of 22 g of potassium

hydroxide dissolved in 92.1 mL tetrahydrofuran (THF) and 184.2 mL ethanol (1:2). Acidification (concentrated HCl) produced the acid of **3**. Ethyl acetate was used to extract the product from solution. Then, water was used to extract salts from the crude product solution. Removal of the solvent (EtOAc) in vacuo afforded the crude product ethyl-BTC.  $^1\text{H NMR}$  (300 MHz, Acetone): 8.66 (s, 2H), 3.43 (m, 2H), 1.34 (t, 3H).

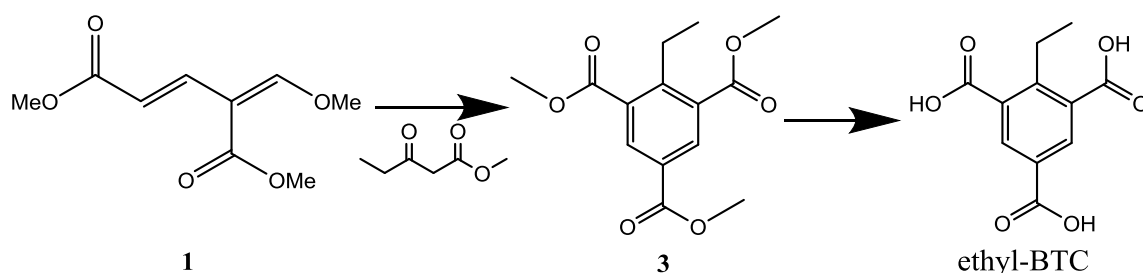


**Figure 4.4** Synthesis of ethyl-BTC

**Preparation of methoxy-1,3,5-benzenetricarboxylic acid (methoxy-BTC, Figure 4.5):** 2,6-bis(hydroxymethyl)-p-cresol (20 g) and  $\text{K}_2\text{CO}_3$  (32.73 g) were added slowly into a mixture of  $\text{CH}_3\text{I}$  (20.16 g) and DMF (200 mL) while stirring at RT for 3 days. Yellow milky solid was obtained, and then diluted with water and extracted with ethyl acetate (EtOAc). Removal of the solvent EtOAc in vacuo afford the crude product which was separated by column separator (1:1  $\text{CH}_2\text{Cl}_2$ : EtOAc) to yield 11.9 g of **4**. Sodium hydroxide (NaOH, 0.55 g) was added into a mixture of compound **4** (5 g) and water (165 mL) in a 500 mL flask equipped with magnetic stirrer and oil bath. Potassium permanganate ( $\text{KMnO}_4$ , 20.3 g) was added in several batches to the solution over 2h with stirring at RT, and then the solution was heated to 80 °C with stirring for 3 days. The resultant brown slurry was filtered to remove the large amount of  $\text{MnO}_2$ , and the filtrate was acidified with concentrated HCl. The aqueous solution is continuously extracted with

ethyl ether. Removal of the solvent (ethyl ether) in vacuo affords product methoxy-BTC (3.6 g).  $^1\text{H NMR}$  (300 MHz,  $\text{D}_2\text{O}$ ): 8.33 (s, 2H), 3.73 (s, 3H).

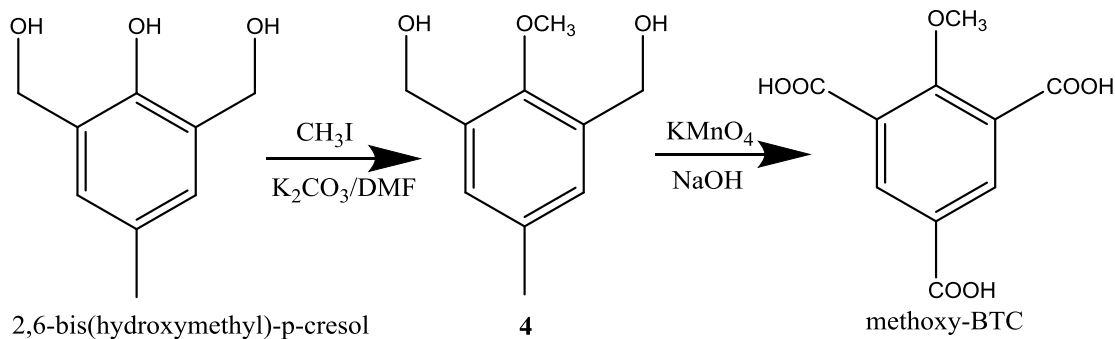


**Figure 4.5** Synthesis of methoxy-BTC

#### 4.2.2 MOF Synthesis Procedures

Like the **tbo** series of MOFs, the synthesis procedure adopted for each **fmj** MOF is different from each other, and also differs with respect to those of the **tbo** series MOFs.<sup>11,12</sup> This result shows that the impact of functional groups on the synthesis environments necessitates that significant effort be expended to identify synthetic conditions for the intended structure via the modification of synthesis parameters. Synthesis solvents of all **fmj** MOF materials are summarized in Table 4.1.

**Synthesis of HKUST-1:** HKUST-1 is synthesized as follows:  $\text{Cu}(\text{NO}_3)_2 \cdot 3\text{H}_2\text{O}$  (4.55 g, 18.8 mmol) is dissolved in 60 mL of de-ionized water, and trimesic acid (2.10 g, 9.99 mmol) is dissolved in 60 mL of ethanol via sonication. The solutions are added together and placed in 20 mL PTFE lined acid digestion vessels. The reaction is conducted at 100 °C for 18 h.

**Synthesis of fmj-methyl:** Blue crystals of  $[\text{Cu}_3(\text{MBTC})_2(\text{H}_2\text{O})_3]$  (fmj-methyl) are synthesized from the reaction of  $\text{H}_3\text{MBTC}$  ( $\text{H}_3\text{MBTC}$  is methyl-1,3,5-

benzenetricarboxylic acid, 44.8mg) with  $\text{Cu}(\text{NO}_3)_2 \cdot 3\text{H}_2\text{O}$  (72.48 mg) in DMF (5 mL) at  $120^\circ\text{C}$  for 66 h in the Teflon reactors.

**Synthesis of fmj-ethyl:** Blue crystals of  $[\text{Cu}_3(\text{EBTC})_2(\text{H}_2\text{O})_3]$  (fmj-ethyl) were synthesized from the reaction of  $\text{H}_3\text{EBTC}$  ( $\text{H}_3\text{EBTC}$  is Ethyl-1,3,5-benzenetricarboxylic acid, 46.7 mg) with  $\text{Cu}(\text{NO}_3)_2 \cdot 3\text{H}_2\text{O}$  (72.48 mg) in a mixture of ethanol (3 mL) and water (3 mL) at  $120^\circ\text{C}$  for 14 h in the Teflon reactors.

**Synthesis of fmj-methoxy: single crystal (a) and powder material (b):** The single crystal and powder form materials of fmj-methoxy are synthesized under different conditions.

- a. A mixture of  $\text{Cu}(\text{NO}_3)_2 \cdot 3\text{H}_2\text{O}$  (72.48 mg), methoxy-BTC (48 mg), and DMF (6 mL) with 1M HCl aqueous solution (0.25 mL) was placed in a 20 mL glass vial, and the resulting mixture was heated in a conventional oven at  $80^\circ\text{C}$  for 72 h and cooled to RT. The block shape green crystal was formed. (Single crystal)
- b. A mixture of  $\text{Cu}(\text{NO}_3)_2 \cdot 3\text{H}_2\text{O}$  (72.48 mg), methoxy-BTC (48 mg), and DMF (6 mL) with 1M HCl aqueous solution (0.05 mL) was placed in a 20 mL glass vial, and the resulting mixture was heated in a conventional oven at  $70^\circ\text{C}$  for 72 h and cooled to RT. The green powder material was obtained by filtration and washed with DMF. The yield was 65 mg. (Powder material)

**Table 4.1** Summary of Synthesis Solvents, Decomposition Temperatures and Activation Procedures of all materials

MOFs	Synthesis Solvents	Decomposition temperatures ( °C)	Activation procedure (under vacuum)
fmj-methyl	DMF	350	170 °C, 8h
fmj-ethyl	Water/ EtOH	350	170 °C, 8h
fmj-methoxy (b)	DMF/HCl sol.	300	170 °C, 8h

#### 4.2.3 Activation Procedure for MOFs

The activation procedures for all materials are summarized in the Table 4.1. the fmj-methyl, fmj-ethyl, and fmj-methoxy materials were air-dried and then heated at 170 °C under vacuum for 8h. The activation process has a significant impact on the adsorption capacity and surface areas and is often the most difficult aspect of new MOF development.<sup>13</sup>

#### 4.3 Thermal Gravimetric Analysis for MOFs

Figure 4.6 shows the decomposition curves of fmj series MOFs. For fmj-methyl and fmj-ethyl MOFs, most of solvents are lost before 150 °C, following with plateaus of compositional stability up to 350 °C. There is no plateau for MOF material with methoxy functional groups, which indicates a strong interaction between solvated DMF molecules and adsorbent surface. Considering the results in Chapter 3, the plateaus do not appear in TGA curves of the **tbo** series MOFs. The functional groups in **tbo** series of MOFs and the methoxy functional group in fmj-methoxy all are polar functional groups. The strong interaction between solvated DMF molecules and adsorbents may be attributed to the

polar functionality of MOFs. The fmj-methyl and fmj-ethyl materials have a slightly higher decomposition temperature than the fmj-methoxy. The decomposition temperatures for all **fmj** materials are summarized in Table 4.1. The decomposition temperatures of **tbo** series MOFs were found to be slightly lower than those of the methyl, ethyl, and methoxy functionalized MOFs. However, the decomposition temperature is not necessarily consistent with thermal stability of materials.

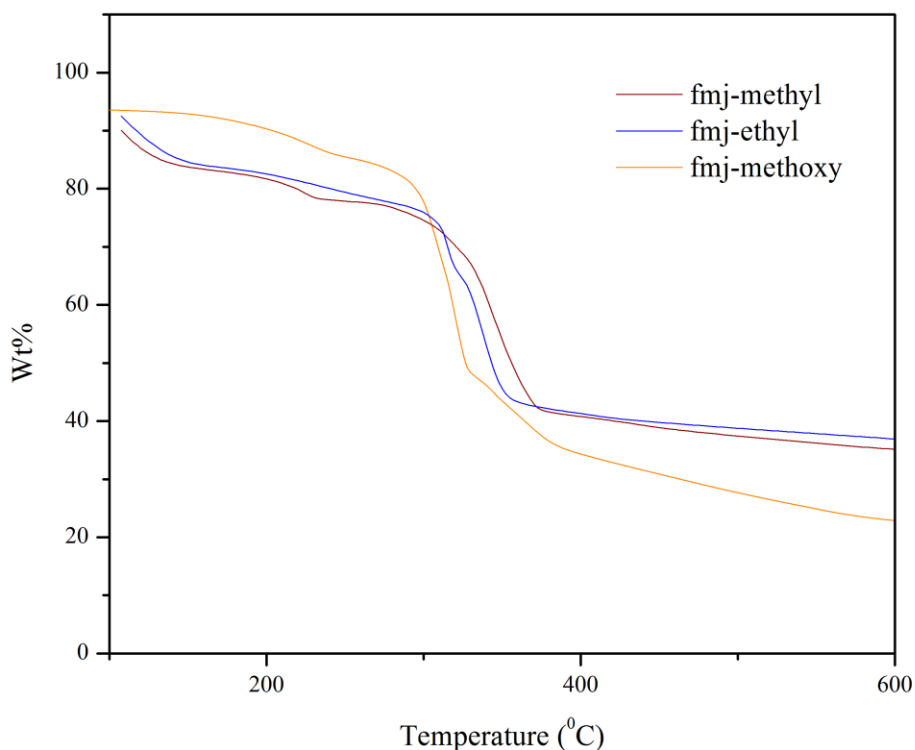


**Figure 4.6** TGA curves of as-synthesized fmj-methyl, fmj-ethyl, and fmj-methoxy in nitrogen flux

## 4.4 Structure Characterization of fmj Series MOFs

### 4.4.1 Description of Structure for fmj Series MOFs

Single-crystal XRD data of fmj series MOFs (fmj-methyl, fmj-ethyl, and fmj-methoxy) were collected on a single crystal Bruker APEX CCD diffraction system with CuK $\alpha$  radiation. The structures were solved by direct methods with the help of SHELX-97 and refined by full-matrix least-squared techniques using SHELXL-97.

**Table 4.2** Crystallographic Data for fmj-methoxy. <sup>a</sup>  $R = \sum ||F_0| - |F_c|| / \sum |F_0|$ , <sup>b</sup>  $wR = [\sum w(F_0 - F_c)^2 / \sum w(F_0^2)]^{1/2}$

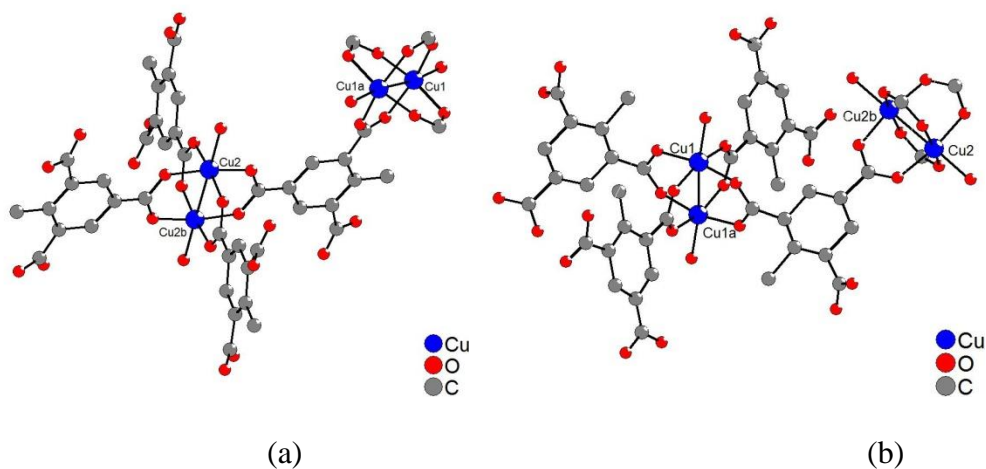
Compound	fmj-methyl	fmj-ethyl	fmj-methoxy
Formula	C <sub>21</sub> H <sub>16</sub> Cu <sub>3</sub> O <sub>15</sub>	C <sub>22</sub> H <sub>14</sub> Cu <sub>3</sub> O <sub>22.5</sub>	C <sub>20</sub> H <sub>14</sub> Cu <sub>3</sub> O <sub>15.75</sub>
MW(g mol <sup>-1</sup> )	689.96	828.95	689.93
Crystal size(mm)	0.12 × 0.12 × 0.08	0.06 × 0.06 × 0.04	0.22 × 0.20 × 0.12
Space group	Immm	Immm	Immm
<i>a</i> (Å)	22.5959(10)	20.1311(16)	19.4476(7)
<i>b</i> (Å)	19.8166(5)	20.1311(16)	19.448(5)
<i>c</i> (Å)	19.817	20.5559(16)	24.1299(8)
<i>V</i> (Å <sup>3</sup> )	8873.4(5)	8330.5(11)	9126.2(4)
<i>Z</i>	8	8	8
$\lambda$ (Cu K $\alpha$ )( Å)	1.54178	1.54178	1.54178
<i>D</i> <sub>calcd</sub> (g cm <sup>-3</sup> )	1.046	1.322	1.014
$\mu$ (mm <sup>-1</sup> )	2.062	2.424	1.428
Temperature (K)	173(2)	173(2)	173(2)
Total reflections	32380	15364	23275
Unique data collected	3994	3685	4072

**Table 4.2** Continued

Observed reflections	2902	3389	2845
$R_{\text{int}}$	0.0607	0.0227	0.1209
Parameters	192	235	195
$R_1, wR(I > 2\sigma(I))^a$	0.1370	0.2437	0.1138
$R_1, wR(\text{all data})^b$	0.3971	0.6523	0.3525
$w = 1/(\sigma F_0)^2 + (aP)^2 + bP$	a = 0.2000,	a = 0.2000, b = 0.0000	a = 0.2000,
Goodness-of-fit-on $F^2$	1.603	1.238	1.251
$\Delta\rho_{\text{min}}$ and $\Delta\rho_{\text{max}}$ (e $\text{\AA}^{-3}$ )	-1.485, 2.729	-5.805, 7.290	-0.886, 1.826

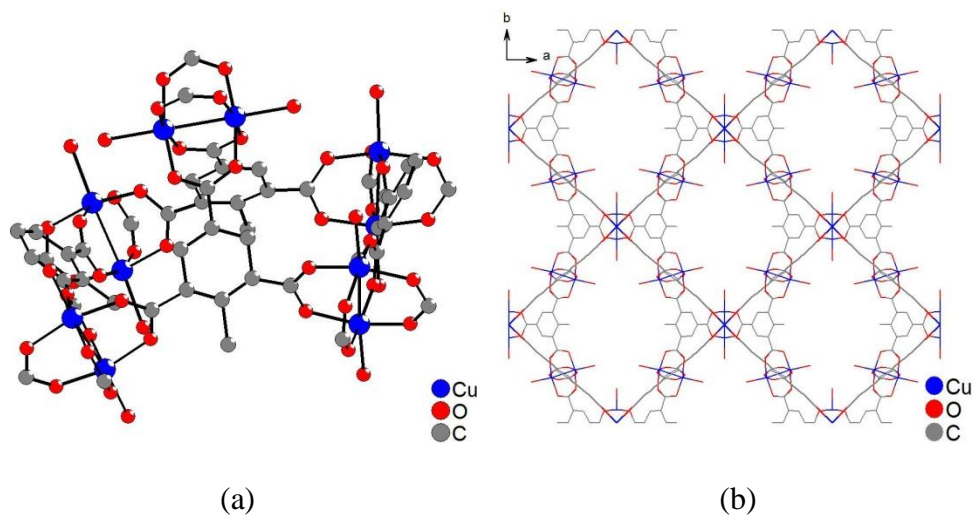
Single-crystal structure analyses reveal that these three MOFs share the same underlying topology. For convenience, I will use the fmj-methyl as an example to describe the structure of this series of materials. The framework of fmj-methyl is composed of two different dimeric cupric tetracarboxylate units, as shown in Figure 4.7. Cu1 and Cu1a (Cu2 and Cu2b) are each coordinated by one water molecule and four oxygen atoms from carboxyl groups. Each copper completes its pseudooctahedral coordination sphere with an axial aqua ligand opposite to the Cu-Cu vector. The modified BTC provides a two-fold symmetry element rather than three-fold due to the presence of the methyl groups. Cu<sub>1</sub><sub>2</sub>(O<sub>2</sub>C)<sub>4</sub> units and methyl groups are at ortho positions of the aromatic rings with a short Cu1-Cu1a internuclear separation of 2.65 Å, while Cu<sub>2</sub><sub>2</sub>(O<sub>2</sub>C)<sub>4</sub> units and methyl groups are at para positions of aromatic rings with a Cu2-Cu2b internuclear separation of 2.65 Å. As shown in Figure 4.7 (a), one tetracarboxylate unit provides a structural motif with potential four-fold symmetry. The other unit forms two-fold rotational symmetry along the line perpendicular to the Cu1-Cu1a vector in

Figure 4.7 (b). However, it does not form the same octahedral secondary building units (SBUs) as HKUST-1. Instead, the origin of the nanometer-sized channels can be considered as arising from the formation of smaller SBUs. As shown in Figure 4.8 (a), the key SBU in fmj-methyl is a pyramidal unit with Cu<sub>1</sub><sub>2</sub> dimers at its four bottom vertices, Cu<sub>2</sub><sub>2</sub> dimers at the top vertices of the pyramid, and two benzene rings at two of the four pyramidal faces of the pyramid. The fmj-ethyl and fmj-methoxy materials share similar dimeric cupric tetracarboxylate units and SBUs with fmj-methyl.



**Figure 4.7** Two different dicopper (II) tetracarboxylate building blocks of fmj-methyl

The final framework is achieved by connecting the SBU with other units through corner sharing of the pyramidal system. In Figure 4.8 (b), a view down the [001] direction of the cubic unit cell of fmj-methyl reveals ~1-nm-size channels with two-fold symmetry. The channels intersect to provide a 3D connected network of pores. The main channels are formed by connecting the cages shown in Figure 4.9 (a) by the windows shown in Figure 4.9 (b).



**Figure 4.8** Secondary building unit and the view of fmj-methyl MOF in [001] direction

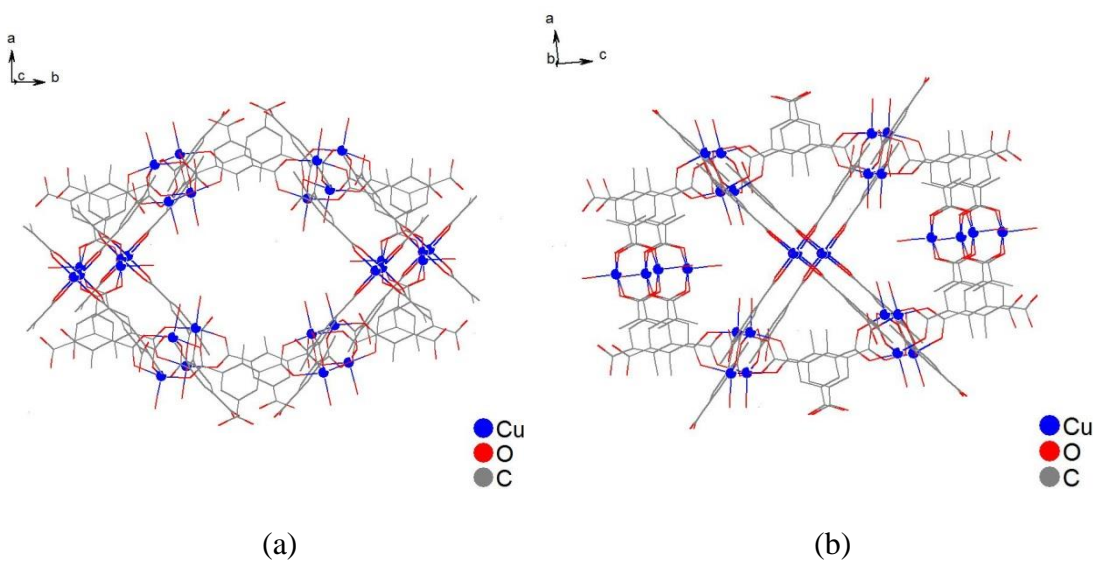


**Figure 4.9** The pore structure (a) and windows (b) which make the pores form 1D channels (b) of fmj-methyl

As shown in and Figure 4.9 (b) and Figure 4.10, the methyl, ethyl, and methoxy-functionalized ligands lead to the formation of the **fmj** topology. Considering the results in Chapter 3, the tagged materials with bromo, nitro, acetamide, and amino functional groups retain the same **tbo** topology as the parent HKUST-1 structure. The ligands with different tags can result in the formation of two different topologies with same 3,4-

connected net, which have not happened on the other systems,<sup>2-4,6,7,14</sup> such as UiO-66. Thus, this is good opportunity to examine how the functional groups affect the construction of MOFs.

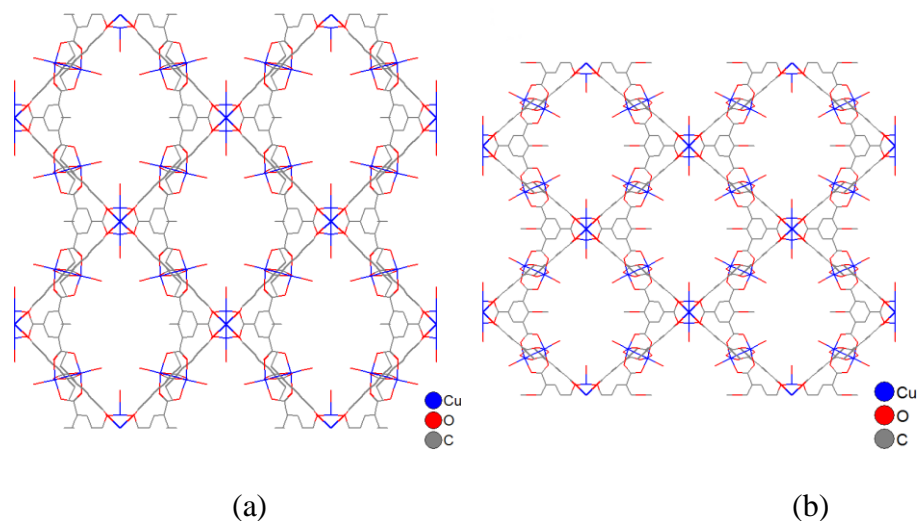


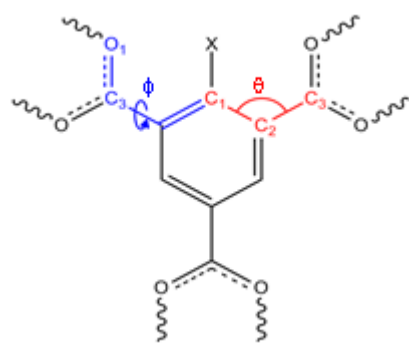
**Figure 4.10** View of the metal-organic frameworks fmj-ethyl(a) and fmj-methoxy(b) in the [001] direction

To understand the impact of functional groups on the construction of MOFs, it is useful to consider how individual ligands differ in the **tbo** and **fmj** topologies. The configuration of the BTC linker can be described by carboxylate torsion angles,  $\phi$  and  $C_1$ - $C_2$ - $C_3$  angles,  $\theta$  as shown in Figure 4.11 (a). First, I consider the **tbo** topology of HKUST-1. For the ideal **tbo** topology (Figure 4.11(b)), all three carboxylate groups lie in plane with the benzene ring, making  $\phi = 0^\circ$ . Additionally, the linker's three-fold symmetry and  $sp^2$  hybridization of  $C_2$  ensures that each  $\theta = 120^\circ$ . Unlike the **tbo** topology, the presence of functional groups in the fmj topology pushes away two ortho-carboxylate groups and causes them to be twisted out of the plane ( $\theta > 120^\circ$  and  $\phi > 0$ ). The third carboxylate group at the para position with respect to the functional group is

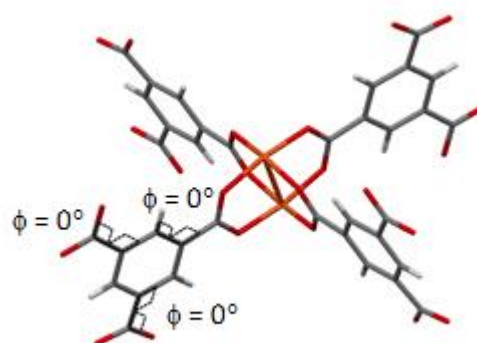
essentially unaffected. The SBU of the fmj topology consists of two types of linkers with different values of  $\theta$  and  $\phi$ . For example, the SBU of fmj-ethyl (Figure 4.11 (c)) has linkers with  $\theta = 130.7^\circ$ ,  $\phi = 34.5^\circ$  and  $\theta = 121.1^\circ$ ,  $\phi = 55.0^\circ$ . The  $\theta$  and  $\phi$  values of all the fmj materials are listed in Table 4.3. Considering that the methyl and ethyl are nonpolar functional groups, these two groups do not have strong affinity with ortho-carboxylate groups. The methyl and ethyl functional groups can push away ortho-carboxylate groups, which leads to  $\theta > 120^\circ$  and  $\phi > 0$ . The methoxy is polar functional group, which may result in a little stronger affinity with ortho-carboxylate groups than nonpolar functional groups, which can be confirmed by the smaller  $\theta$  than those of fmj-methyl and fmj-ethyl materials. However, the steric effect dominates the construction of MOFs and causes ortho-carboxylate groups to be twisted out of the plane as well, so the methoxy tags lead to the formation of fmj topology. The functional groups used for the construction of tagged HKUST-1 materials all are polar functional groups. They have stronger affinity with ortho-carboxylate groups than functional groups used in the fmj MOFs. The steric effect of these polar functional groups is not strong enough to cause ortho-carboxylate groups to be twisted out of the plane. Thus, the polarity of functional groups may have impact on the formation of topology: most of polar functional groups (acetamide, nitro, bromo, and amino) maintained the **tbo** topology of HKUST-1 materials, while nonpolar functional groups (methyl and ethyl) and the methoxy groups with weak polarity lead to the new CuBTC materials with **fmj** topology.

**Table 4.3** the  $\theta$  and  $\phi$  values of fmj-methyl, fmj-ethyl, and fmj-methoxy

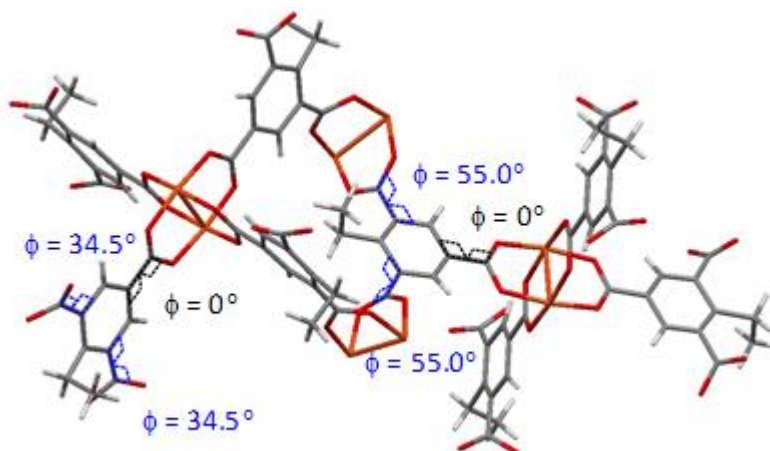
fmj-methyl		fmj-ethyl		fmj-methoxy	
$\theta$	$\phi$	$\theta$	$\phi$	$\theta$	$\phi$
131.6°	58.2°	130.7°	34.5°	122.59°	61.8°
126.1°	27.9°	121.1°	55.0°	120.23°	19.2°



(a)



(b)



(c)

**Figure 4.11** (a) Schematic of the BTC linker showing the  $sp^2$   $C_1-C_2-C_3$  angle,  $\theta$  (red) and carboxylate torsion angle,  $\phi$  (blue). For unfunctionalized BTC linkers,  $X = H$  while for

functionalized BTC linkers, X is replaced by the corresponding functional group.

Representative images for secondary building units (SBU) are shown for the (b) **tbo**, (c)

**fmj**

#### **4.4.2 Characterization of the Functionality of fmj-methoxy**

As shown in Figure 4.12, half of the methoxy groups in fmj-methoxy are decomposed to hydroxyl groups during the synthesis. Figure 4.13 indicates the experimental pXRD patterns of the bulk sample of fmj-methoxy material did not match the simulated pXRD patterns from the single crystal X-ray crystallographic study. Thus, there are multiple phases that appear to coexist in the fmj-methoxy bulk sample material. After modifying the synthesis parameters of the fmj-methoxy MOF, such as temperature and pH values, the pure fmj-methoxy material can be obtained. As shown in Figure 4.13, the pXRD patterns of as-synthesized materials obtained at modified synthesis conditions have good consistency with simulated pXRD patterns of desired fmj-methoxy material. The details about the optimization of the synthesis conditions for the fmj-methoxy material are discussed later in Chapter 7. However, we still need to verify the functional groups in fmj-methoxy material obtained at the modified synthesis condition. NMR studies were used to verify the presence of methoxy functional groups in the powder form material. As shown in Figure 4.14, there are only methoxy functional groups in powder materials of fmj-methoxy, while the methoxy functional groups in single crystal materials were partially decomposed to hydroxyl groups.

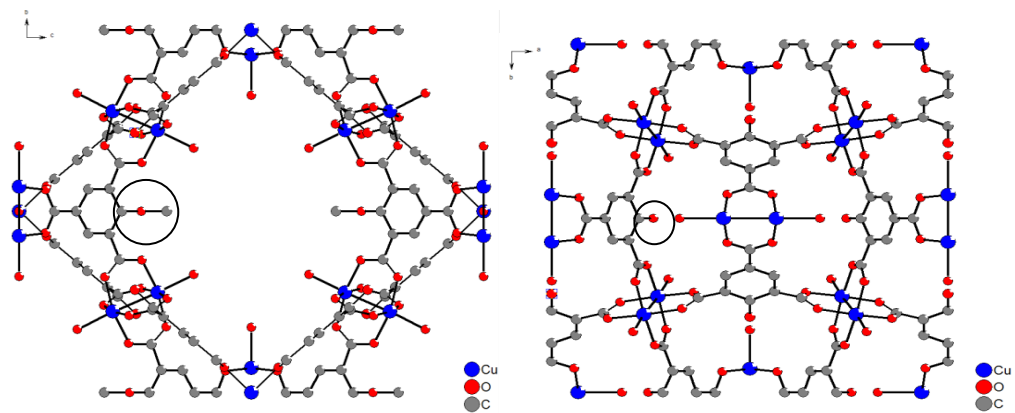


**Figure 4.12** Polymer frameworks of fmj-methoxy viewed down the [100] (a) and [010] (b) direction

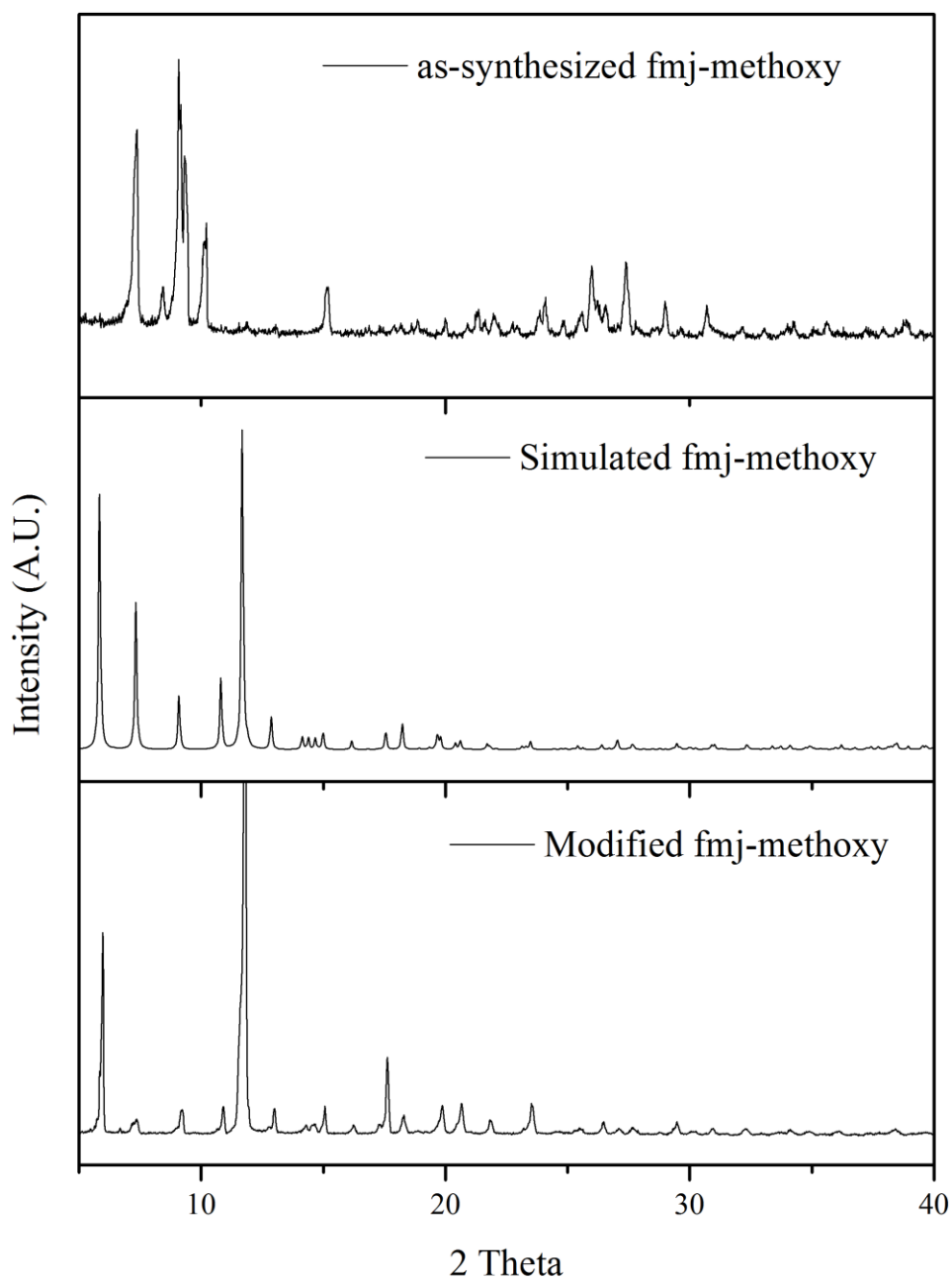
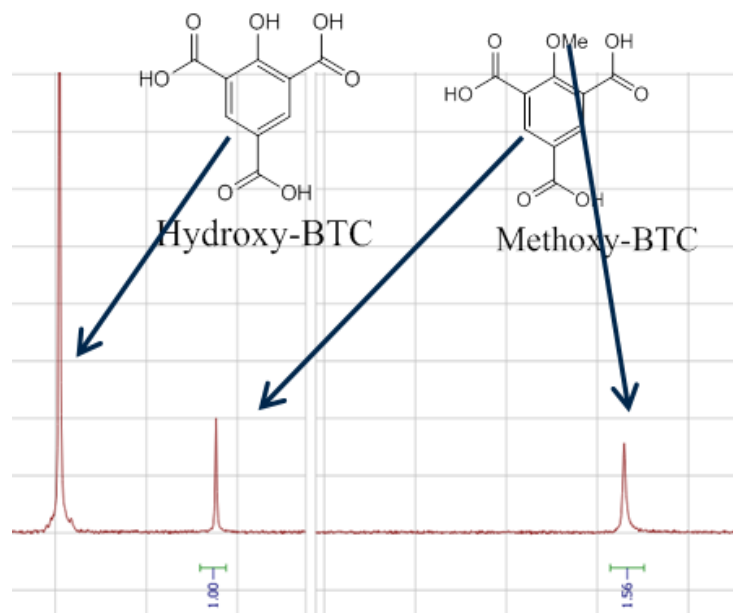
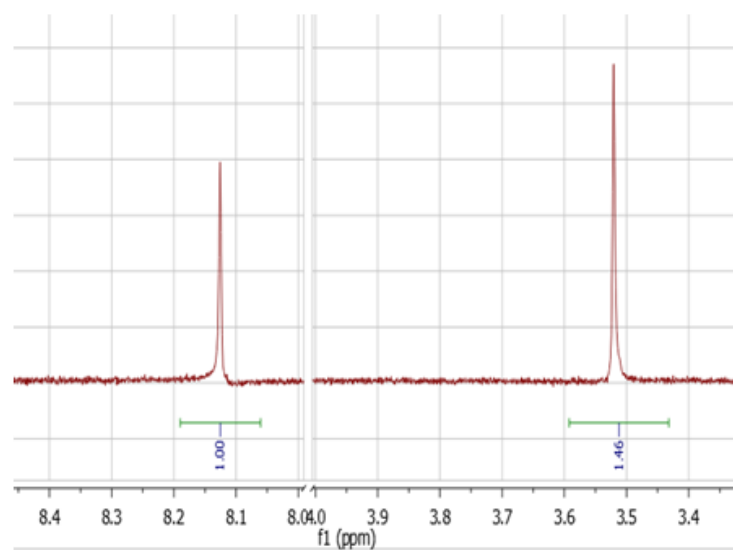


**Figure 4.13** Comparison among simulated pXRD, experimental pXRD of bulk phase materials for fmj-methoxy before and after the modification of the synthesis condition.



(a)



(b)

**Figure 4.14** NMR data of single crystal (a) of fmj-methoxy and powder material (b) of fmj-methoxy

### 4.4.3 Characterization of Powder Form Materials

Figure 4.15 shows that as-synthesized powder form materials of fmj-methyl, fmj-ethyl, and fmj-methoxy have the same structure with single crystals. Figure 4.16 - Figure 4.18 show the comparison between as-synthesized samples and activated ones for **fmj** series of MOFs. The pXRD patterns of fmj-methyl show that fmj-methyl retained their crystallinity after the activation. As shown in Figure 4.17 and Figure 4.18, some peaks are broadened for fmj-ethyl after activation, while some peaks are missing for fmj-methoxy material. This result indicates that fmj-ethyl and fmj-methoxy lose some of their crystallinity during the activation. Comparison between pXRD patterns for the activated samples of fmj-ethyl and fmj-methoxy shows that the fmj-ethyl is still better preserved than fmj-methoxy after activation. Generally speaking, considering the results from Chapter 3, the **tbo** series of MOFs have higher thermal stability than **fmj** systems, which is attributed to the topology differences, though the decomposition temperatures of **tbo** MOFs are lower than those of **fmj** series MOFs. The presence of functional groups in the **fmj** topology pushes away two ortho-carboxylate groups and causes them to be twisted out of the plane ( $\theta > 120^\circ$  and  $\phi > 0$ ), which may lead to the less thermally stable structure.

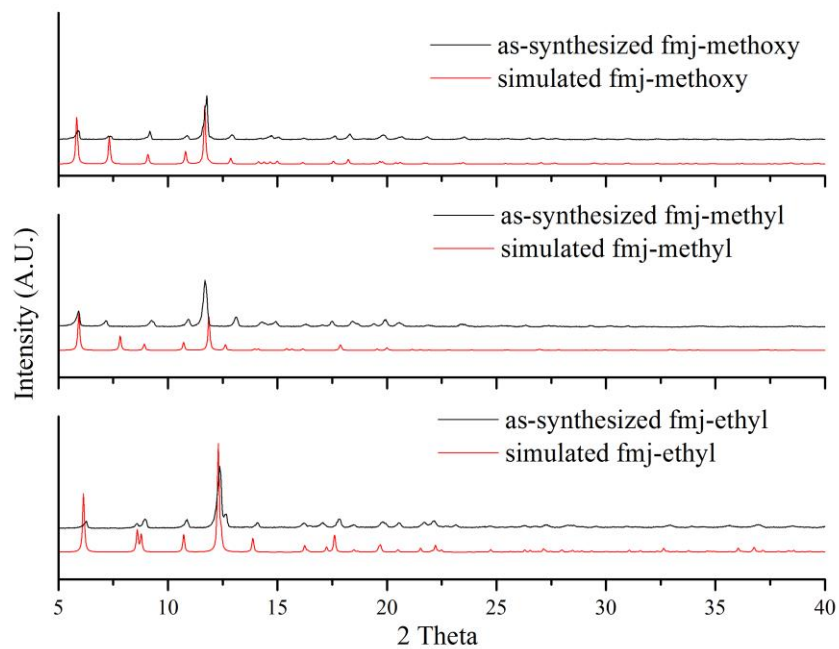


**Figure 4.15** Comparison of pXRD patterns and simulated pXRD patterns from single crystal data for as-synthesized fmj-methoxy (top), fmj-methyl (middle), and fmj-ethyl (bottom)

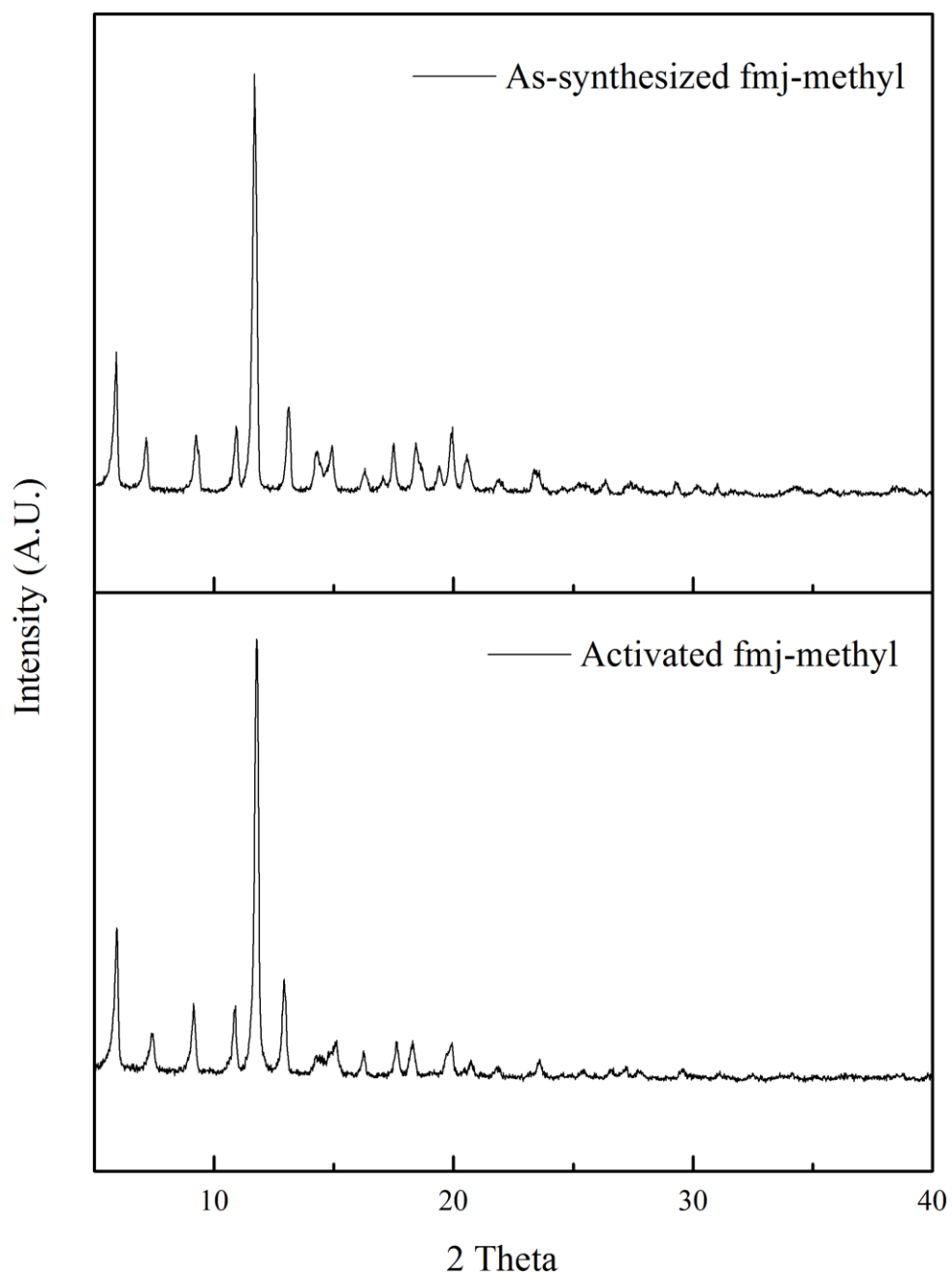


**Figure 4.16** pXRD diffractograms of as-synthesized (top) and activated (bottom) fmj-methyl

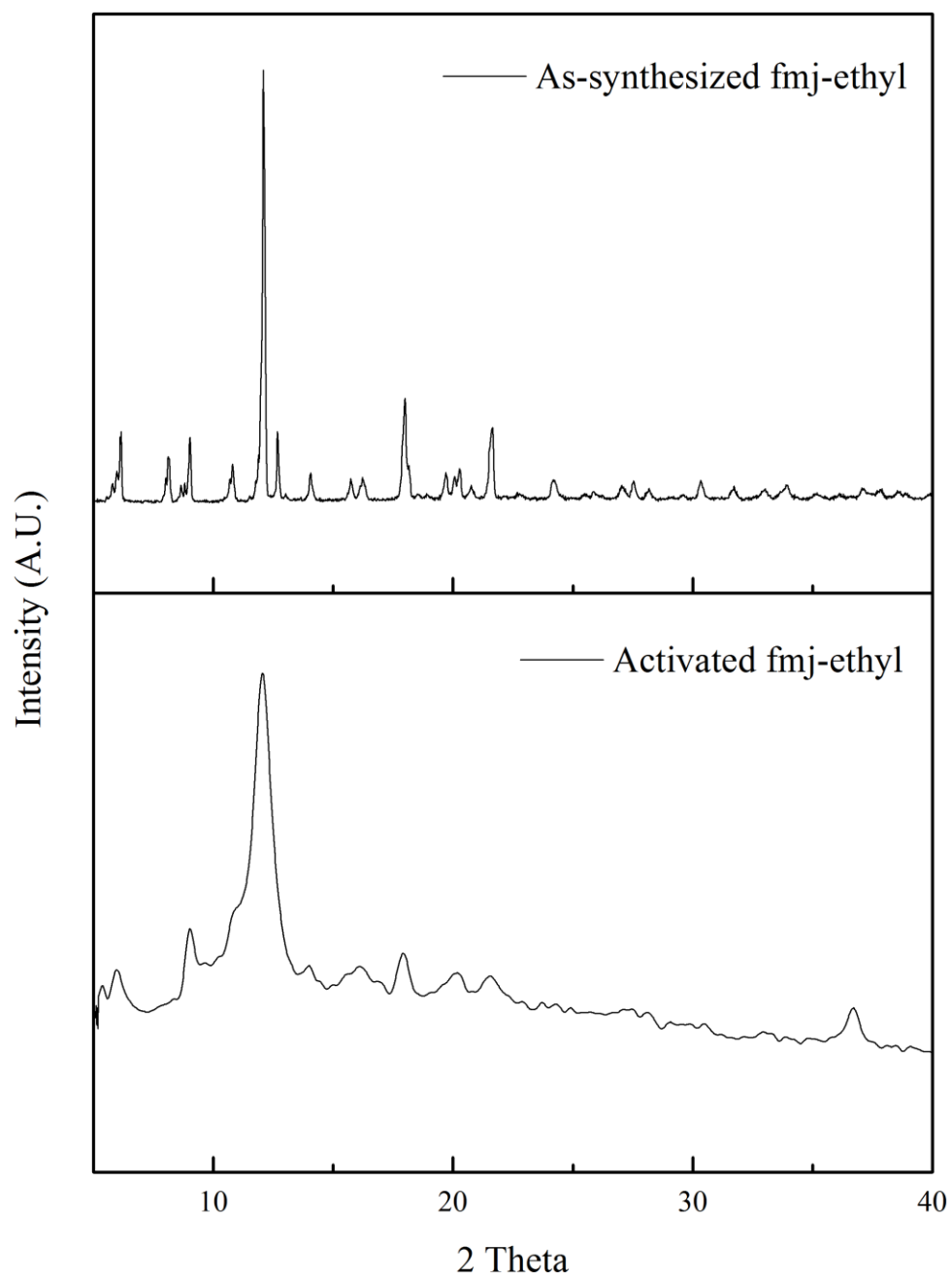


**Figure 4.17** pXRD diffractograms of as-synthesized (top) and activated (bottom) fmj-ethyl

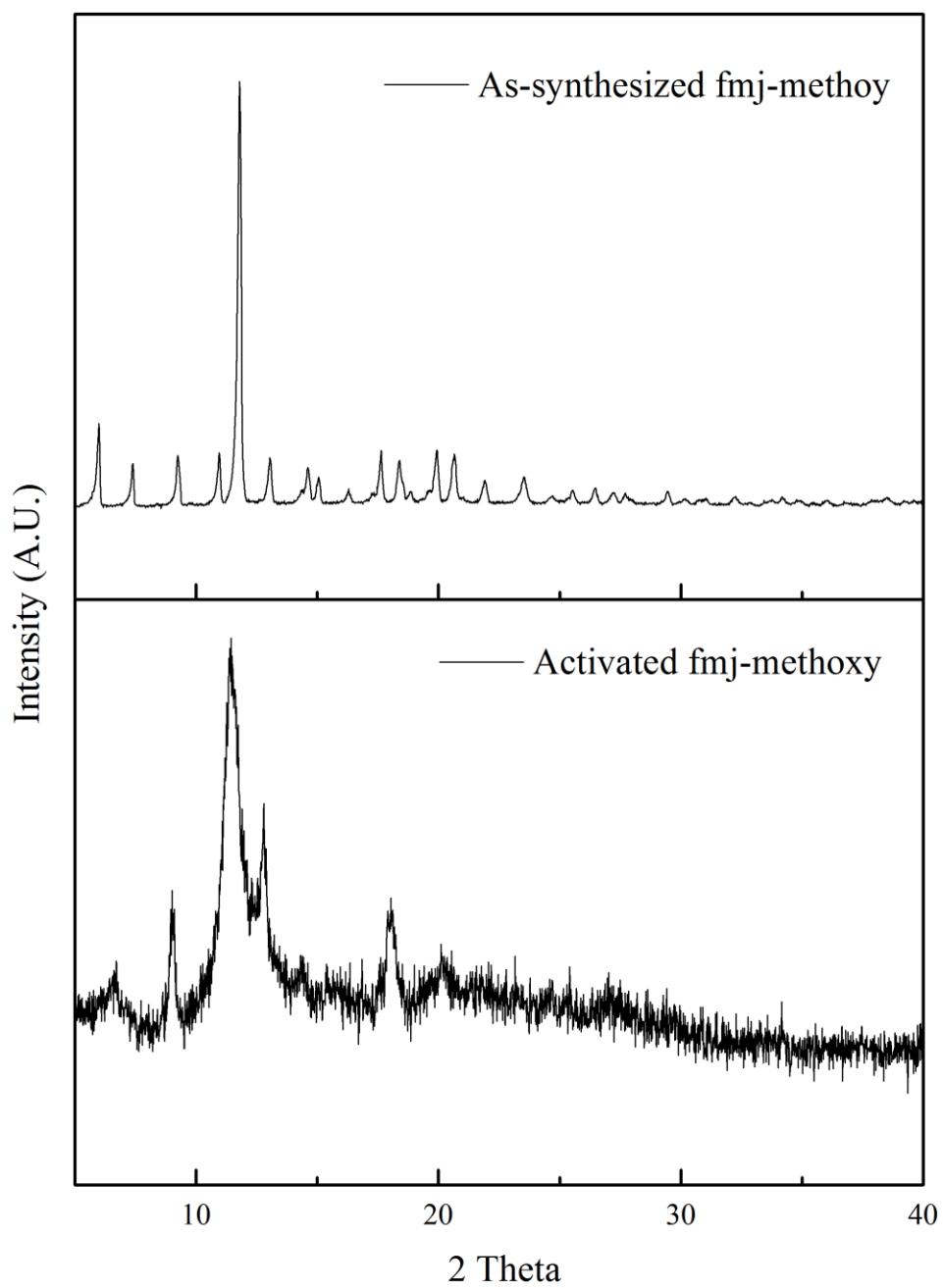


**Figure 4.18** pXRD diffractograms of as-synthesized (top) and activated (bottom) fmj-methoxy

## 4.5 Surface Area Analysis of MOFs

The accessible surface areas<sup>15</sup> for fmj-methyl, fmj-ethyl, and fmj-methoxy are calculated to compared the BET results from experimental isotherms (Figure 19 - Figure 21. Nitrogen adsorption isotherms for fmj-methyl, fmj-ethyl, and fmj-methoxy were used to obtain the BET surface areas of activated MOFs. The BET surface areas of fmj-methyl and fmj-ethyl are close to the calculated accessible surface areas, this result indicates fmj-methyl and fmj-ethyl were obtained in relatively pure phases and were properly activated and the broadening of the pXRD peaks of fmj-ethyl did not have effect on its BET surface area of fmj-ethyl. The fmj-methoxy material has relatively low BET surface areas, which may be attributed to the partial collapse of the structure during activation. The key observations from these experiments of **fmj** series MOFs are summarized in Table 4.4, which lists the experimental crystal structure of each material, and their measured surface areas and the accessible surface areas.

**Table 4.4** Observed Structure Topology, Synthesis Solvents, Accessible Surface Areas, and N<sub>2</sub> BET Surface Areas of **fmj** series MOFs

Linker	Solvent	Topology	Surface Area (m <sup>2</sup> /g)	
			Accessible <sup>15</sup>	BET
<b>methyl</b> *	DMF	<b>fmj</b>	1921	1471
<b>ethyl</b> *	Water/ EtOH	<b>fmj</b>	1563	1434
<b>Methoxy</b> *	DMF/ HCl sol.	<b>fmj</b>	1824	1259

\* Single crystal XRD structure has been solved

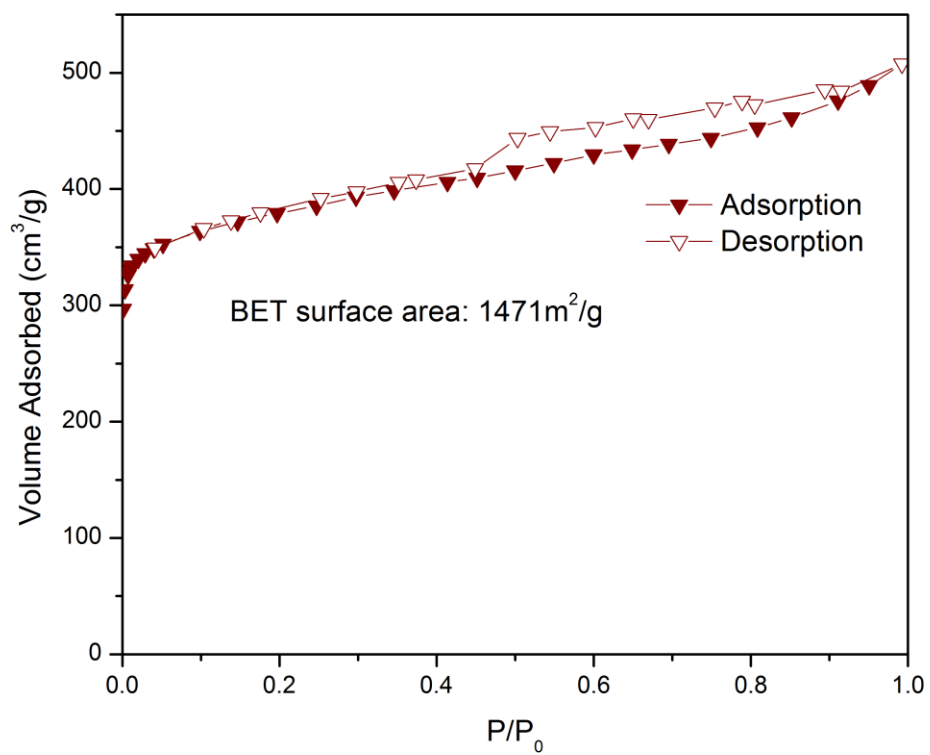


**Figure 4.19** Nitrogen isotherm of activated fmj-methyl at 77K (closed symbols – adsorption, open symbols – desorption)

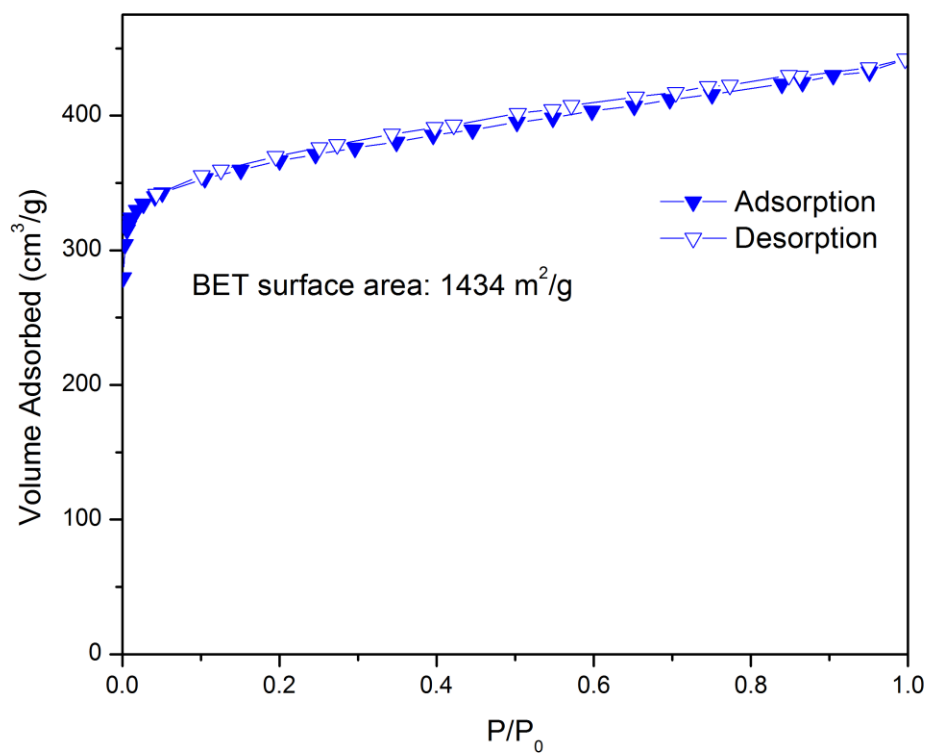


**Figure 4.20** Nitrogen isotherm of activated fmj-ethyl at 77K (closed symbols – adsorption, open symbols – desorption)

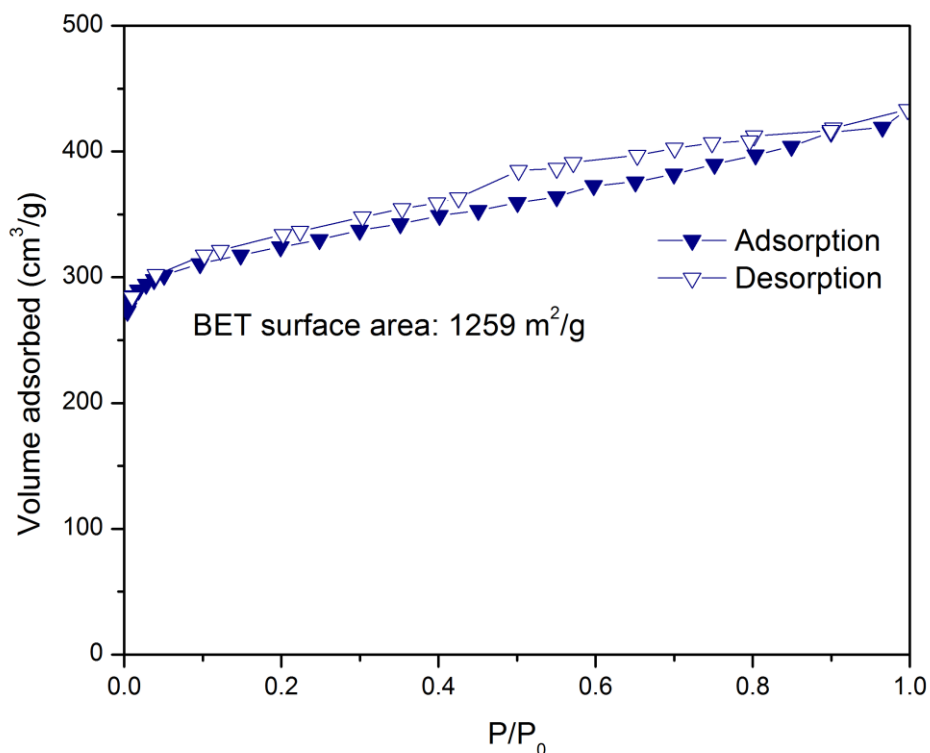


**Figure 4.21** Nitrogen isotherm of activated fmj-methoxy at 77K (closed symbols – adsorption, open symbols – desorption)

#### 4.5 Conclusions

In this chapter, I have successfully synthesized another three functionalized BTC ligands, methyl-BTC, ethyl-BTC, and methoxy-BTC. Instead of the formation of tagged HKUST-1, I synthesized three new tagged CuBTC under **fmj** topology systems. The synthesis procedure adopted for each **fmj** MOFs is slightly different with each other and also differs with respect to those of **tbo** series MOFs.<sup>16</sup> This result also indicates that the functional groups of ligands can have a dramatic effect on the synthesis environment. Combining the TGA results from Chapter 3 and Chapter 4, the missing of the plateaus only appears in the MOFs with polar functional groups. These results indicate that the

polar functional groups may increase the interaction between the solvated solvents and the surface of the adsorbents.

In Chapter 3 and Chapter 4, I have shown that functionalized HKUST-1 derivatives adopt multiple crystal structures. This is a striking example where inclusion of new functional groups in a MOF does not lead to an isostructural family of materials. These tagged materials with polar functional groups (bromo, nitro, acetamide, and amino) retain the same **tbo** topology as the parent HKUST-1 structure. The methyl, ethyl, and methoxy-functionalized ligands, however, lead to the formation of the **fmj** topology. The methyl and ethyl functional groups are nonpolar, while the methoxy group has a weak polarity. Thus, I conclude the polarity of functional groups has a significant impact on the topology: polar functional groups (acetamide, nitro, bromo, and amino) maintained the **tbo** topology of HKUST-1 materials, while nonpolar functional groups (methyl and ethyl) lead to the new CuBTC materials under **fmj** topology. The only exception is the methoxy functional group, where the polarity of methoxy functional group did not provide enough affinity with ortho-carboxylate groups for the formation of **tbo** structure and the steric effect of the functional group still dominated the construction of MOFs.

## 4.6 References

- 1 Kim, M., Boissonault, J. A., Allen, C. A., Dau, P. V. & Cohen, S. M. Functional tolerance in an isoreticular series of highly porous metal–organic frameworks. *Dalton Trans.* **41**, 6277-6282 (2012).
- 2 Yang, Q. *et al.* Functionalizing porous zirconium terephthalate UiO-66(Zr) for natural gas upgrading: a computational exploration. *Chem. Commun.* **47**, 9603-9605 (2011).
- 3 Cmarik, G. E., Kim, M., Cohen, S. M. & Walton, K. S. Tuning the adsorption properties of UiO-66 via ligand functionalization. *Langmuir* **28**, 15606-15613 (2012).
- 4 Kandiah, M. *et al.* Synthesis and stability of tagged UiO-66 Zr-MOFs. *Chem. Mater.* **22**, 6632-6640 (2010).
- 5 Huang, Y., Qin, W., Li, Z. & Li, Y. Enhanced stability and CO<sub>2</sub> affinity of a UiO-66 type metal-organic framework decorated with dimethyl groups. *Dalton Trans.* **41**, 9283-9285 (2012).
- 6 Couck, S. *et al.* An amine-functionalized MIL-53 metal-organic framework with large separation power for CO<sub>2</sub> and CH<sub>4</sub>. *J. Am. Chem. Soc.* **131**, 6326-6327 (2009).
- 7 Jasuja, H., Huang, Y.-g. & Walton, K. S. Adjusting the stability of metal-organic frameworks under humid conditions by ligand functionalization. *Langmuir* **28**, 16874-16880 (2012).
- 8 Dau, P. V., Tanabe, K. K. & Cohen, S. M. Functional group effects on metal-organic framework topology. *Chem. Commun.* **48**, 9370-9372 (2012).
- 9 Karagiari, O. *et al.* Synthesis and characterization of isostructural cadmium zeolitic imidazolate frameworks via solvent-assisted linker exchange. *Chem. Sci.* **3**, 3256-3260 (2012).
- 10 Blatov, V., Shevchenko, A. & Serezhkin, V. TOPOS3. 2: a new version of the program package for multipurpose crystal-chemical analysis. *J. Appl. Crystallogr.* **33**, 1193-1193 (2000).
- 11 Peikert, K., Hoffmann, F. & Froba, M. Amino substituted Cu<sub>3</sub>(btc)<sub>2</sub>: a new metal-organic framework with a versatile functionality. *Chem. Commun.* **48**, 11196-11198 (2012).
- 12 Schoenecker, P. M., Carson, C. G., Jasuja, H., Flemming, C. J. J. & Walton, K. S. Effect of water adsorption on retention of structure and surface area of metal-organic frameworks. *Ind. Eng. Chem. Res.* **51**, 6513-6519 (2012).

- 13 Liu, J. *et al.* Experimental and theoretical studies of gas adsorption in Cu<sub>3</sub> (BTC) 2: an effective activation procedure. *J. Phys. Chem. C* **111**, 9305-9313 (2007).
- 14 Lin, Y., Kong, C. & Chen, L. Direct synthesis of amine-functionalized MIL-101(Cr) nanoparticles and application for CO<sub>2</sub> capture. *R. Soc. Chem. Adv.* **2**, 6417-6419 (2012).
- 15 Düren, T., Millange, F., Férey, G., Walton, K. S. & Snurr, R. Q. Calculating geometric surface areas as a characterization tool for metal-organic frameworks. *J. Phys. Chem. C* **111**, 15350-15356 (2007).
- 16 Karra, J. R. & Walton, K. S. Effect of open metal sites on adsorption of polar and nonpolar molecules in metal-organic framework Cu-BTC. *Langmuir* **24**, 8620-8626 (2008).

# CHAPTER 5

## TUNING THE GAS ADSORPTION BEHAVIORS VIA FUNCTIONALIZATION OF BTC PRECURSORS

### 5.1 Introduction

A key issue in developing adsorption-based technologies, such as gas capture and separation, is the identification and synthesis of adsorbents that provide the proper adsorption capacities, selectivities, or reactivities for the application. The ability to modify the physical environment of the pores and cavities within MOFs would allow tuning of the interactions with guest species, and serves as a route to tailor the chemical stability and/or reactivity of the frameworks. These features make MOFs good candidates for adsorption-based applications.<sup>1-5</sup> Hence, there are an increasing number of studies dealing with gas adsorption in MOF materials including H<sub>2</sub>, CH<sub>4</sub>, N<sub>2</sub>, and CO<sub>2</sub>, among others.<sup>6-8</sup>

Perhaps the most attractive structural element of secondary building units in some MOFs is the open metal sites or coordinatively unsaturated centers which can be achieved in the metal clusters, such as paddle-wheel clusters, that have additional solvent molecules bound to them via a Lewis acid/base interaction.<sup>9,10</sup> After the removal of these solvent molecules, the coordinatively unsaturated centers exposed to the interior surface of the materials without detriment to the frameworks. These open metal sites, such as those found in HKUST-1 or MIL-100, have been shown to impart catalytic activity to the materials.<sup>11,12</sup> The partial positive charges on the open metal sites in MOFs also have a tremendous influence on the resulting adsorption properties. Several studies have demonstrated that the open metal sites greatly increase the ability of the materials to

adsorb the hydrogen molecules.<sup>13,14</sup> Many of studies have shown that the coordinatively unsaturated metal centers in MOFs are of paramount importance for selective adsorption of polar molecules over nonpolar molecules.<sup>15</sup> Thus, the further modification of MOFs including open metal sites, such as HKUST-1, for more specific application is a practical strategy for manipulating the adsorption behaviors.

Previous work has been done on the impact of functional groups on adsorption properties for a lot of MOF materials, such as UiO-66,<sup>16-19</sup> IRMOF,<sup>20,21</sup> and DMOF.<sup>22,23</sup> The published results indicate the most promising adsorption enhancements occur for certain polar functional groups, particularly amino, nitro, and hydroxyl functional groups, while the nonpolar functional groups, such as alkyl and naphthyl functionalities, can increase the hydrophobicity of parent materials.<sup>16,22,24</sup> However, the functional groups can interact with metal ions in a way that would interfere with MOF synthesis. For example, the reaction between methoxy functionalized BTB ligands and Zn (II) leads to the formation of functionalized MOF-177 which is isostructural MOF of MOF-177; the combination of hydroxy-BTB and Zn (II) generates the new MOF with interpenetrated pcu-e framework.<sup>25</sup>

In Chapter 3 and Chapter 4, we have focused on how the functional groups in BTC ligands affected the formation of the derivatives of HKUST-1 with different functionalities. I reported that the combination of BTC-X (acetamide, bromo, and nitro) ligands and Cu ions allows for the formation of functionalized HKUST-1 with bromo, acetamide and nitro functional groups under **tbo** topology. In contrast, the combination of BTC-X (methyl, ethyl and methoxy) and Cu ions generates the new CuBTC MOFs under **fmj** topology. This is a striking example where the combination of the metal clusters and

different functionalized ligands leads to two series of MOFs with same connectivity under different topologies. The two series of CuBTC MOFs with different topologies are closely related in such a way that 1) both assemble as a 3,4-connected network, 2) both possess copper paddle-wheel clusters with open metal sites, and 3) both have similar surface area, so the adsorption properties of these two series MOFs are comparable. Therefore, this chapter will focus on the systematic study of the impact of functionalization on the gas adsorption properties for the MOFs with open metal sites. Additionally, the isosteric heats of adsorption are calculated for each pure-component gas to estimate the extent of the interaction between the adsorbents and adsorbate molecules. The ideal selectivities based on the Henry's constant and the Ideal Adsorbed Solution Theory (IAST) were calculated to assess the impact of functional groups on the binary mixture selectivities compared with the parent HKUST-1 material.

## **5.2 Experimental Details**

### **5.2.1 Materials Synthesis and Activation**

All chemicals were commercially available and used as received without further purification. The functionalized ligands and two series of CuBTC MOFs were synthesized following procedure previous reported in Chapter 3 and Chapter 4. Activation procedures of all materials can be found in Chapter 3 and Chapter 4 as well.

### **5.2.2 Experimental Methods and Procedures**

The BET analysis is the standard method for determining surface areas by applying the theory of Brunauer, Emmett, and Teller (BET)<sup>26</sup> to nitrogen adsorption isotherms measured at 77K. The BET surface areas of MOF materials were calculated

from the experimental nitrogen isotherms at 77K in the range  $0.007 < P/P_0 < 0.05$ .<sup>27</sup> The nitrogen adsorption isotherms were measured at 77K using a QUADRASORB™ SI volumetric analyzer manufactured by Quantachrome Instruments. Single component gas adsorption isotherms were obtained using an Intelligent Gravimetric Analyser (IGA-001) from Hiden Isochema, which uses the gravimetric technique to measure gas sorption processes from vacuum to high pressure. All gases used in the adsorption experiments (CO<sub>2</sub>, CH<sub>4</sub>, and N<sub>2</sub>) were Ultra-High Purity or Bone Dry grade (Airgas).

## 5.3 Results and Discussion

### 5.3.1 Gas Adsorption Analysis

All the samples are activated under 170°C for 8 h to obtain the guest-free and fully dehydroxylated frameworks. The measurement of nitrogen isotherms at 77 K have allowed the BET surface areas to be quantified.<sup>26</sup> The BET surface area results are presented in Table 4.4. Considering the results from Chapter 4, the comparison between the pXRD patterns before and after activation for fmj-methoxy shows the methoxy tagged material may experience the partially decomposition of the structure. Compared with the accessible surface areas of fmj-methoxy, the BET surface area of fmj-methoxy has relatively low surface area, which may be attributed to this partial collapse of fmj-methoxy. The fmj-methoxy material still has the BET surface area of 1259 m<sup>2</sup>/g, so the pure component adsorption isotherms will be examined. However, the tbo-nitro has even lower BET surface area, much lower than its accessible surface area. Considering the consistency between pXRD patterns for tbo-nitro before and after activation, this result indicates that the sample has not been activated properly or the sample is not pure enough

for further application. Thus, in this chapter, we focused on the adsorption properties of HKUST-1, tbo-acetamide, tbo-bromo, fmj-methyl, fmj-ethyl, and fmj-methoxy.

The CO<sub>2</sub> adsorption measurements of all materials were carried out at 298 K and up to 20 bar, shown in Figure 5.1. These isotherms at the low pressure regime are shown in Figure 5.2. HKUST-1 shows slightly lower CO<sub>2</sub> and CH<sub>4</sub> adsorption than previously reported values. The discrepancy may be attributed to the different synthesis and activation procedures.<sup>28</sup> As we expected, the bromo functional group shows the highest uptakes among all the CuBTC MOFs investigated throughout the whole range of pressure, because the polar functional groups can enhance the interaction between the surface of adsorbents and the CO<sub>2</sub> adsorbate molecules. Though the acetamide is also a polar functional group, which may lead to the increase of CO<sub>2</sub> uptake, tbo-actemide has nearly identical loading with HKUST-1, probably due to the bulky shape of functional group. The bulky functional groups may have shielding effect on the open metal sites, which could result in the decrease of the CO<sub>2</sub> adsorbate molecule uptake. At low pressure regime, the methyl and ethyl functionalities exhibit lower loading than other materials. The nonpolar functional groups provide steric hindrance near the open metal sites, which may decrease the interaction between CO<sub>2</sub> molecules and open metal sites and lead to the lower uptake of CO<sub>2</sub> at low pressure regime. The fmj-methyl has the same uptake with HKUST-1 at 20 bar, which may be attributed to the same pore volume. The CO<sub>2</sub> uptake of fmj-methoxy is obviously lower than all other materials, due to the partial collapse of the structure.

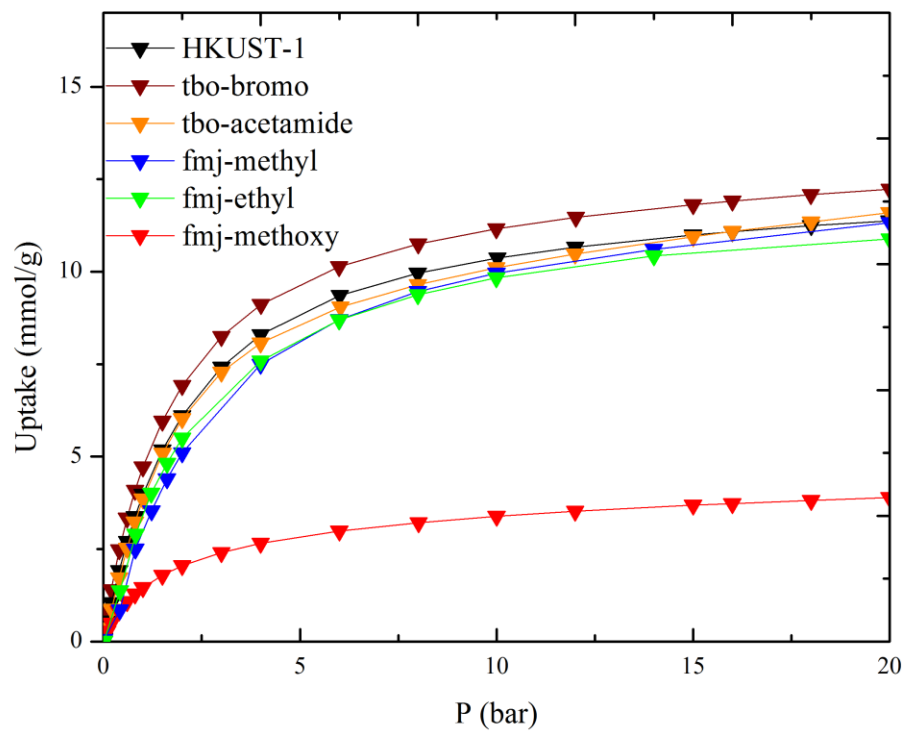


**Figure 5.1** CO<sub>2</sub> adsorption isotherms for samples at 25°C

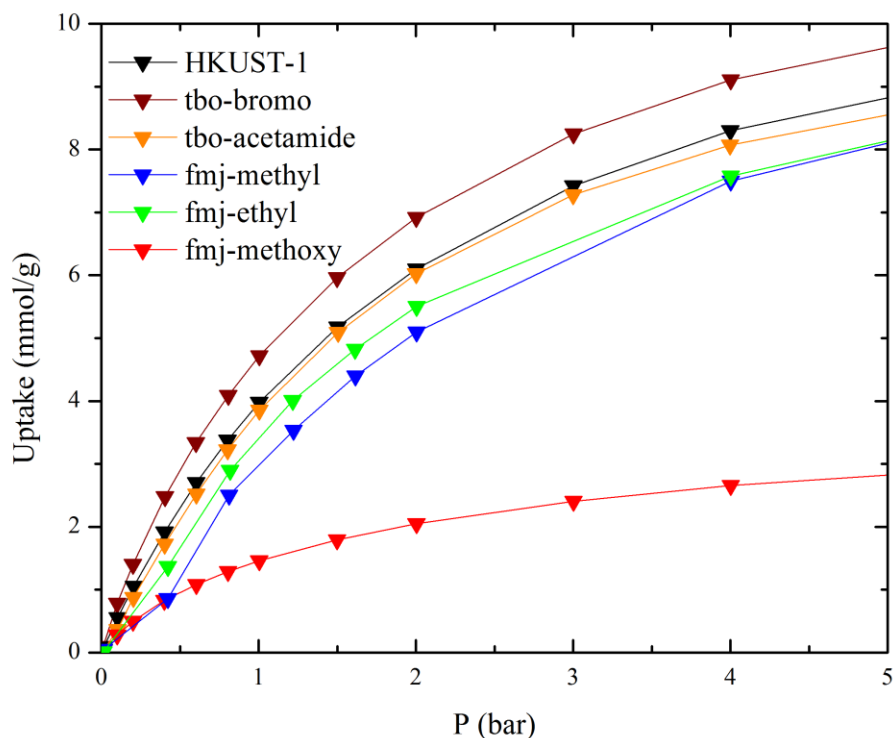


**Figure 5.2** CO<sub>2</sub> adsorption isotherms for samples at 25°C between 0-5 bar

The methane adsorption isotherms are collected up to 20 bar in Figure 5.3 and the low pressure regime of these isotherms is shown in Figure 5.4. MOFs with bulkier functional groups show slightly higher methane adsorption over the parent HKUST-1 materials at low pressure, following the order: acetamide > bromo > methyl. For example, the acetamide functionality shows highest adsorption loading at low pressure. The presence of acetamide functional group in the pores increases the van der Waals interaction between the methane molecule and the surface of the adsorbents, leading to relatively high methane uptake at low pressure. Methyl and ethyl groups have same trend of methane isotherms over all pressure range in the pressure range from 0 to 20 bar, due to the similar functionality of the fmj-methyl and fmj-ethyl materials; methyl has higher

uptake than ethyl over the entire pressure range, due to the BET surface area differences between these two materials. Like the CO<sub>2</sub> isotherm of fmj-methoxy, the fmj-methoxy still has lowest methane uptake due to partial decomposition of the structure. Considering the partially collapsed fmj-methoxy material, the calculations of its isosteric heat of adsorption and its CO<sub>2</sub>/CH<sub>4</sub> selectivity is not worthwhile, because this collapse of the adsorbent surface makes the comparison of the impact of the functional groups on the adsorption properties difficult. These results of the CO<sub>2</sub> and CH<sub>4</sub> isotherms for all materials show that the CH<sub>4</sub> adsorption isotherms do not have the similar trend to CO<sub>2</sub>. For CO<sub>2</sub> isotherms, the trend is based on the balance between the polarity and the shielding effect from the size differences; the polar functional groups can lead to the increase of CO<sub>2</sub> uptake and the bulky groups can block the access of CO<sub>2</sub> molecules to the open metal sites. However, for CH<sub>4</sub> isotherms, the trend mainly depends on the size of the functional groups.

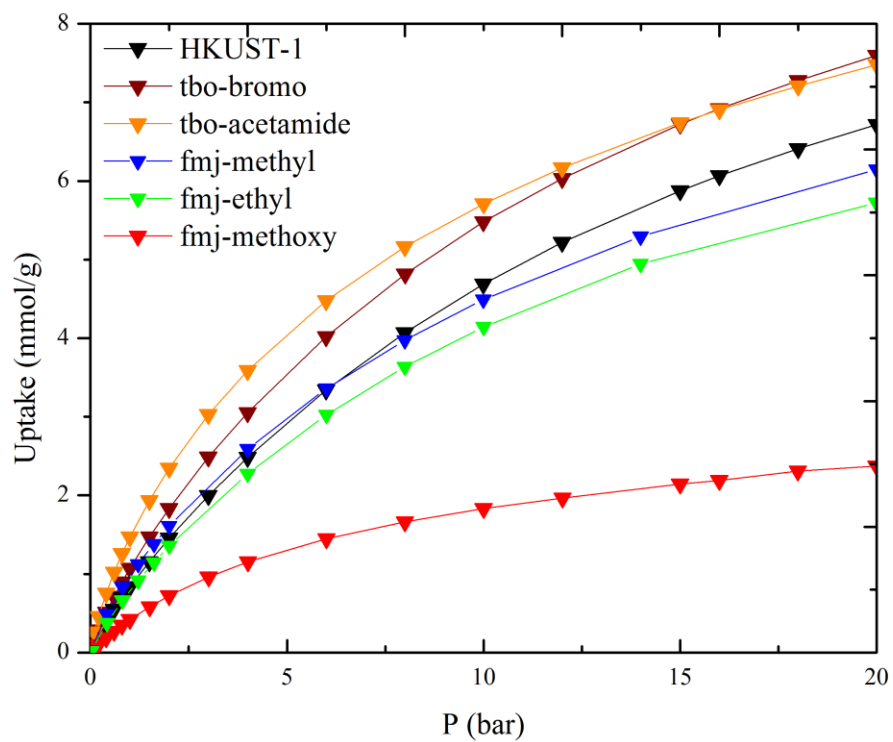


**Figure 5.3** CH<sub>4</sub> adsorption isotherms for samples at 25°C

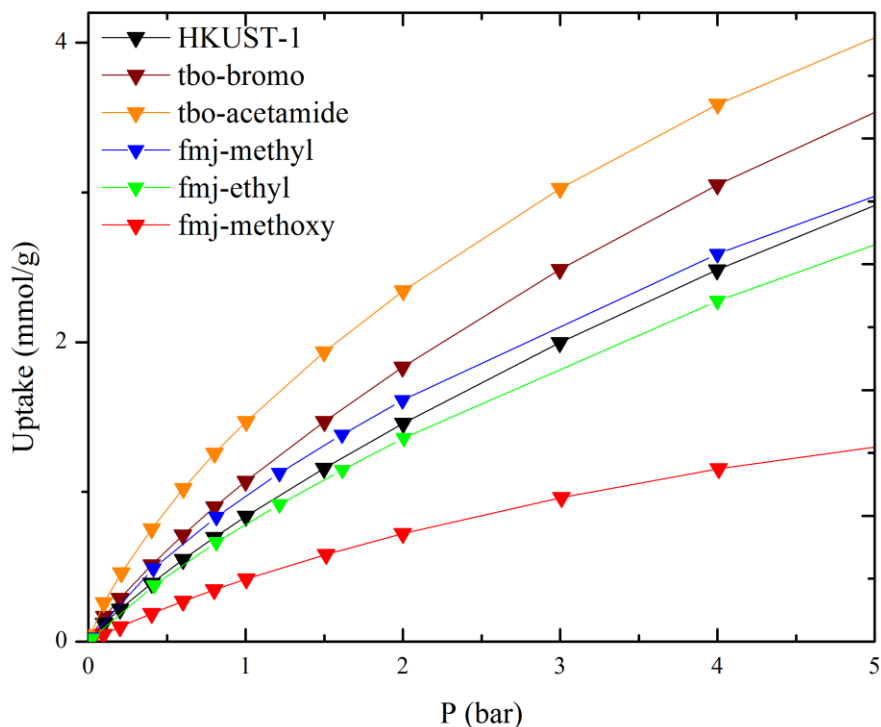


**Figure 5.4** CH<sub>4</sub> adsorption isotherms for samples at 25°C between 0-5 bar

### 5.3.2 Heat of Adsorption

The isosteric heat of adsorption is important parameter for industrial processes, because the heat released during the adsorption step can create temperature waves through the adsorption bed and decrease the efficiency of the process.<sup>29</sup> The isosteric heat of adsorption is the basic foundation of any adsorbent and adsorbate system, corresponding to the interaction between the adsorbate molecules and the surface of the adsorbent. The isosteric heats of adsorption for HKUST-1 tbo-acetamide, tbo-bromo, fmj-methyl, and fmj-ethyl will be calculated in this work to understand the interaction between the gas molecules and the adsorbent surfaces.

The CO<sub>2</sub> isotherms are fit to the Toth equation,<sup>30</sup>

$$n = n_s \frac{bP}{[1 + (bP)^t]^{1/t}} \quad (1)$$

where  $P$  is equilibrium pressure,  $b$  is the adsorbent affinity,  $n$  is the adsorption loading,  $n_s$  is the maximum loading corresponding to complete monolayer coverage, and  $t$  is a parameter which is typically  $< 1$ , describing the heterogeneity of the adsorbent surface.

The methane isotherms are fit to the Langmuir equation,<sup>30,31</sup>

$$n = n_s \frac{bP}{1 + bP} \quad (2)$$

where  $n$ ,  $P$ ,  $n_s$  used are the same as in the Toth equation, and the constant  $b$  is the Langmuir adsorption constant and increases with an increase in the binding energy of adsorption and with a decrease in temperature.

The isosteric heat of adsorption for CO<sub>2</sub> and CH<sub>4</sub> was calculated using the Clausius-Clapeyron equation<sup>30</sup> up to 2 bar,

$$\frac{Q_{st}}{RT^2} = - \left( \frac{\partial \ln P}{\partial T} \right)_q \quad (3)$$

where  $Q_{st}$  is isosteric heat of adsorption,  $T$  is temperature, and  $P$  is equilibrium pressure.. Under low pressure regime (below 10 bar), the difference between the heats of adsorption with or without considering buoyance correction is negligible, so the experimental data were directly used to fit the models.

The calculated isosteric heats of adsorption of CO<sub>2</sub> and CH<sub>4</sub> for HKUST-1, tbo-acetamide, tbo-bromo, fmj-methyl and fmj-ethyl are shown in Figure 5.5 and Figure 5.6 respectively. The isosteric heats of adsorption of CO<sub>2</sub> and CH<sub>4</sub> for HKUST-1 are slightly lower than the previous published data,<sup>32</sup> probably due to the usage of different fitting models. For CO<sub>2</sub> heat of adsorption in HKUST-1, as loading increases, the calculated

heat of adsorption drops slightly from 28.2 to 27.5 kJ/mol. The heats of adsorption of other MOFs were not previously reported. The high isosteric heat of adsorption of tbo-bromo at CO<sub>2</sub> low loading indicates the existence of strong adsorption sites, which is consistent with the high CO<sub>2</sub> uptake shown in Figure 5.1. As loading increases, the heat of adsorption of tbo-bromo converges to 26 kJ/mol with HKUST-1. Surprisingly, the acetamide functionality has lower  $Q_{st}$  than HKUST-1, which may be attributed to the shielding effect of the acetamide group, due to its bulky shape. As shown in Figure 5.5, the methyl and ethyl nonpolar functional groups can decrease the  $Q_{st}$  of the parent material. The adsorbents with nonpolar functional groups, methyl and ethyl, have lower heats of adsorption at low CO<sub>2</sub> loading than other polar functionalized MOFs. This behavior suggests that the nonpolar groups have a negative effect on CO<sub>2</sub> adsorption, because the nonpolar groups have a steric effect on CO<sub>2</sub> molecules and block CO<sub>2</sub> access to open metal sites. These results indicate that heats of adsorption for CO<sub>2</sub> in these derivatives of HKUST-1 not only depend on the polarity of functional groups, but also on the accessible pore space experienced by the adsorbate molecules.

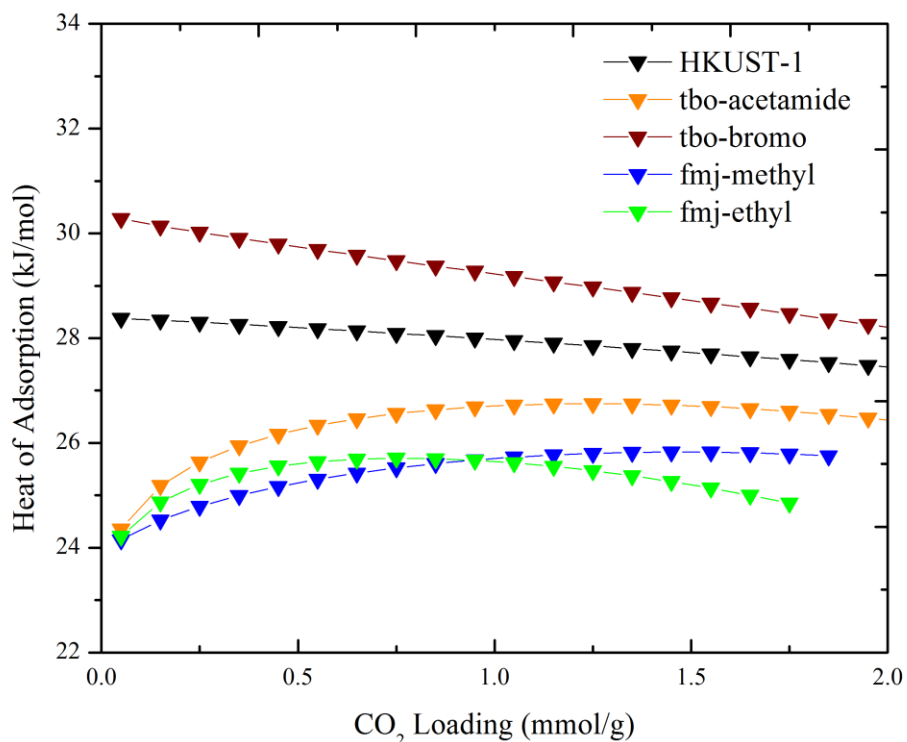


**Figure 5.5** Isosteric heats of adsorption as a function of CO<sub>2</sub> loading

The methane isosteric heats of adsorption of all materials increase as methane loading increases, shown in Figure 5.6. The acetamide functionality provides the highest  $Q_{st}$  among other functionalized MOF. This behavior is consistent with the high methane uptake. Bromo-functionalized HKUST-1 has higher  $Q_{st}$  than the parent material. At low CH<sub>4</sub> loading, the heats of adsorption increase when the functional group becomes bulkier, following the order: acetamide > bromo > ethyl > methyl. These results showed that the size of the functional groups has strong effect on the interaction between CH<sub>4</sub> molecules and the adsorbent surface. The larger functional groups increase the van der Waal interaction between adsorbents and the methane molecules.

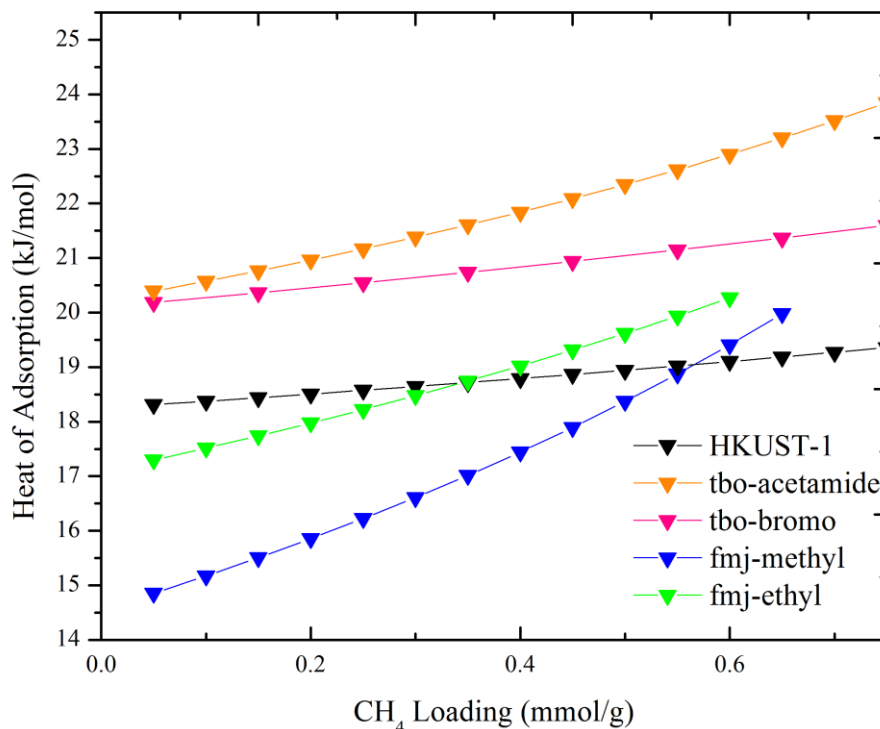


**Figure 5.6** Isosteric heat of adsorption as a function of CH<sub>4</sub> loading

### 5.3.3 CO<sub>2</sub>/ CH<sub>4</sub> Selectivity

The removal of carbon dioxide from methane is a critical issue for natural gas transportation and usage in which corrosion of equipment and pipelines must be prevented. Selectivity is a critical parameter for characterizing the separation properties of materials. Here, we employed two ways to calculate the CO<sub>2</sub>/CH<sub>4</sub> selectivity: calculating the ratio of the Henry's constants for CO<sub>2</sub> and CH<sub>4</sub> was employed to determine the ideal selectivity of MOF materials;<sup>33</sup> and IAST was used to predict binary mixture adsorption from the experimental pure-gas isotherms. The incorporation of functional sites may induce stronger interactions with carbon dioxide than nonpolar gas molecules, such as methane, and result in the increase of the CO<sub>2</sub>/CH<sub>4</sub> separation

selectivity. For example, adding hydroxyl groups to the DMOF-1 material dramatically enhanced the interactions between CO<sub>2</sub> molecules and the surface of the adsorbent. Accordingly, CO<sub>2</sub>/CH<sub>4</sub> separation selectivity in the hydroxyl functionalized DMOF-1 (UTSA-25a) of 12.5 is much higher than the one of 3.7 in DMOF-1 at 296 K.<sup>34</sup> In this work, the calculation of the CO<sub>2</sub>/CH<sub>4</sub> selectivities based on the Henry's constant and IAST was used to predict the CO<sub>2</sub>/CH<sub>4</sub> separation behaviors of all materials.

The Toth equation and Langmuir equation have been used to fit the CO<sub>2</sub> and CH<sub>4</sub> isotherms. The calculation of the Henry's constant is simply the product of adsorption affinity,  $b_i$ , and the maximum loading corresponding to complete monolayer coverage,  $n_{si}$ , given in the following equation,

$$H_i = n_{si} \times b_i \quad (4)$$

Table 5.1 shows the ideal CO<sub>2</sub>/CH<sub>4</sub> selectivity at 298, 308, and 318 K as determined from a ratio of Henry's constants. The polar functional groups, acetamide and bromo have significantly higher ideal selectivities for CO<sub>2</sub> over CH<sub>4</sub> compared to the parent MOF (HKUST-1). The nonpolar functionalized materials, fmj-methyl and fmj-ethyl have lower selectivity than HKUST-1, probably due to the enhanced interaction between nonpolar functional groups with methane molecules.

**Table 5.1** The Ratio of Henry's Constants for CO<sub>2</sub>/CH<sub>4</sub> Binary Gas Mixture at 298, 308, and 318 K

T(K)	HKUST-1	tbo-acetamide	tbo-bromo	fmj-methyl	fmj-ethyl
298	5.342957	5.655126	6.351332	3.812861	4.603702
308	4.572934	5.937095	5.415489	3.486322	4.2314
318	4.13211	5.322629	4.895561	3.015515	3.972556

From the single-component CO<sub>2</sub> and CH<sub>4</sub> isotherms, mixture adsorption was predicted using the ideal adsorbed solution theory (IAST). It has been reported that IAST can accurately predict gas mixture adsorption in many zeolites<sup>35-37</sup> and MOF materials.<sup>9,35,38</sup> Although other theories exist for such predictions, IAST continues to serve as the benchmark for prediction of mixed-gas adsorption equilibria from single component isotherms.<sup>35,38-40</sup> In order to perform the integrations required by IAST, the single-component isotherms should be fitted by a proper model. There is no restriction on the choice of the model to fit the adsorption isotherm, but data over the pressure range under study should be fitted very precisely. Thus, we still used the Toth equation to fit the CO<sub>2</sub> isotherms and the Langmuir model to fit the CH<sub>4</sub> isotherms. The fitted isotherm parameters were applied to perform the necessary integrations in IAST. The selectivity  $S_{i/j}$  in a binary mixture of components  $i$  and  $j$  is defined as  $(x_i/y_i)/(x_j/y_j)$ , where  $x_i$  or  $x_j$  and  $y_i$  or  $y_j$  are the mole fractions of component  $i$  or  $j$  in the adsorbed and bulk gas phases, respectively. Figure 5.7 and Figure 5.8 show the adsorption selectivities of an equimolar mixture of CO<sub>2</sub>/CH<sub>4</sub> and 5:95 mixture of CO<sub>2</sub>/CH<sub>4</sub> in all materials as a function of total bulk pressure.

Figure 5.7 shows that CO<sub>2</sub> is preferentially adsorbed over CH<sub>4</sub> from their binary mixture in all adsorbents due to the quadruple moment of CO<sub>2</sub> molecules. In all materials, when the bulk pressure is close to zero, the adsorption selectivity calculated from IAST is approximately equal to the ratio of the Henry's constant. In all the six adsorbents, the selectivities decrease slowly as the pressure increases. At low pressure, there are more CO<sub>2</sub> molecules adsorbed on the surface of materials than methane due to the stronger affinity between the open metal sites and the CO<sub>2</sub>, while at high pressure, all the strong

surface adsorption sites are taken, which results in that the decrease of selectivities. At low pressure, the bromo polar functional groups have higher selectivity than HKUST-1 and nonpolar functionalized materials, because the polar functional groups can increase the interaction between the adsorbent surface and CO<sub>2</sub> molecules. At the highest pressure, HKUST-1 has highest adsorption selectivity, probably because the van der Waal interactions between CH<sub>4</sub> and the surface of adsorbent in functionalized materials are higher than parent HKUST-1 material, which results in a decrease of the selectivities at high pressure. The tbo-acetamide, fmj-methyl, and fmj-ethyl have the similar selectivities; as pressure increase, the selectivities decrease. However, the tbo-acetamide still has a higher selectivity than fmj-methyl and fmj-ethyl at low pressure, due to the polarity of tbo-acetamide, which leads to the stronger affinity between the CO<sub>2</sub> molecules and the adsorbent surface than methyl and ethyl functionalized materials.

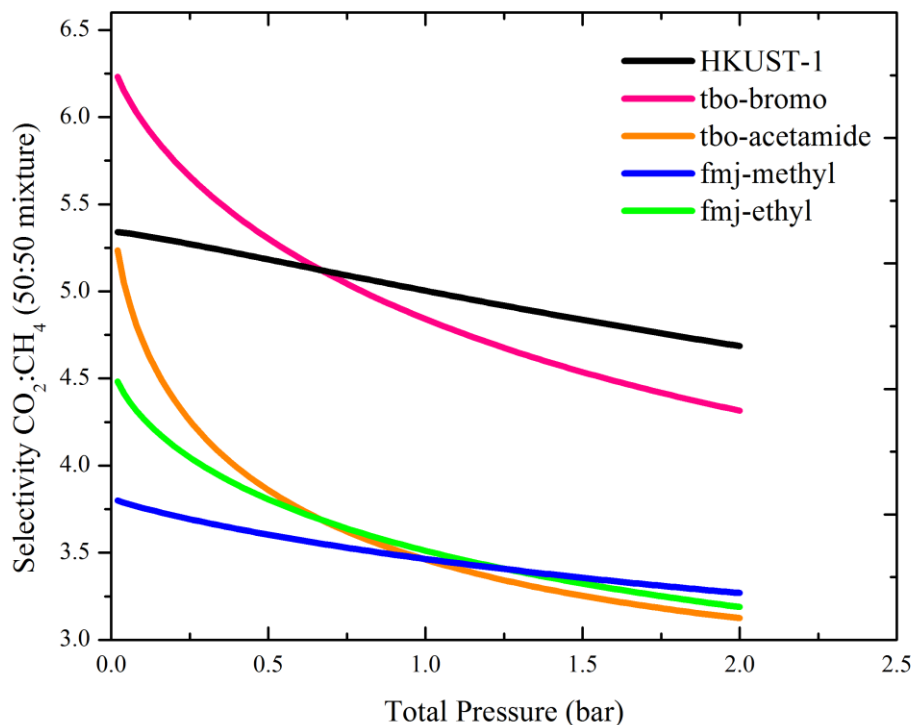


**Figure 5.7** Selectivity by applying IAST for a 50:50 CO<sub>2</sub>/CH<sub>4</sub> gas mixture at 25°C

Natural gas (NG) is composed of a high concentration of methane (80%) with other hydrocarbons (C<sub>2+</sub>) in variable quantities and several impurities in small quantities, such as carbon dioxide. Considering the composition of natural gas, we also calculated the 5:95 CO<sub>2</sub>/CH<sub>4</sub> mixture selectivity as well. In all the six adsorbents, the adsorption selectivities increase slowly as the pressure increases. Figure 5.8 indicates the polar functional groups slightly outperform other MOFs in CO<sub>2</sub>/CH<sub>4</sub> selectivities along the whole pressure range, because polar functional groups have positive effect on the CO<sub>2</sub> adsorption. The nonpolar functional groups have lower CO<sub>2</sub>/CH<sub>4</sub> selectivities than HKUST-1, because the nonpolar functional groups increase the methane molecule uptake which leads to low CO<sub>2</sub>/CH<sub>4</sub> selectivities. Compared with the 50:50 mixture of CO<sub>2</sub> and

CH<sub>4</sub>, the selectivities of all materials in 5% CO<sub>2</sub> mixture are higher than in the 50:50 mixture. Because of the low percentage of CO<sub>2</sub>, most of the CO<sub>2</sub> molecules could be adsorbed on the open metal sites due to the quadruple moment, which leads to the higher selectivities than 50% CO<sub>2</sub> mixture.

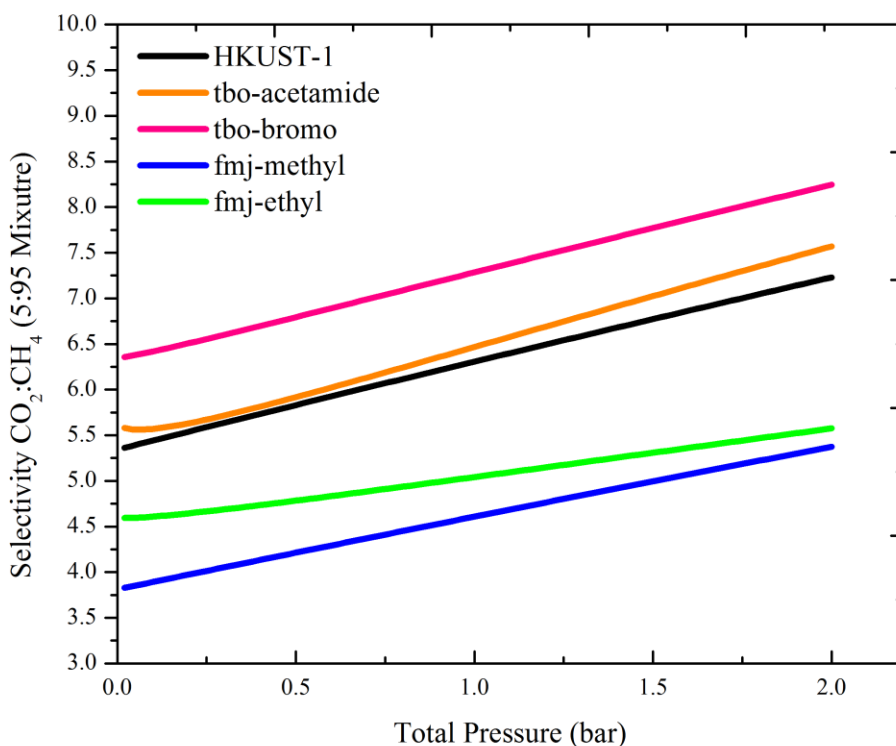


**Figure 5.8** Selectivity by applying IAST for a 5:95 CO<sub>2</sub>/CH<sub>4</sub> gas mixture at 25°C

#### 5.4 Conclusions

The adsorption properties of CuBTC MOFs with methyl, ethyl, methoxy, acetamide and bromo functionality were studied. Generally, the polar functional groups improve the CO<sub>2</sub> uptake, while nonpolar functionalities, methyl and ethyl, decrease the CO<sub>2</sub> uptake under low pressure. Based on the isosteric heats of adsorption, the bulky

functional groups enhance the interaction of CH<sub>4</sub> and adsorbent at low loading, following the order: acetamide > bromo > ethyl > methyl. General speaking, the polar functional groups slightly outperform other MOFs in CO<sub>2</sub>/CH<sub>4</sub> selectivities, because polar functional groups have positive effect on the CO<sub>2</sub> adsorption. The nonpolar functional groups have lower CO<sub>2</sub>/CH<sub>4</sub> selectivities than HKUST-1, because the nonpolar functional groups increase the methane molecule uptake which leads to low CO<sub>2</sub>/CH<sub>4</sub> selectivities. Therefore, this work demonstrates that the pre-functionalization method could be used to manipulate the adsorption behaviors of MOF materials.

## 5.5 References

- 1 Eddaoudi, M. *et al.* Systematic design of pore size and functionality in isorecticular MOFs and their application in methane storage. *Science* **295**, 469-472 (2002).
- 2 Kitagawa, S., Kitaura, R. & Noro, S. Functional porous coordination polymers. *Angew. Chem. Int. Ed.* **43**, 2334-2375 (2004).
- 3 James, S. L. Metal-organic frameworks. *Chem. Soc. Rev.* **32**, 276 (2003).
- 4 Ferey, G. Hybrid porous solids: past, present, future. *Chem. Soc. Rev.* **37**, 191-214 (2008).
- 5 Garberoglio, G., Skoulidas, A. I. & Johnson, J. K. Adsorption of gases in metal organic materials: comparison of simulations and experiments. *J. Phys. Chem. B* **109**, 13094-13103 (2005).
- 6 Morris, R. E. & Wheatley, P. S. Gas storage in nanoporous materials. *Angew. Chem. Int. Ed.* **47**, 4966-4981 (2008).
- 7 Wang, S., Yang, Q. & Zhong, C. Adsorption and separation of binary mixtures in a metal-organic framework Cu-BTC: A computational study. *Sep. Purif. Technol.* **60**, 30-35 (2008).
- 8 Furukawa, H. *et al.* Ultrahigh porosity in metal-organic frameworks. *Science* **329**, 424-428 (2010).
- 9 Mu, B., Li, F. & Walton, K. S. A novel metal-organic coordination polymer for selective adsorption of CO<sub>2</sub> over CH<sub>4</sub>. *Chem. Commun.*, 2493-2495 (2009).
- 10 Guo, Z. *et al.* A metal-organic framework with optimized open metal sites and pore spaces for high methane storage at room temperature. *Angew. Chem. Int. Ed.* **50**, 3178-3181 (2011).
- 11 Alaerts, L. *et al.* Probing the lewis acidity and catalytic activity of the metal-organic framework [Cu<sub>3</sub>(btc)<sub>2</sub>] (BTC=Benzen-1,3,5-tricarboxylate). *Chem. Eur. J.* **12**, 7353-7363 (2006).
- 12 Horcajada, P. *et al.* Synthesis and catalytic properties of MIL-100(Fe), an iron(III) carboxylate with large pores. *Chem. Commun.*, 2820-2822 (2007).
- 13 Forster, P. M. *et al.* Hydrogen adsorption in nanoporous nickel (II) phosphates. *J. Am. Chem. Soc.* **125**, 1309-1312 (2003).
- 14 Vitillo, J. G. *et al.* Role of exposed metal sites in hydrogen storage in MOFs. *J. Am. Chem. Soc.* **130**, 8386-8396 (2008).

- 15 Mu, B., Li, F. & Walton, K. S. A novel metal-organic coordination polymer for selective adsorption of CO<sub>2</sub> over CH<sub>4</sub>. *Chem. Commun.*, 2493-2495 (2009).
- 16 Cmarik, G. E., Kim, M., Cohen, S. M. & Walton, K. S. Tuning the adsorption properties of UiO-66 via ligand functionalization. *Langmuir* **28**, 15606-15613 (2012).
- 17 Kandiah, M. *et al.* Synthesis and stability of tagged UiO-66 Zr-MOFs. *Chem. Mater.* **22**, 6632-6640 (2010).
- 18 Huang, Y., Qin, W., Li, Z. & Li, Y. Enhanced stability and CO<sub>2</sub> affinity of a UiO-66 type metal-organic framework decorated with dimethyl groups. *Dalton Trans.* **41**, 9283-9285 (2012).
- 19 Yang, Q. *et al.* Functionalizing porous zirconium terephthalate UiO-66(Zr) for natural gas upgrading: a computational exploration. *Chem. Commun.* **47**, 9603-9605 (2011).
- 20 Wang, Z. & Cohen, S. M. Postsynthetic modification of metal-organic frameworks. *Chem. Soc. Rev.* **38**, 1315-1329 (2009).
- 21 Farrusseng, D. *et al.* Heats of adsorption for seven gases in three metal-organic frameworks: systematic comparison of experiment and simulation. *Langmuir* **5**, 7383-7388 (2009).
- 22 Jasuja, H., Huang, Y.-g. & Walton, K. S. Adjusting the stability of metal-organic frameworks under humid conditions by ligand functionalization. *Langmuir* **28**, 16874-16880 (2012).
- 23 Wang, Z., Tanabe, K. K. & Cohen, S. M. Tuning hydrogen sorption properties of metal-organic frameworks by postsynthetic covalent modification. *Chem. Eur. J.* **16**, 212-217 (2010).
- 24 Zhao, Y. *et al.* Enhancing gas adsorption and separation capacity through ligand functionalization of microporous metal-organic framework structures. *Chem. Eur. J.* **17**, 5101-5109 (2011).
- 25 Dau, P. V., Tanabe, K. K. & Cohen, S. M. Functional group effects on metal-organic framework topology. *Chem. Commun.* **48**, 9370-9372 (2012).
- 26 Brunauer, S., Emmett, P. H. & Teller, E. Adsorption of gases in multimolecular layers. *J. Am. Chem. Soc.* **60**, 309-319 (1938).
- 27 Walton, K. S. & Snurr, R. Q. Applicability of the BET method for determining surface areas of microporous metal-organic frameworks. *J. Am. Chem. Soc.* **129**, 8552-8556 (2007).

- 28 Karra, J. R. & Walton, K. S. Effect of open metal sites on adsorption of polar and nonpolar molecules in metal-organic framework Cu-BTC. *Langmuir* **24**, 8620-8626 (2008).
- 29 Mohr, R. & Rao, M. B. Isosteric heat of adsorption: theory and experiment. *J. Phys. Chem. B* **103**, 6539-6546 (1999).
- 30 Do Duong, D. *Adsorption analysis: equilibria and kinetics*. Vol. 2 (Imperial College Pr, 1998).
- 31 Cavenati, S., Grande, C. A., Rodrigues, A. r. E., Kiener, C. & Müller, U. Metal organic framework adsorbent for biogas upgrading. *Ind. Eng. Chem. Res.* **47**, 6333-6335 (2008).
- 32 Moellmer, J., Moeller, A., Dreisbach, F., Glaeser, R. & Staudt, R. High pressure adsorption of hydrogen, nitrogen, carbon dioxide and methane on the metal-organic framework HKUST-1. *Microporous Mesoporous Mater.* **138**, 140-148 (2011).
- 33 Van Heest, T., Teich-McGoldrick, S. L., Greathouse, J. A., Allendorf, M. D. & Sholl, D. S. Identification of metal-organic framework materials for adsorption separation of rare gases: applicability of ideal adsorbed solution theory (IAST) and effects of inaccessible framework regions. *J. Phys. Chem. C* **116**, 13183-13195 (2012).
- 34 Chen, Z. *et al.* Significantly enhanced CO<sub>2</sub>/CH<sub>4</sub> separation selectivity within a 3D prototype metal-organic framework functionalized with OH groups on pore surfaces at room temperature. *Eur. J. Inorg. Chem.* **2011**, 2227-2231 (2011).
- 35 Babarao, R., Hu, Z., Jiang, J., Chempath, S. & Sandler, S. I. Storage and separation of CO<sub>2</sub> and CH<sub>4</sub> in silicalite, C168 schwarzite, and IRMOF-1: A comparative study from Monte Carlo simulation. *Langmuir* **23**, 659-666 (2007).
- 36 Challa, S. R., Sholl, D. S. & Johnson, J. K. Adsorption and separation of hydrogen isotopes in carbon nanotubes: Multicomponent grand canonical Monte Carlo simulations. *J. Chem. Phys.* **116**, 814-824 (2002).
- 37 Goj, A., Sholl, D. S., Akten, E. D. & Kohen, D. Atomistic simulations of CO<sub>2</sub> and N<sub>2</sub> adsorption in silica zeolites: the impact of pore size and shape. *J. Phys. Chem. B* **106**, 8367-8375 (2002).
- 38 Yang, Q. & Zhong, C. Molecular simulation of carbon dioxide/methane/hydrogen mixture adsorption in metal-organic frameworks. *J. Phys. Chem. B* **110**, 17776-17783 (2006).
- 39 Goetz, V., Pupier, O. & Guillot, A. Carbon dioxide-methane mixture adsorption on activated carbon. *Adsorption* **12**, 55-63 (2006).

- 40 Murthi, M. & Snurr, R. Q. Effects of molecular siting and adsorbent heterogeneity on the ideality of adsorption equilibria. *Langmuir* **20**, 2489-2497 (2004).

## CHAPTER 6

# ADJUSTING HYDROTHERMAL STABILITY VIA FUNCTIONALIZATION OF BTC PRECURSORS

### 6.1 Introduction

In this chapter, we focus on the hydrothermal stability of the new **fmj** and **tbo** materials. Hydrothermal stability is a critical issue for MOF applications, because humidity is present in many gas adsorption and separation systems. The low hydrothermal stability limits the usage of most MOF materials. However, relatively few studies have focused on hydrothermal stability of MOFs, and in general, we know very little about how the construction of MOFs affects their hydrothermal stability. Based on previous water studies, it is well known that some MOFs are water sensitive.<sup>1-5</sup> MOF structures containing the zinc-carboxylate connectivity, such as MOF-5 and MOF-177, were found to be unstable after exposure to liquid water.<sup>6</sup> However, the nitrogen-coordinated MOFs, such as ZIF-8, are stable under humid condition due to the higher basicity of these ligands compared to multidentate carboxylic acid.<sup>7-9</sup> MOFs consisting of metal ions such as zirconium (IV) provide high stability under high temperature and humidity environment.<sup>10-13</sup> UiO-66 shows no change in pXRD patterns after exposure to liquid water and other solvents. After adding the functional groups to the parent UiO-66 material, the functionalized MOFs maintained the same hydrothermal stability as the parent material. Recently, some studies have shown that the steric effect of some functional groups can change the hydrothermal stability of MOF materials dramatically.<sup>14</sup> Using hydrophobic functional groups, such as alkyl chains, can protect the oxygen-metal coordination sites from hydrolysis. However, the mechanism of hydrothermal stability of

MOFs is still unclear. In order to develop more hydrothermally stable MOFs, more effort should be put into this field to understand the degradation mechanisms of MOFs in humid environments. So far, no work has been done on how the topology changes affect hydrothermal properties of MOFs, especially with same connectivity. Herein, the formation of the two series CuBTC MOFs provides a convenient system for examining in a systematic way the topology effect and the impact of functional groups on the stability of MOFs.

So far, there have been several studies that focus on the hydrothermal stability HKUST-1, which showed good structure retention after exposure to liquid water.<sup>6</sup> MOFs with open metal sites, such as HKUST-1 are quite hydrophilic and appear to maintain the structure according to pXRD, but significant surface area loss indicates the decomposition is occurring.<sup>15</sup> In this work, we report the water vapor adsorption properties and crystallinity changes before and after water adsorption measurement of the two series of functionalized CuBTC MOFs, tbo-bromo, tbo-acetamide, fmj-methyl, fmj-ethyl, and fmj-methoxy, to understand how the topology affects the hydrothermal stability and how the functional groups affect the water adsorption properties.

## **6.2 Experimental Details**

### **5.2.1 Materials Synthesis and Activation**

All chemicals were commercially available and used as received without further purification. The functionalized ligands and two series of CuBTC MOFs were synthesized following procedures detailed in Chapter 4. Activation procedure of all materials can be found in Chapter 4 as well.

## 5.2.2 Experimental Methods and Procedures

Water vapor adsorption isotherms were collected using an IGA-003 from Hiden Isochema, which was designed to study vapor sorption processes. Dry air was used as the carrier gas, with a portion of the carrier gas being bubbled through a vessel of deionized water. This system incorporates a multiple inlet mass flow control system which can control the ratio of saturated air and dry air. Dry air used in the water adsorption experiments was Ultra-High Purity (Airgas). More experimental details were listed in chapter 3.

## 6.3 Results and Discussion

### 6.3.1 Water Adsorption Measurements

In this work, we measured the water vapor adsorption of derivatives of HKUST-1 MOF, tbo-acetamide, tbo-bromo, fmj-methyl, and fmj-ethyl, and fmj-methoxy. Results are shown in Figure 6.1. As expected, all derivatives of HKUST-1 with different functional groups exhibit a strong affinity for water molecules. This result is consistent with previous reports that MOFs with open-metal sites have high affinities with water molecules. The tbo-acetamide and tbo-bromo CuBTC MOFs have similar adsorption loadings under low humidity with HKUST-1, due to the presence of open metal sites and the similarity of the structure. At high humidity, the MOFs with acetamide and bromo functional groups (20 and 23 mol/kg for tbo-acetamide and tbo-bromo respectively) have lower water loading than HKUST-1 (33 mol/kg). This result may be attributed to the size of the functional groups acetamide and bromo, which may partially block the access of water in the functionalized materials compared to parent material HKUST-1. The fmj-

methoxy has similar uptake with fmj-methyl and fmj-ethyl, because all fmj MOFs break down in a similar way during water exposure.

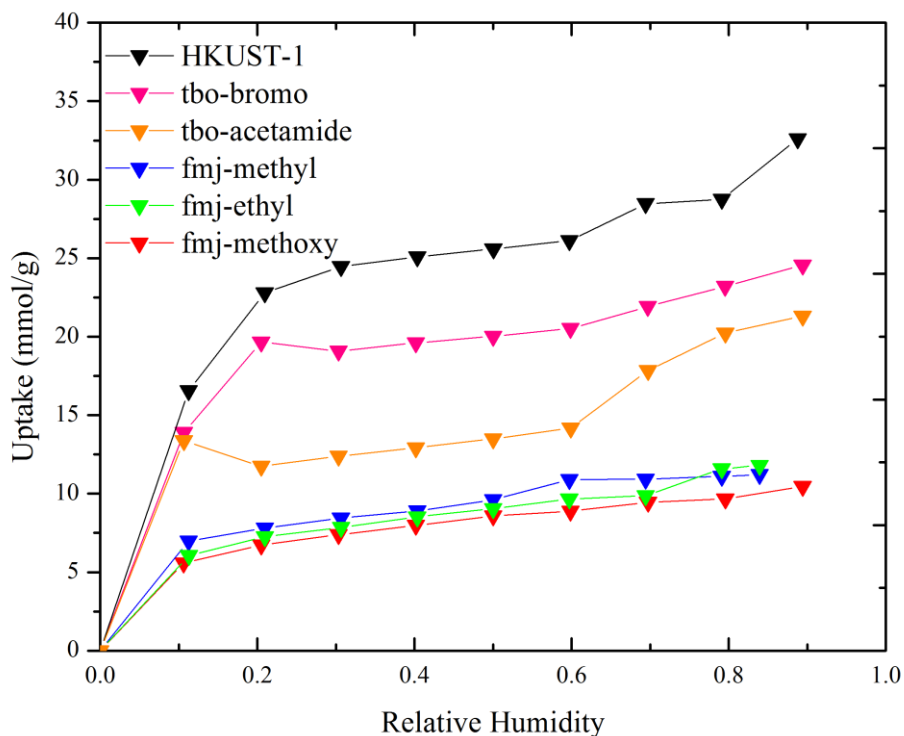


**Figure 6.1** Water adsorption isotherms for samples at 298 K

### 6.3.2 Structural Stability

There are still concerns about the chemical and mechanical stability of this class of materials. Therefore, each of the MOFs was examined for structural stability upon water exposure by comparing pXRD patterns and the BET surface area changes before and after the water adsorption measurements. Schoenecker et al showed that HKUST-1 is relatively stable under humidity; the pXRD patterns remains the same after water exposure, but the reactivated samples have a slightly decreased BET surface area.<sup>15</sup> As

shown in Figure 6.2-6.7, the **fmj** series samples present dramatic changes in pXRD data after water exposure, while pXRD patterns of the **tbo** series (tbo-bromo and tbo-acetamide) are still the same after water exposure. The crystalline structure of **tbo** series of MOFs remain intact, compared to the **fmj** series of MOFs. This result is consistent with the BET surface area study shown in Table 6.1; tbo-bromo and tbo-acetamide MOFs maintain 94-96% of BET surface area after the reactivation of water-exposed MOFs, while the **fmj** series of MOFs lose most of the BET surface area after reactivation. The BET surface areas of tbo-acetamide and tbo-bromo remain almost the same after water exposure, compared with HKUST-1 (26% BET surface area loss), so the functional groups partially protect the MOF structure. The pXRD and BET surface area tests both indicate that tbo topology is more stable than fmj topology. Considering how individual ligands differ in the **tbo** and **fmj** topologies (Chapter 4), unlike the **tbo** topology, the presence of functional groups in the **fmj** topology pushes away two ortho-carboxylate groups and causes them to be twisted out of the plane. The ortho-carboxylate groups lose their protection from benzene rings and are exposed to water molecules under humid conditions. In the **fmj** topology, the water molecules can easily access to the oxygen in the carboxylate groups and break the bond between the Cu ions and the oxygen in carboxylate groups. This result is consistent with the discovery that nonpolar functional groups provided the shielding effect on the MOF structure.<sup>14</sup> This work shows that the topology change from **tbo** to **fmj** results in the carboxylate groups in the **fmj** topology losing their shield, and the bond between the Cu ions and oxygen in carboxylate groups can be easily attacked under humid conditions. The hydrothermal stability depends on not only the connectivity of the MOFs but also the way MOFs are constructed (or topology).

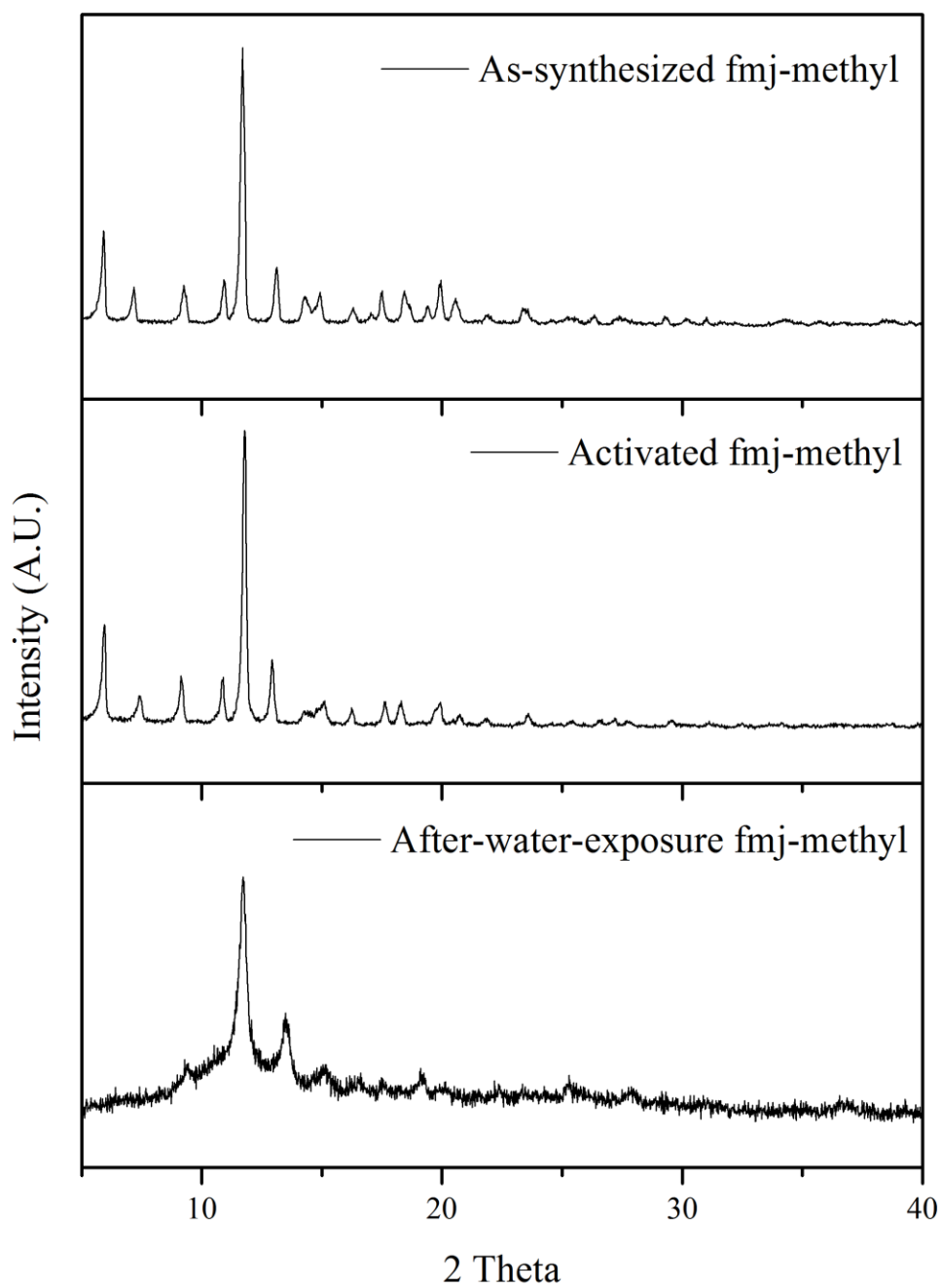


**Figure 6.2** pXRD Patterns for As-synthesized, Activated and After-exposure-to-water fmj-methyl Samples

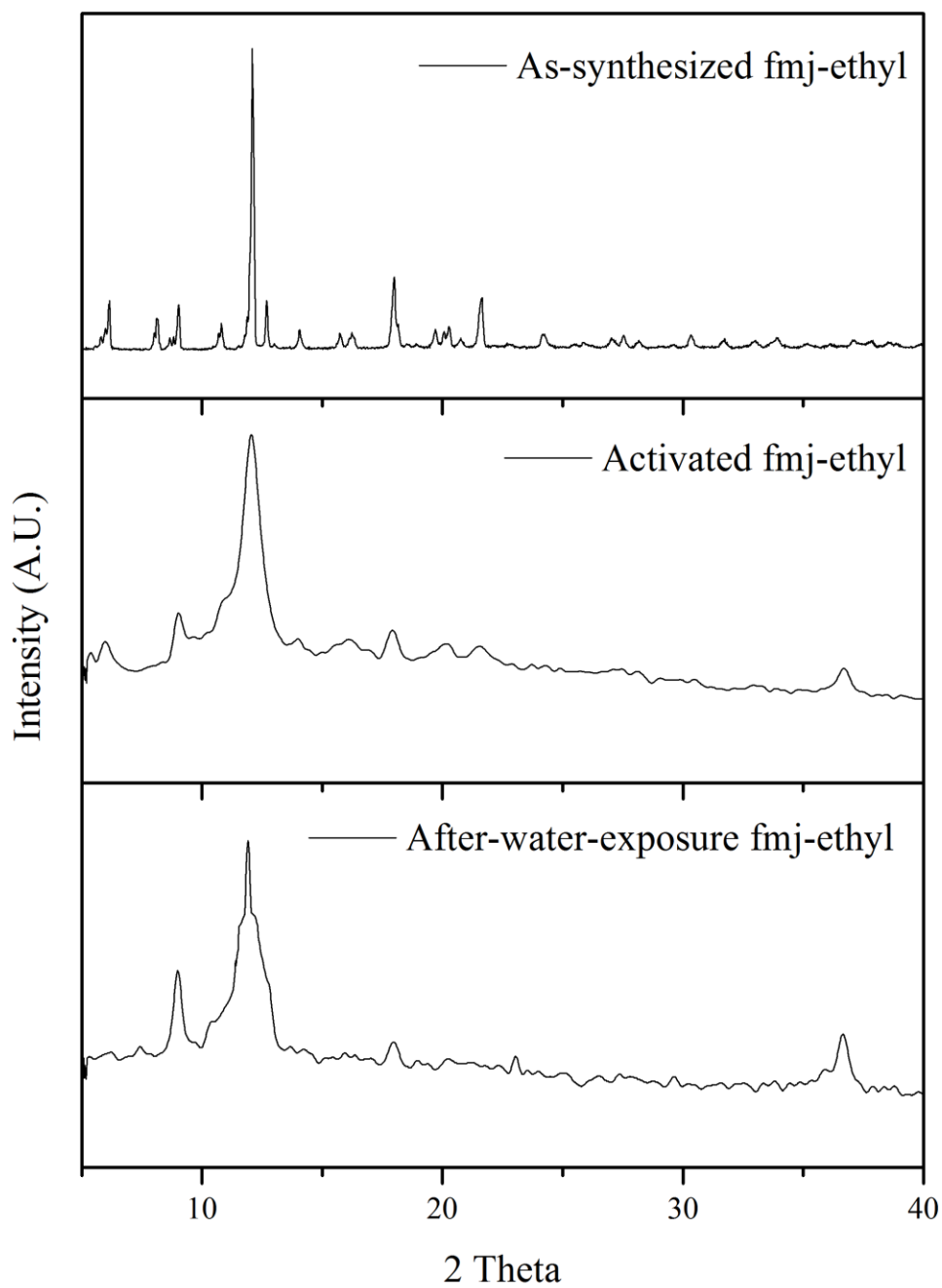


**Figure 6.3** pXRD Patterns for As-synthesized, Activated and After-exposure-to-water fmj-ethyl Samples

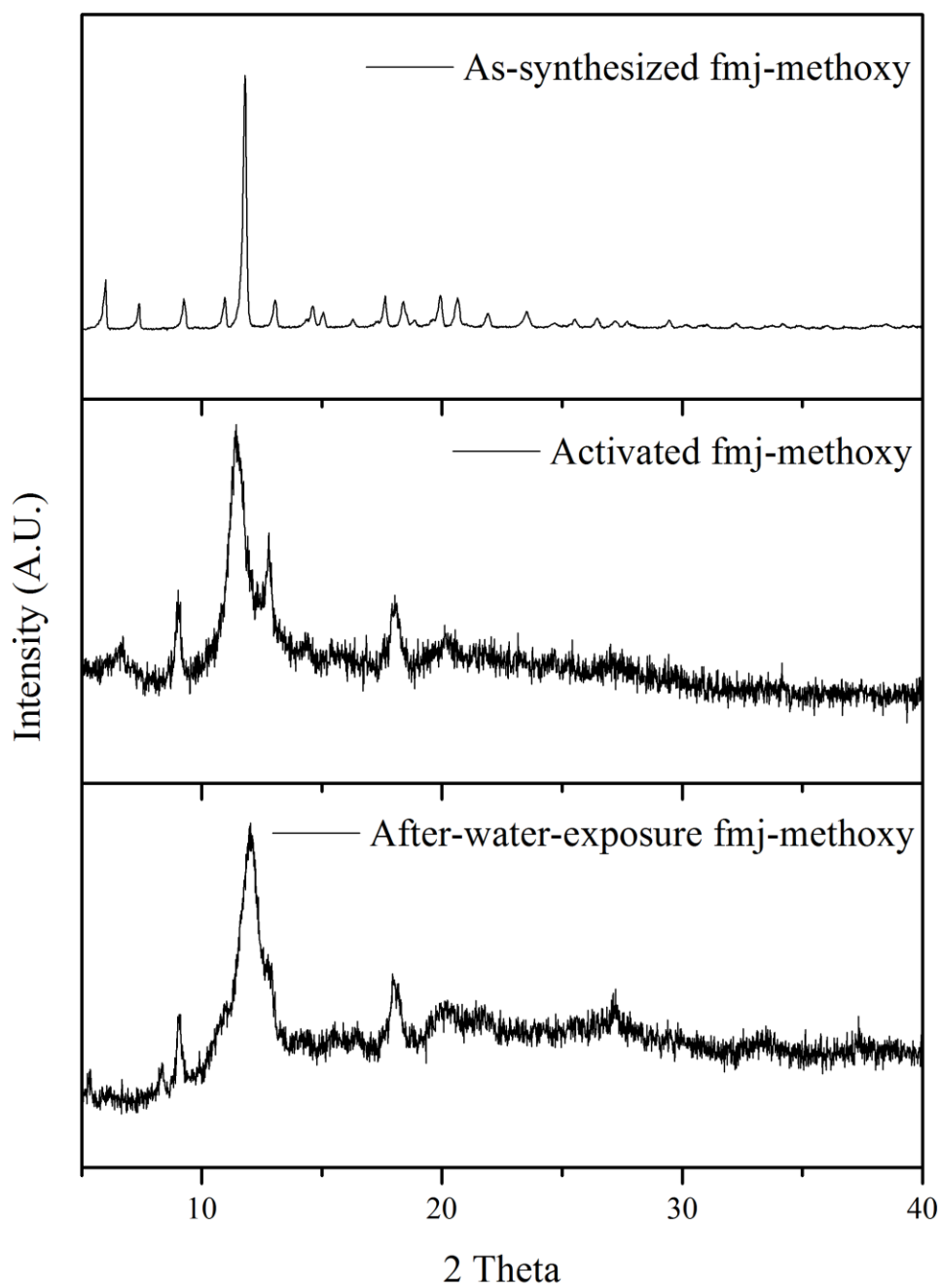


**Figure 6.4** pXRD Patterns for As-synthesized, Activated and After-exposure-to-water fmj-methoxy Samples

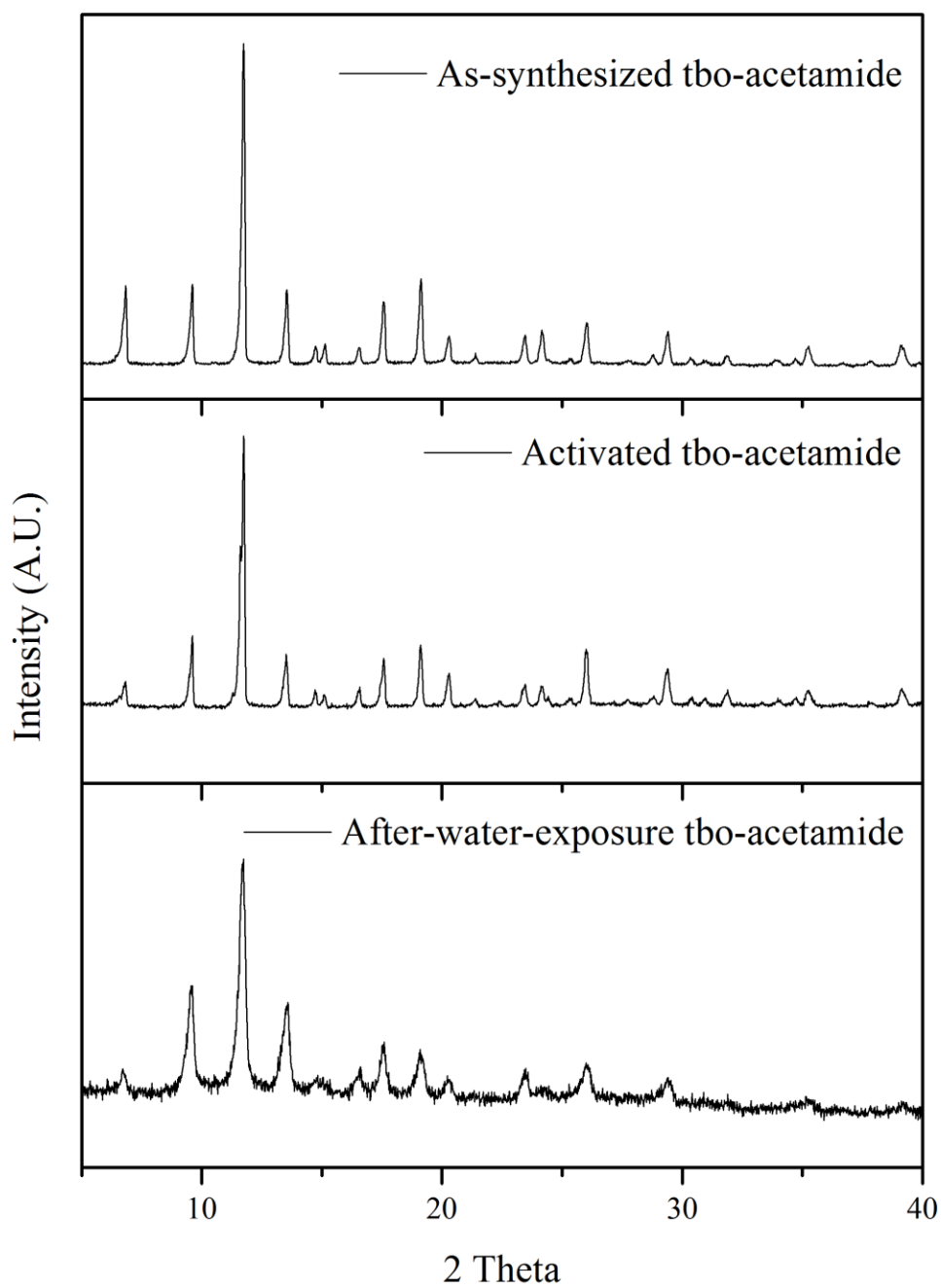


**Figure 6.5** pXRD Patterns for As-synthesized, Activated and After-exposure-to-water tbo-acetamide Samples

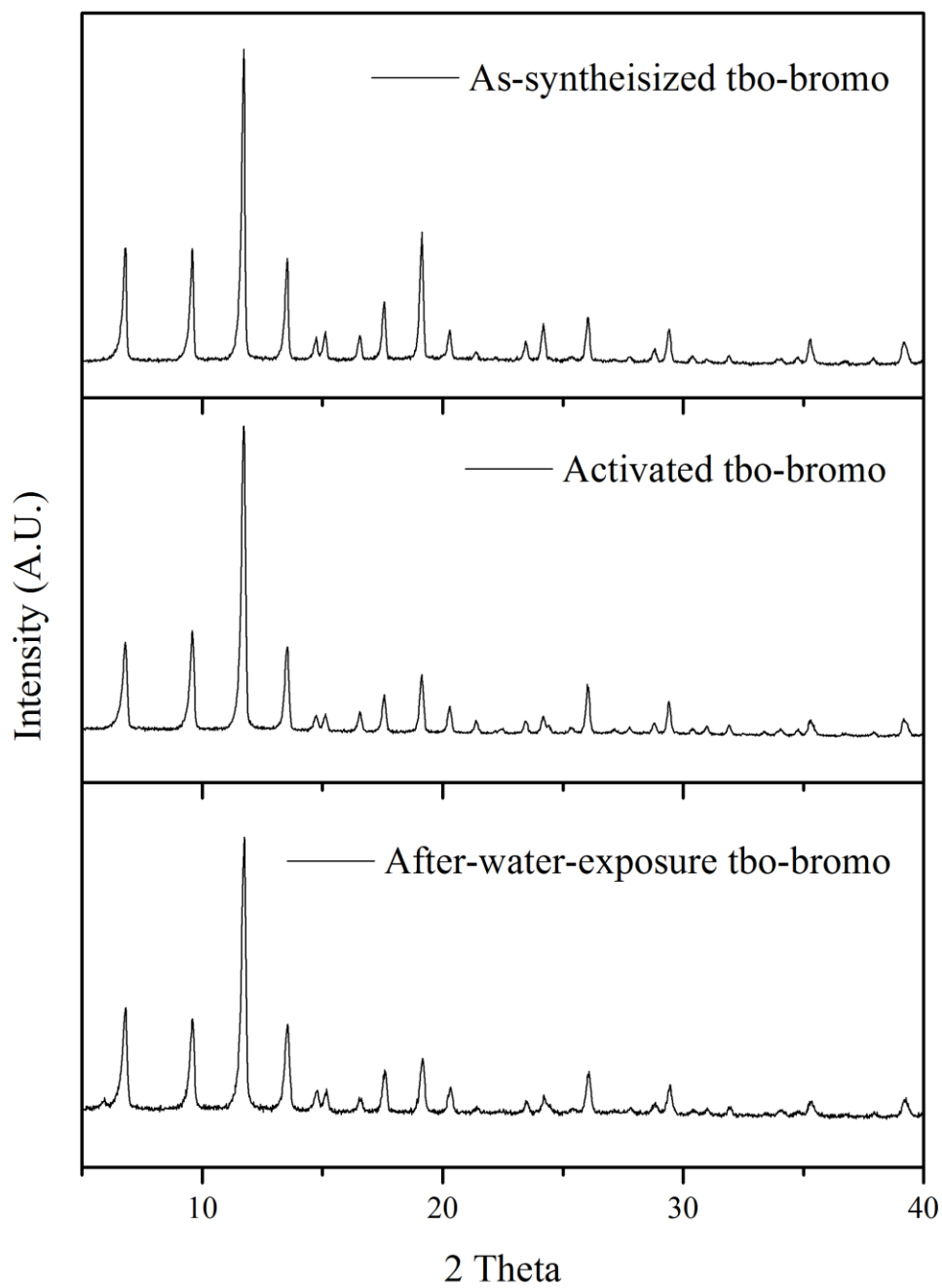


**Figure 6.6** pXRD Patterns for As-synthesized, Activated and After-exposure-to-water tbo-bromo Samples

**Table 6.1** Accessible and BET Surface Areas Comparison Before and After Water

materials	Accessible SA (m <sup>2</sup> /g)	Exposure		
		before	after	Loss %
HKUST-1	2224	1509,1270 <sup>15</sup>	945 <sup>15</sup>	26 <sup>15</sup>
tbo-bromo	1929	1458	1358	6.8
tbo-acetamide	1680	1415	1368	3.3
fmj-methoxy	1824	1295	45	96.5
fmj-methyl	1921	1471	74	95
fmj-ethyl	1563	1434	60	95.8

#### 6.4 Conclusions

All derivatives of HKUST-1 with different functional groups exhibit a strong affinity for water molecules due to the presence of open metal sites. The tbo-acetamide and tbo-bromo CuBTC MOFs have similar adsorption loadings under low humidity with HKUST-1, due to the presence of open metal sites and the similarity of the structure. At high humidity, the lower water loadings of tbo-acetamide and tbo-bromo may be attributed to the size of the functional groups acetamide and bromo, which may partially block the access of water to the functionalized materials, compared to parent material HKUST-1. The fmj-methoxy has similar uptake to fmj-methyl and fmj-ethyl, because all **fmj** MOFs break down in a similar way during water exposure. Considering the water vapor adsorption measurement and pXRD studies together, we noticed that the different topologies lead to entirely different hydrothermal stability, even with same connectivity.

The **tbo** topology (HKUST-1, tbo-bromo, tbo-acetamide) yields more stable structure than the **fmj** topology (fmj-methyl, fmj-ethyl, and fmj-methoxy). The **fmj** series of MOFs completely lost the surface areas and their crystallinity after water exposure completely. The presence of functional groups in the fmj topology pushes away two ortho-carboxylate groups and causes them to be twisted out of the plane, which results in the exposure of the bond between the Cu ions and oxygen in carboxylate groups to water molecules. The **tbo** series of MOFs retained their crystallinity based on pXRD, but it is important to note that slightly degradation of the structure may not show up in the pXRD patterns, which could decrease the BET surface areas of the reactivated samples. The functionalized HKUST-1 materials maintain the BET surface areas better than HKUST-1, due to the protection from their bulky functional groups.

## 6.5 References

- 1 Huang, L. *et al.* Synthesis, morphology control, and properties of porous metal–organic coordination polymers. *Microporous Mesoporous Mater.* **58**, 105-114 (2003).
- 2 Greathouse, J. A. & Allendorf, M. D. The interaction of water with MOF-5 simulated by molecular dynamics. *J. Am. Chem. Soc.* **128**, 10678-10679 (2006).
- 3 Kaye, S. S., Dailly, A., Yaghi, O. M. & Long, J. R. Impact of preparation and handling on the hydrogen storage properties of Zn<sub>4</sub>O(1, 4-benzenedicarboxylate)<sub>3</sub> (MOF-5). *J. Am. Chem. Soc.* **129**, 14176-14177 (2007).
- 4 Wu, T. *et al.* Enhancing the stability of metal–organic frameworks in humid air by incorporating water repellent functional groups. *Chem. Commun.* **46**, 6120-6122 (2010).
- 5 Hausdorf, S., Wagler, J. r., Moßig, R. & Mertens, F. O. Proton and water activity-controlled structure formation in zinc carboxylate-based metal organic frameworks. *J. Phys. Chem. A* **112**, 7567-7576 (2008).
- 6 Cychosz, K. A. & Matzger, A. J. Water stability of microporous coordination polymers and the adsorption of pharmaceuticals from water. *Langmuir* **26**, 17198-17202 (2010).
- 7 K üsgens, P. *et al.* Characterization of metal-organic frameworks by water adsorption. *Microporous Mesoporous Mater.* **120**, 325-330 (2009).
- 8 Choi, H. J., Dincă, M., Dailly, A. & Long, J. R. Hydrogen storage in water-stable metal–organic frameworks incorporating 1, 3-and 1, 4-benzenedipyrazolate. *Energy Environ. Sci.* **3**, 117-123 (2010).
- 9 Park, K. S. *et al.* Exceptional chemical and thermal stability of zeolitic imidazolate frameworks. *Proc. Natl. Acad. of Sci.* **103**, 10186-10191 (2006).
- 10 Kandiah, M. *et al.* Synthesis and stability of tagged UiO-66 Zr-MOFs. *Chem. Mater.* **22**, 6632-6640 (2010).
- 11 Huang, Y., Qin, W., Li, Z. & Li, Y. Enhanced stability and CO<sub>2</sub> affinity of a UiO-66 type metal-organic framework decorated with dimethyl groups. *Dalton Trans.* **41**, 9283-9285 (2012).
- 12 Yang, Q. *et al.* Functionalizing porous zirconium terephthalate UiO-66(Zr) for natural gas upgrading: a computational exploration. *Chem. Commun.* **47**, 9603-9605 (2011).

- 13 Cavka, J. H. *et al.* A new zirconium inorganic building brick forming metal organic frameworks with exceptional stability. *J. Am. Chem. Soc.* **130**, 13850-13851 (2008).
- 14 Jasuja, H., Huang, Y.-g. & Walton, K. S. Adjusting the stability of metal-organic frameworks under humid conditions by ligand functionalization. *Langmuir* **28**, 16874-16880 (2012).
- 15 Schoenecker, P. M., Carson, C. G., Jasuja, H., Flemming, C. J. J. & Walton, K. S. Effect of water adsorption on retention of structure and surface area of metal-organic frameworks. *Ind. Eng. Chem. Res.* **51**, 6513-6519 (2012).

## CHAPTER 7

# PURIFICATION OF MIXED-PHASE MATERIALS VIA SYNTHESIS CONDITION MODIFICATION

### 7.1 Introduction

The rational design and construction of metal-organic frameworks (MOFs) have received much attention, due to interest for potential applications in gas separations, heterogeneous catalysis, and gas storage.<sup>1-5</sup> There is also great scientific interest in the formation of molecular assemblies, topology and cluster, and in the physical properties of adsorbents.<sup>3</sup> The synthesis of MOFs proceeds mainly under solvothermal conditions, especially for synthesizing novel MOFs.<sup>6</sup>

The most detailed structural information can be gained from single crystal X-ray crystallography. Indeed, without knowing the crystal structure, it will be quite difficult to interpret any subsequently observed properties. Therefore, the discovery of new MOF synthesis in this area is strongly directed toward obtaining X-ray quality single crystals.<sup>7-10</sup> Single crystals of MOF materials are usually generated in one-pot solvothermal synthesis.<sup>8-11</sup> However, in some cases there are multiple phases of MOFs coexisting in one-pot synthesis, so the mixed materials need to be separated or purified. The purification methods, such as distillation, recrystallization, chromatography, sublimation, etc., are not feasible for the separation of mixed MOF materials. If sufficiently large crystals of distinct morphology or color are obtained, they can be manually separated, but it is usually time-consuming. Farha et al. introduced a physical method to isolate solids that takes advantage of MOF density differences such that one phase floats in a solvent of appropriate density while the other sinks.<sup>12</sup> However, this method requires significant

density differences between the different phases and also requires good stability of the MOFs in the solvent. Nevertheless, even if the MOF is stable in the solvent, the physical separation of mixed materials still wastes a large amount of starting materials.

## 7.2 Synthesis and Characterization of Multi-Phase Materials

In Chapter 4, we reported that there are multiple phases coexisting in the one-pot reaction used to synthesize fmj-methoxy.  $[\text{Cu}_3(\text{MeOBTC})(\text{HOBTC})(\text{H}_2\text{O})_3]$  (fmj-methoxy) and  $\text{Cu}(\text{HOBTC})$  MOFs both were synthesized in one-pot solvothermal synthesis from the reaction of methoxy-BTC with  $\text{Cu}(\text{NO}_3)_2 \cdot 3\text{H}_2\text{O}$  at  $80^\circ\text{C}$  (see Chapter 4 for synthesis procedure). The fmj-methoxy structure is a body-centered-orthorhombic crystal that possesses the three-dimensional framework shown in Figure 7.1. It shares the same topology with fmj-methyl and fmj-ethyl materials. All carboxylate groups in methoxy-BTC are completely deprotonated and coordinated with the copper ions. The single crystal X-ray crystallographic study shows there are two different functional groups, methoxy and hydroxyl, which coexist in the crystal materials of fmj-methoxy. This result indicates that methoxy functional group decomposed to hydroxyl during the MOF synthesis because only methoxy ligands were included in the precursors.  $\text{Cu}(\text{HOBTC})$  is a needle-shaped blue crystal, whose structure is shown in Figure 7.2. The carboxylate groups in  $\text{Cu}(\text{HOBTC})$  are partially deprotonated. Two carboxylate groups and one hydroxyl group of one ligand are deprotonated and coordinate to two copper ions, which connect the two organic ligands together and form one layer. As shown in Figure 7.2 (b), layers are stacked via the coordination between the copper ions and the oxygen atoms of the carboxylate groups to form 1D MOF materials. In Figure 7.6 (a), NMR test on as-synthesized materials also confirms that most of the methoxy functional

groups in mixed materials have decomposed into hydroxyl functional groups. The experimental powder X-ray diffraction (pXRD) patterns of the bulk sample of materials did not match either of the simulated patterns, as shown in Figure 7.3. The multi-phase presence is also confirmed by SEM of the bulk phase sample, as shown in Figure 7.7 (a). New MOF structures are published frequently, but systematic investigations of the synthetic procedures and their parameters are rarely reported<sup>13</sup> and even fewer papers discuss how to separate the mixed-phase materials via systematically modifying the synthesis conditions. The coexistence of multi-phase materials in one-pot synthesis containing in situ ligands reaction, offers a rare opportunity to examine the role of various reaction variables in determining which structure forms and how the functional groups react during the MOF synthesis. Here, I conduct a systematic modification of the two variables of solvothermal synthesis conditions to purify the mixed MOF materials: pH value and temperature.

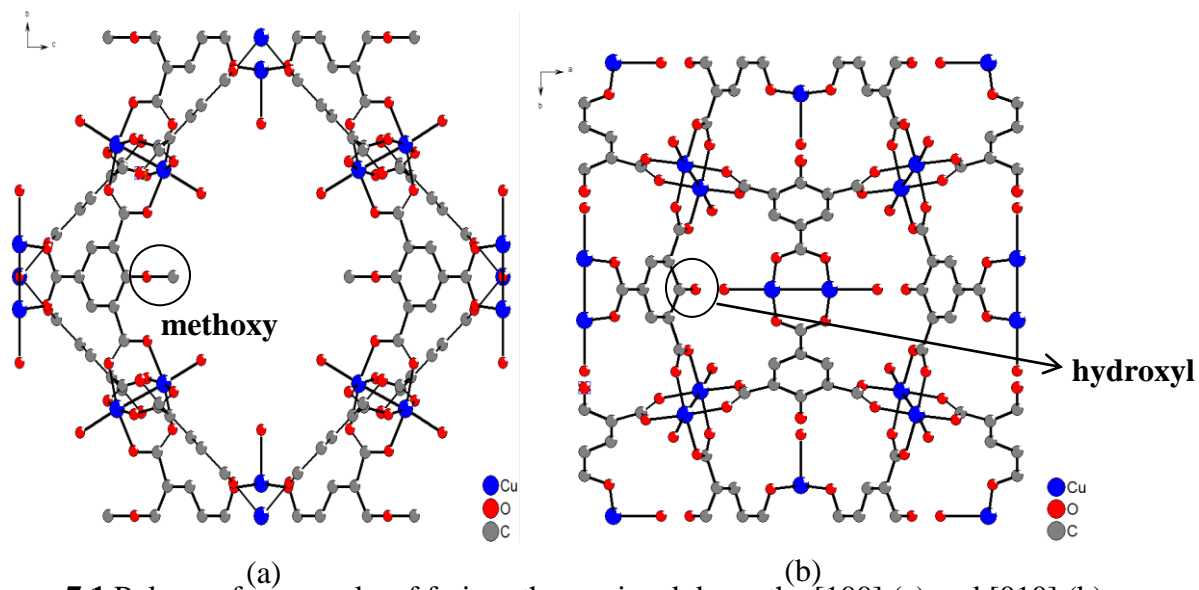


**Figure 7.1** Polymer frameworks of fmj-methoxy viewed down the [100] (a) and [010] (b) direction

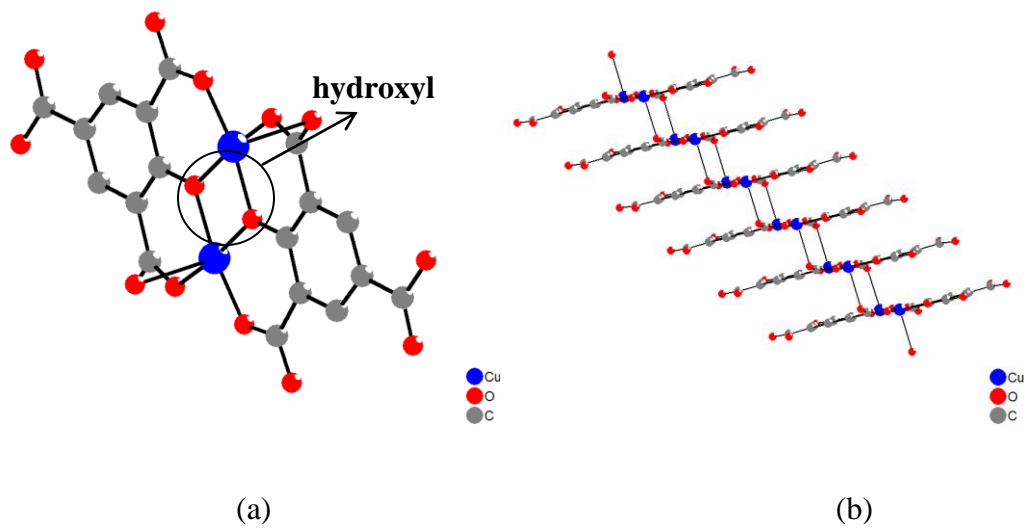


**Figure 7.2** (a) Cu(HOBTC) structure unit; (b) View of layers stacked in an ABAB manner of Cu(HOBTC)

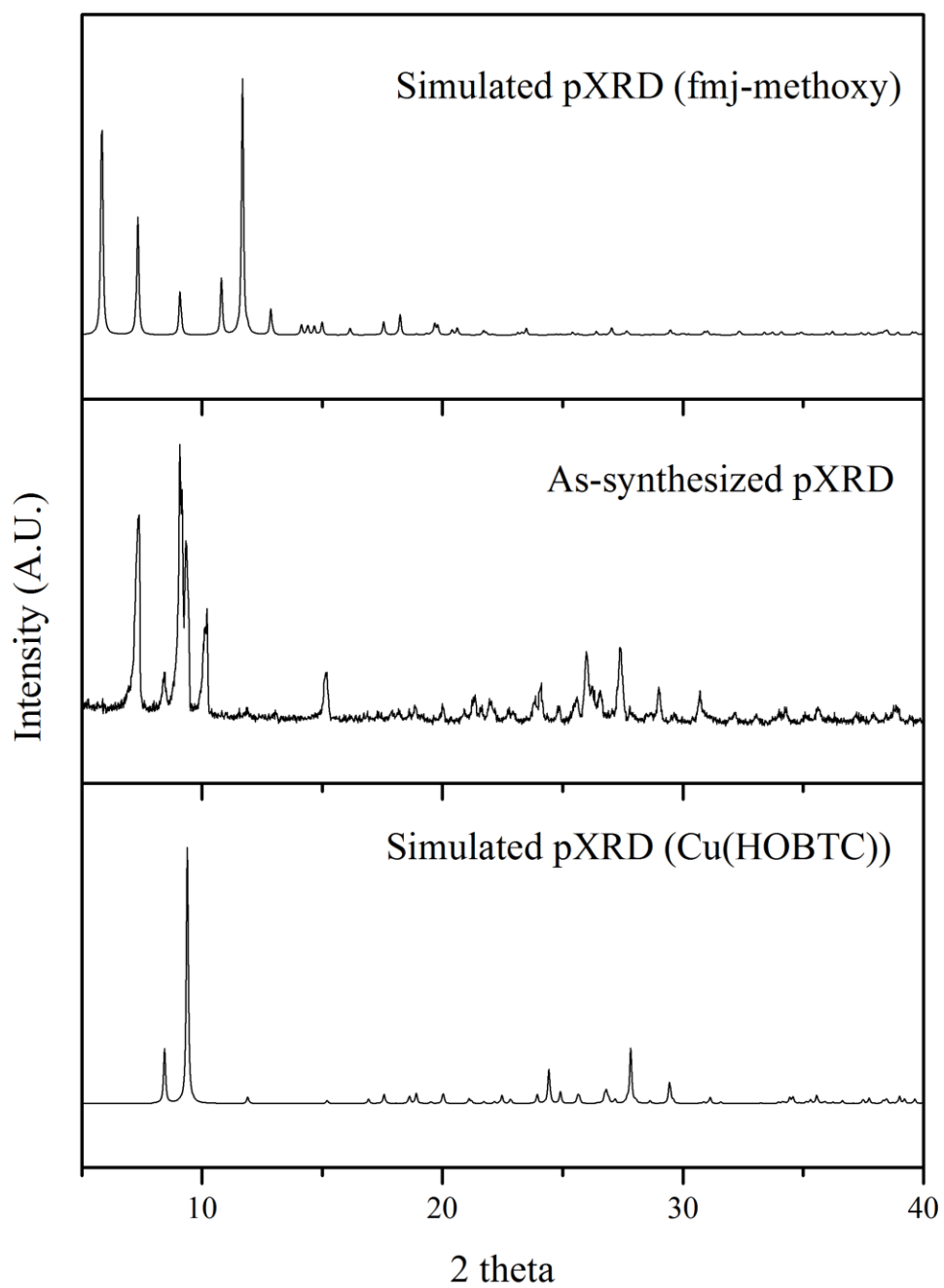


**Figure 7.3** Comparison between simulated pXRD of fmj-methoxy and Cu(HOBTC), and as-synthesized pXRD

### **7.3 Optimization of MOF Synthesis Condition**

All reagents were of analytical grade and used as received. The reaction mixture is placed in 20 mL glass vials, and the sealed vials are placed in a conventional oven for 3 days. After cooling to room temperature, the products are collected by using filter paper and allowed to air-dry overnight in the fume hood. The resulting products are characterized via pXRD and NMR to verify the structure of materials and phase purity. The crystal morphology is examined using scanning electron microscope (SEM). The nitrogen adsorption isotherms are measured at 77K, after evacuation of the obtained samples at 170<sup>o</sup>C for 8h. The surface areas were obtained using Brunauer, Emmett, Teller (BET) equation.

#### **7.3.1 Influence of pH Value on fmj-methoxy Synthesis**

The methoxy-BTC ligands in these two phases have different degrees of deprotonation: carboxylic groups of methoxy-BTC in fmj-methoxy crystal are completely deprotonated, while the ligands in Cu(HOBTC) are partially deprotonated. For multidentate carboxylate linkers, its degree of deprotonation would have great influence on the structures of the resulting coordination materials.<sup>14</sup> The previous studies showed that the high pH condition can increase the deprotonation of the carboxylate groups.<sup>15</sup> I postulated that pure fmj-methoxy material would be achieved under higher pH value conditions, so the influence of the pH value on the formation of mixed-phase materials was investigated. In the reaction mixture described in the original synthesis condition, the amount of 1M HCl aqueous solution was decreased from 0.25ml to 0.15ml and 0.05ml respectively. The mixtures were heated at 80<sup>o</sup>C for 3days. These reactions were all repeated for reproducibility tests. The pXRD patterns of the reaction products obtained

from synthesis mixtures with different amounts of HCl aqueous solution are shown in Figure 7.4. The intensity of the reflections belonging to Cu(HOBTC) decrease with the decrease of the amount of HCl aqueous solution. The elimination of this undesired phase Cu(HOBTC) was achieved under the condition with 0.05ml HCl aqueous solution. The peaks which represent the fmj-methoxy began to grow as the amount of HCl in the aqueous solution decreases. A possible explanation is that the increase of the pH can result in the complete deprotonation of carboxylate groups and the formation of fmj-methoxy. However, another unknown phase still can be observed in the bulk phase in addition to the formation of fmj-methoxy, based on the extra peak in the pXRD patterns.

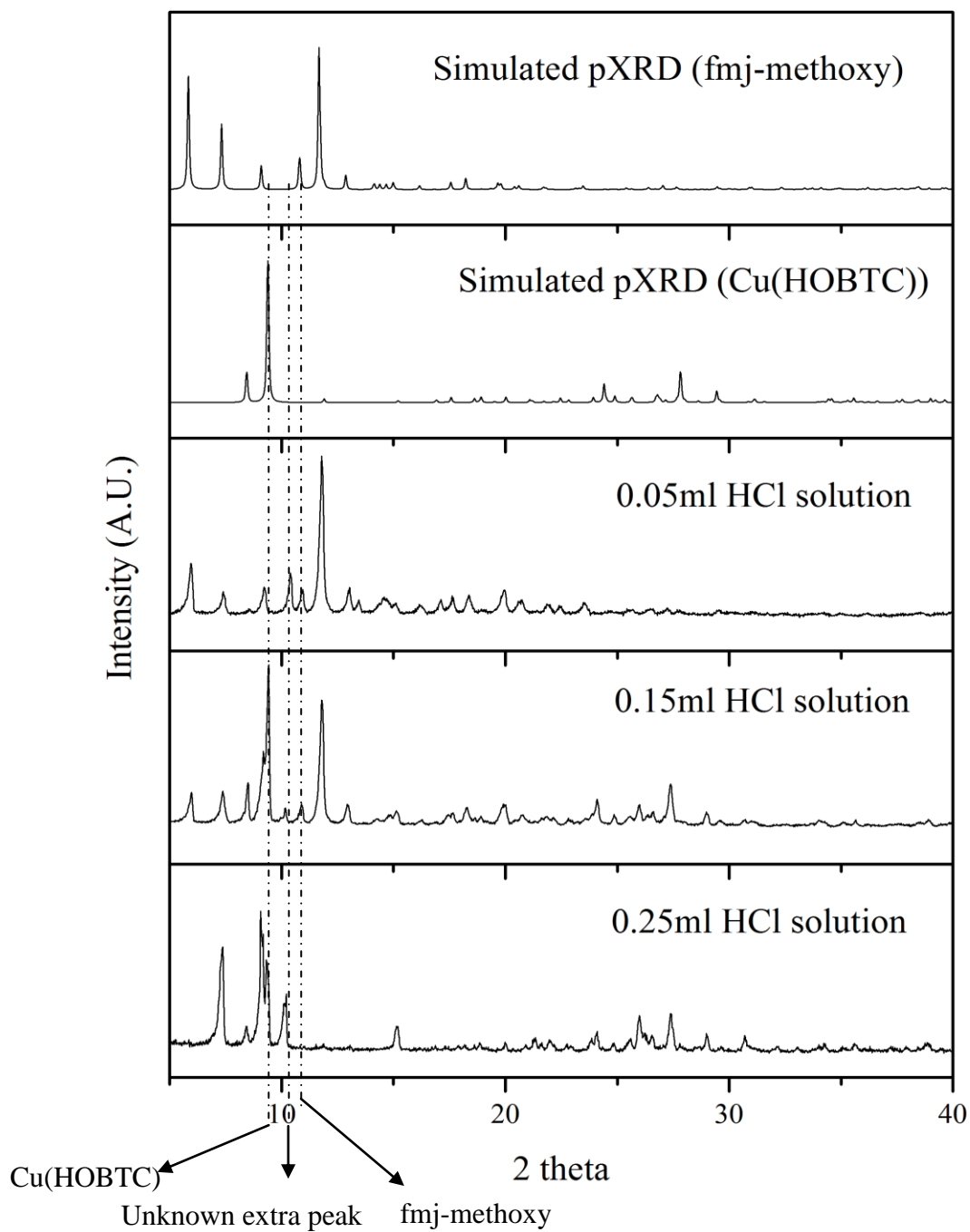


**Figure 7.4** Comparison among simulated pXRD from the fmj-methoxy and Cu(HOBTC) and as-synthesized pXRD of samples made with the different amount of 0.05 ml, 0.15 ml, and 0.25 ml 1M HCl aqueous solution at 80°C for 72h

### 7.3.2 Influence of Temperature on fmj-methoxy Synthesis

The role of temperature is also important for synthesis of MOF materials. For example, seven different cobalt succinates solids were obtained under the same starting mixture and only via changing temperature.<sup>16</sup> Therefore we studied the influence of the synthesis temperature on the phase purity. Keeping the same starting mixture of the synthesis condition with 0.05ml 1M HCl aqueous solution, the solvothermal syntheses were performed in the 20ml glass vials at 70<sup>0</sup>C, 80<sup>0</sup>C, and 90<sup>0</sup>C respectively. The reaction product was filtered off, rinsed with DMF solvent, and air-dried overnight. The diffraction patterns of the reaction products obtained from synthesis mixtures in conventional reactors at different temperature (70, 80, and 90<sup>0</sup>C) are shown in Figure 7.5. The unknown peaks disappeared at 90<sup>0</sup>C, but the amount of the Cu(HOBTC) impurity appeared again, as confirmed by the pXRD characterization in Figure 7.5. The formation of Cu(HOBTC) material is preferred at higher temperature. The pXRD patterns of as-synthesized materials at 70<sup>0</sup>C have a good consistency with simulated patterns of desired materials, so the pure materials can be obtained by using lower reaction temperature 70 °C with elimination of two undesired phases.

The functionality of materials was verified by NMR experiments with the results shown in Figure 7.6. As shown in the figure, only methoxy functional groups are present in the bulk-phase materials obtained from the reaction at 70 °C, while the methoxy functional groups were mostly decomposed under original synthesis conditions. In Figure 7.7, the comparison of SEM micrographs of original as-synthesized materials and the modified materials also confirmed that the pure desired materials can be obtained by the modification of the synthesis condition. We also measured N<sub>2</sub> adsorption isotherms on all

resulting materials at 77K and obtained the BET surface areas listed in Table 7.1. As we expected, the pure materials of fmj-methoxy give the highest surface area, which is close to the calculated accessible surface areas shown in Chapter 4.

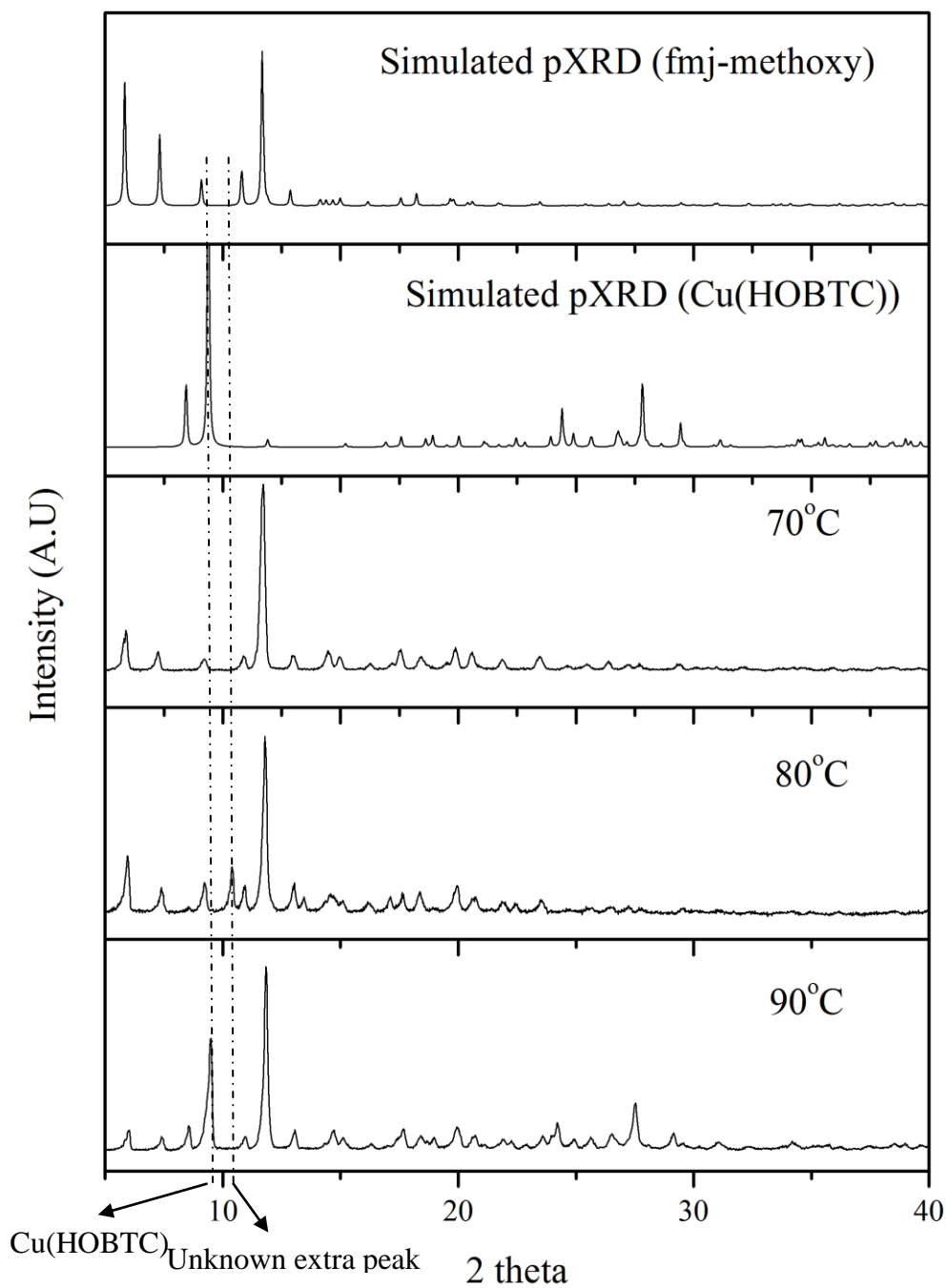


**Figure 7.5** Comparison among simulated pXRD from the fmj-methoxy and Cu(HOBTC) and as-synthesized pXRD of resultant products at 70°C, 80°C, and 90°C

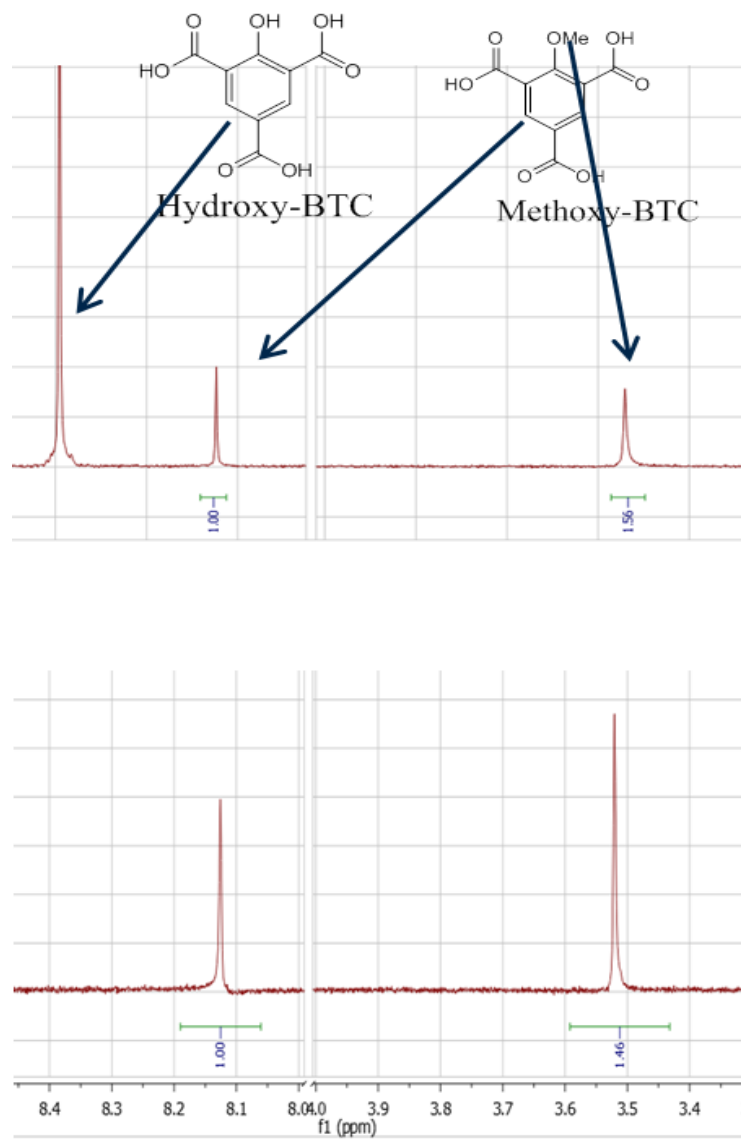


**Figure 7.6** NMR on as-synthesized samples before (a) and after (b) modification

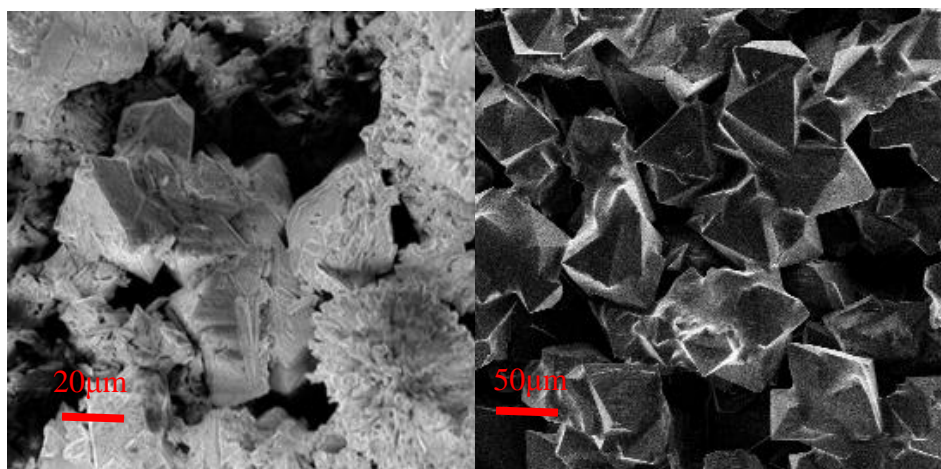


**Figure 7.7** SEM micrographs of as-synthesized samples before (a) and after (b) modification

**Table 7.1** BET Surface Areas of Samples under Different Synthesis Conditions

Samples and synthesis condition	BET surface areas (m <sup>2</sup> /g)
80 °C, 0.25 ml HCl	153
80 °C, 0.15 ml HCl	612
80 °C, 0.05 ml HCl	478
90 °C, 0.05 ml HCl	743
70 °C, 0.05 ml HCl	1259

## 7.4 Conclusions

For the fmj-methoxy and Cu(HOBTC) mixed materials, the pH value and the choice of temperature have profound effects on the phase purity. The experimental results show that the formation, phase purity, functionality, and morphology of materials are extremely sensitive to the synthesis parameters explored in this study. Relatively high pH value and low temperature result in the pure desired fmj-methoxy MOF. Thus higher pH value and lower temperature are usually responsible for deprotonation of carboxylate groups and also can decrease the demethylation of methoxy groups. Finally, we have been able to further optimize the synthesis procedure for fmj-methoxy samples free of other phases, which can be used to obtain optimized surface areas and for further application.

## 7.5 References

- 1 Kuppler, R. J. *et al.* Potential applications of metal-organic frameworks. *Coord. Chem. Rev.* **253**, 3042-3066 (2009).
- 2 James, S. L. Metal-organic frameworks. *Chem. Soc. Rev.* **32**, 276-288 (2003).
- 3 Ferey, G. Hybrid porous solids: past, present, future. *Chem. Soc. Rev.* **37**, 191-214 (2008).
- 4 Kitagawa, S., Kitaura, R. & Noro, S. Functional porous coordination polymers. *Angew. Chem. Int. Ed.* **43**, 2334-2375 (2004).
- 5 O'Keeffe, M. Design of MOFs and intellectual content in reticular chemistry: a personal view. *Chem. Soc. Rev.* **38**, 1215-1217 (2009).
- 6 Schlichte, K., Kratzke, T. & Kaskel, S. Improved synthesis, thermal stability and catalytic properties of the metal-organic framework compound  $\text{Cu}_3(\text{BTC})_2$ . *Microporous Mesoporous Mater.* **73**, 81-88 (2004).
- 7 Mu, B., Li, F. & Walton, K. S. A novel metal-organic coordination polymer for selective adsorption of  $\text{CO}_2$  over  $\text{CH}_4$ . *Chem. Commun.*, 2493-2495 (2009).
- 8 Cai, Y., Zhang, Y., Huang, Y., Marder, S. R. & Walton, K. S. Impact of alkyl-functionalized BTC on properties of copper-based metal-organic frameworks. *Cryst. Growth Des.* **12**, 3709-3713 (2012).
- 9 Huang, Y. G. *et al.* A porous flexible homochiral  $\text{SrSi}_2$  array of single-stranded helical nanotubes exhibiting single-crystal-to-single-crystal oxidation transformation. *Angew. Chem. Int. Ed.* **50**, 436-440 (2011).
- 10 Jasuja, H., Huang, Y.-g. & Walton, K. S. Adjusting the stability of metal-organic frameworks under humid conditions by ligand functionalization. *Langmuir* **28**, 16874-16880 (2012).
- 11 Schoenecker, P. M., Carson, C. G., Jasuja, H., Flemming, C. J. J. & Walton, K. S. Effect of water adsorption on retention of structure and surface area of metal-organic frameworks. *Ind. Eng. Chem. Res.* **51**, 6513-6519 (2012).
- 12 Farha, O. K., Mulfort, K. L., Thorsness, A. M. & Hupp, J. T. Separating solids: purification of metal-organic framework materials. *J. Am. Chem. Soc.* **130**, 8598-8599 (2008).
- 13 Forster, P. M., Stock, N. & Cheetham, A. K. A high-throughput investigation of the role of pH, temperature, concentration, and time on the synthesis of hybrid inorganic-organic materials. *Angew. Chem. Int. Ed.* **44**, 7608-7611 (2005).

- 14 Cheng, D., Khan, M. A. & Houser, R. P. Structural variability of cobalt (II) coordination polymers: three polymorphs of  $\text{Co}_3(\text{TMA})_2$  [TMA= Trimesate,  $\text{C}_6\text{H}_3(\text{COO})_3^{3-}$ ]. *Cryst. Growth Des.* **4**, 599-604 (2004).
- 15 Yaghi, O. M., Davis, C. E., Li, G. & Li, H. Selective guest binding by tailored channels in a 3-D porous zinc(II)-benzenetricarboxylate network. *J. Am. Chem. Soc.* **119**, 2861-2868 (1997).
- 16 Forster, P. M., Burbank, A. R., Livage, C., Ferey, G. & Cheetham, A. K. The role of temperature in the synthesis of hybrid inorganic-organic materials: the example of cobalt succinates. *Chem. Commun.*, 368-369 (2004).

## CHAPTER 8

### CONCLUSIONS AND RECOMMENDATIONS

One of the ongoing endeavors to effectively enhance the performance of MOF materials and access advanced MOF materials suitable for more specialized and sophisticated applications is to integrate functionalities of greater complexity into these materials.<sup>1-5</sup> However, despite numerous interesting results and findings, a great challenge remains in the systemic design of the isostructural MOFs with different functional groups because the groups may interfere with formation of the desired MOF to form other materials, and finding the appropriate reaction conditions for forming a particular MOF requires a great effort. Thus, this work focused on how functional groups affect the topology, the adsorption properties, and the hydrothermal stability of the materials, and how the parameters of the synthesis conditions affect the formation of desired materials.

#### 8.1 Synthesis of Isostructural MOFs with Functionalized Organic Ligands (Chapter 3 and Chapter 4)

In Chapter 3 and Chapter 4, I have shown that functionalized HKUST-1 derivatives adopt multiple crystal structures. This is a striking example where inclusion of new functional groups in a MOF does not lead to an isostructural family of materials, even though sterics would indicate that the isostructural materials are plausible. I synthesized tagged HKUST-1 with acetamide, nitro, and bromo functionalized BTC ligands based on the **tbo** topology, while forming another series of CuBTC frameworks under **fmj** topology with methyl-, ethyl-, and methoxy-BTC linkers. At first, I was expecting to get functionalized isostructural MOFs of HKUST-1 with all functionalized

BTC ligands, but even minor changes to the parent linker can lead to the formation of derivatives under different topology. These results showed the polarity of functional groups has an effect on the formation of the MOF structure: polar functional groups, such as amino, nitro, acetamide, bromo, maintain the **tbo** topology of HKUST-1; while nonpolar functional groups (methyl and ethyl groups) lead to the new CuBTC under **fmj** topology. The methoxy groups are polar functional groups, which lead to **fmj** topology as well. The only exception may be attributed to the interaction between functional groups and synthesis solvent during the MOF synthesis.

In this work, I have synthesized six derivatives of HKUST-1 with acetamide, nitro, bromo, methyl, ethyl, and methoxy functional groups. In the near future, studies should implement other interesting functionalized ligands, such as hydroxyl or carboxylic functional groups, which have high polarity and acidity. There are three sites in BTC ligands which could be functionalized. The incorporation of the multiple functional groups in BTC ligands has not been studied yet, such as trimethyl-BTC ligands. Thus, next steps should be focused on the synthesis of MOF materials with multiple functional groups attached in one BTC ligand.

The impact of functional groups on the structure of the MOFs strongly depends on the type of the ligands used. MOFs with functionalized di-dentate linkers always maintained the topology of their parent materials, such as UiO-66,<sup>5,6</sup> DMOF,<sup>1</sup> and MIL-53,<sup>7</sup> while the topology change by adding functional groups mostly happened on the tri-dentate linkers, such as BTB<sup>3</sup> and BTC ligands. For the long-term research, the effort should be made on other MOF systems with tri-dentate or other multi-dentate ligands such as MOF-14<sup>8</sup> or UMCM-1,<sup>9</sup> to understand how the functional groups affect the

formation of the MOF structure and improve the understanding of the construction of MOF materials.

## 8.2 Functional Groups Effect on Gas Adsorption Isotherms (Chapter 5)

The reticular synthesis method has been applied on several MOF systems, such as IRMOFs,<sup>10</sup> UIO-66,<sup>5,6,11</sup> and MIL-53<sup>12,13</sup> and some studies have been done on the effect of functional groups on the adsorption properties. In this work, I demonstrated that functional groups have the following effect on the adsorption properties: some polar functional groups enhance the adsorption of CO<sub>2</sub>, while bulky functional groups increase the affinity with methane molecules, which are consistent with their isosteric heat of adsorption values. The MOFs with polar functional groups have a higher CO<sub>2</sub>/CH<sub>4</sub> adsorption selectivity than HKUST-1, while nonpolar functional groups decrease CO<sub>2</sub>/CH<sub>4</sub> adsorption selectivity due to the increase of the interaction between the CH<sub>4</sub> molecules and the surface of the adsorbents.

I have tested the CO<sub>2</sub> and CH<sub>4</sub> adsorption properties of these materials. Studies should implement other gas systems, such as hydrogen, nitrogen, ethane, ethylene, and alcohols, and so on, which may provide interesting results attributed to the adding of functional groups.

## 8.3 The Hydrothermal Stability Changes Based on the Topology (Chapter 6)

Chapter 6 demonstrates that even with same connectivity, the MOFs series with different topologies can lead to the different hydrothermal stability. Generally speaking, CuBTC MOFs under **tbo** topology are obviously more stable than the CuBTC MOFs under **fmj** topology. The **fmj** series of MOFs undergo complete loss of crystallinity. The acetamide and bromo functionalized HKUST-1s are relatively more stable than the parent

HKUST-1 material based on the BET surface area changes after water exposure: HKUST-1 losses more BET surface areas after reactivation than these tagged HKUST-1 materials. The topology is the dominant factor for the hydrothermal stability of MOFs.

The degradation mechanism itself is still not clear and may differ drastically for different MOF systems. The lack of understanding of the degradation mechanism under humid conditions may prohibit MOFs from industrial application. Current and future work in the group should combine in-situ XRD and modeling techniques with the water adsorption/desorption test to understand the mechanism of the hydrothermal stability of different MOF systems. The discovery of more high hydrothermally stable MOFs is of paramount importance for the industrial application of MOF materials.

#### **8.4 Optimization of fmj-methoxy Synthesis (Chapter 7)**

In Chapter 7, I have shown the coexistence of multi-phase materials in one-pot synthesis containing in situ ligands reaction, which offers a rare opportunity to examine the role of various reaction variables in determining which structure forms and how the functional groups react during the MOF synthesis. Here, I have conducted a systematic modification of the two variables in solvothermal synthesis conditions to purify the mixed MOF materials: pH value and temperature.

For the fmj-methoxy and [Cu(HOBTC)] mixed materials, the pH value and the choice of temperature have a profound effect on the phase purity. The experimental results show that the formation, phase purity, functionality, and morphology of materials are extremely sensitive to the synthesis parameters explored in this study. Relatively high pH value and low temperature result in the pure desired fmj-methoxy MOF. Thus higher pH value and lower temperature are usually responsible for deprotonation of carboxylate

groups and also can decrease the demethylation of methoxy groups. Finally, I have been able to further optimize the synthesis procedure for fmj-methoxy samples free of other phases, which can be used to obtain pure material for further application.

Because many of the commercially important zeolites may be synthesized without organic templates by altering simple variables such as temperature, reaction time, Si/Al ratio, and pH, a detailed understanding of the role that these variables play in zeolite synthesis remains one of the most important advancements in the field.<sup>14,15</sup> However, very few works have been focused on the synthesis mechanism of MOF materials. We know a little about the synthesis condition impact on the construction of MOF materials. The synthesis of novel MOFs is mostly based on the trial-and-error strategy, so the fully understanding of the synthesis condition effect on MOF synthesis can dramatically decrease the effort for this process. Even for the existing materials, different synthesis routes may lead to different adsorption properties.<sup>16</sup> For the scale-up application of MOF materials, usually the synthesis condition developed at the lab scale does not work for the scaled-up system, so we also need to optimize the synthesis parameters for large-scale systems. Thus, the detailed understanding of the synthesis mechanism is necessary for the further development of the MOF field.

Forster and co-workers used the so-called high-throughput synthesis in the crystallization of MOFs to evaluate rapidly the effect of reaction conditions on the synthesis and to search for optimum conditions for a phase that is difficult to synthesize.<sup>17,18</sup> In future work, the high-throughput method could be used in the optimization of MOF synthesis condition to understand the synthesis mechanism, and to provide insights into crystallization and nucleation mechanism study involving

thermodynamics and kinetics, which will help us to understand the growth process of MOFs.

## 8.5 References

- 1 Jasuja, H., Huang, Y.-g. & Walton, K. S. Adjusting the stability of metal-organic frameworks under humid conditions by ligand functionalization. *Langmuir* **28**, 16874-16880 (2012).
- 2 Zhao, Y. *et al.* Enhancing gas adsorption and separation capacity through ligand functionalization of microporous metal-organic framework structures. *Chem. Eur. J.* **17**, 5101-5109 (2011).
- 3 Dau, P. V., Tanabe, K. K. & Cohen, S. M. Functional group effects on metal-organic framework topology. *Chem. Commun.* **48**, 9370-9372 (2012).
- 4 Tanabe, K. K., Wang, Z. & Cohen, S. M. Systematic functionalization of a metal-organic framework via a postsynthetic modification approach. *J. Am. Chem. Soc.* **130**, 8508-8517 (2008).
- 5 Cmarik, G. E., Kim, M., Cohen, S. M. & Walton, K. S. Tuning the adsorption properties of UiO-66 via ligand functionalization. *Langmuir* **28**, 15606-15613 (2012).
- 6 Kandiah, M. *et al.* Synthesis and Stability of Tagged UiO-66 Zr-MOFs. *Chem. Mater.* **22**, 6632-6640 (2010).
- 7 Couck, S. *et al.* An amine-functionalized MIL-53 metal-organic framework with large separation power for CO<sub>2</sub> and CH<sub>4</sub>. *J. Am. Chem. Soc.* **131**, 6326-6327 (2009).
- 8 Chen, B., Eddaoudi, M., Hyde, S. T., O'Keeffe, M. & Yaghi, O. M. Interwoven metal-organic framework on a periodic minimal surface with extra-large pores. *Science* **291**, 1021-1023 (2001).
- 9 Mu, B., Schoenecker, P. M. & Walton, K. S. Gas adsorption study on mesoporous metal-organic framework UMCM-1. *J. Phys. Chem. C* **114**, 6464-6471 (2010).
- 10 Eddaoudi, M. *et al.* Systematic design of pore size and functionality in isorecticular MOFs and their application in methane storage. *Science* **295**, 469-472 (2002).
- 11 Huang, Y., Qin, W., Li, Z. & Li, Y. Enhanced stability and CO<sub>2</sub> affinity of a UiO-66 type metal-organic framework decorated with dimethyl groups. *Dalton Trans.* **41**, 9283-9285 (2012).
- 12 Biswas, S., Ahnfeldt, T. & Stock, N. New functionalized flexible Al-MIL-53-X (X = -Cl, -Br, -CH<sub>3</sub>, -NO<sub>2</sub>, -(OH)<sub>2</sub>) solids: syntheses, characterization, sorption, and breathing behavior. *Inorg. Chem.* **50**, 9518-9526 (2011).

- 13 Serra-Crespo, P. *et al.* Interplay of metal node and amine functionality in NH<sub>2</sub>-MIL-53: modulating breathing behavior through intra-framework interactions. *Langmuir* **28**, 12916-12922 (2012).
- 14 Breck, D. W. *Zeolite molecular sieves: structure, chemistry, and use*. Vol. 4 (Wiley New York, 1973).
- 15 Szostak, R. *Molecular sieves: principles of synthesis and identification*. (Springer, 1998).
- 16 Haque, E., Khan, N. A., Park, J. H. & Jhung, S. H. Synthesis of a metal-organic framework material, iron terephthalate, by ultrasound, microwave, and conventional electric heating: a kinetic study. *Chem. Eur. J.* **16**, 1046-1052 (2010).
- 17 Forster, P. M., Stock, N. & Cheetham, A. K. A high-throughput investigation of the role of pH, temperature, concentration, and time on the synthesis of hybrid inorganic-organic materials. *Angew. Chem. Int. Ed.* **44**, 7608-7611 (2005).
- 18 Sonnauer, A. *et al.* Giant pores in a chromium 2, 6-naphthalenedicarboxylate open-framework structure with MIL-101 topology. *Angew. Chem. Int. Ed.* **121**, 3849-3852 (2009).

# **APPENDIX A**

## **THE ADSORPTION PROPERTIES OF FMJ-METHOXY MATERIAL**

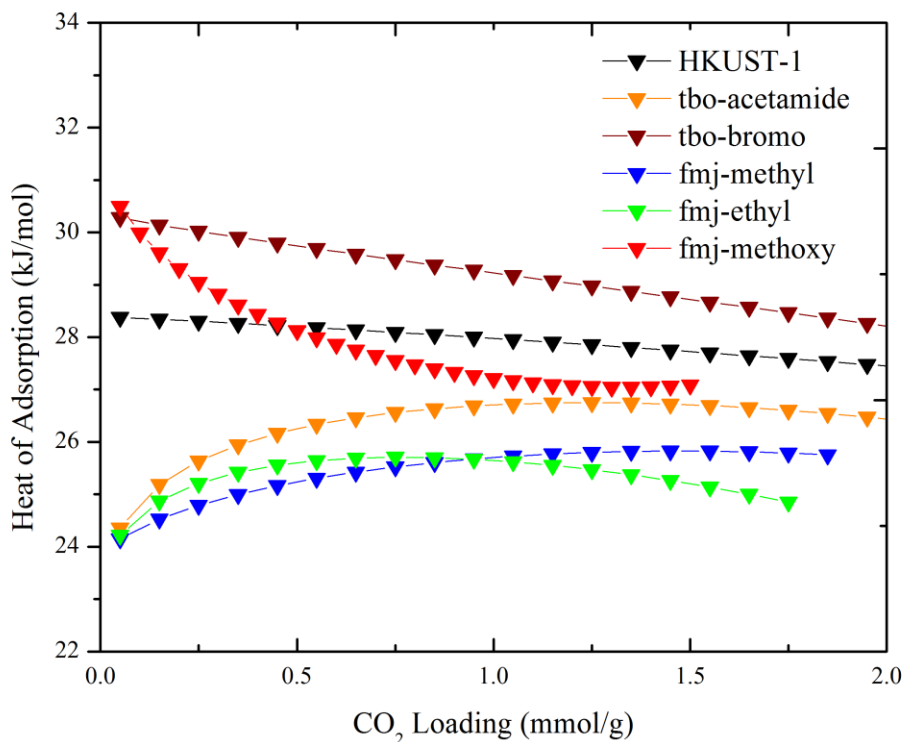
### **Introduction**

In Chapter 4, the results show that fmj-methoxy material is partially collapsed during the activation, but it still provide relatively high BET surface area, 1259 m<sup>2</sup>/g. Chapter 5 shows that the fmj-methoxy material has relatively lower CO<sub>2</sub> and CH<sub>4</sub> uptakes than other functionalized materials, shown in Figure 5.1 – Figure 5.4. There are several peaks in pXRD patterns on the activated fmj-methoxy (Chapter 4). These two observations may be attributed to partial decomposition of the structure, and this collapse of the adsorbent makes the comparison of the impact of the functional groups on the adsorption properties difficult. Thus, I did not provide the isotheric heat of adsorption and CO<sub>2</sub>/CH<sub>4</sub> selectivity data in Chapter 5. I will provide these data here to examine the interaction between the adsorbate molecules and adsorbent surface and the selectivity properties of fmj-methoxy.

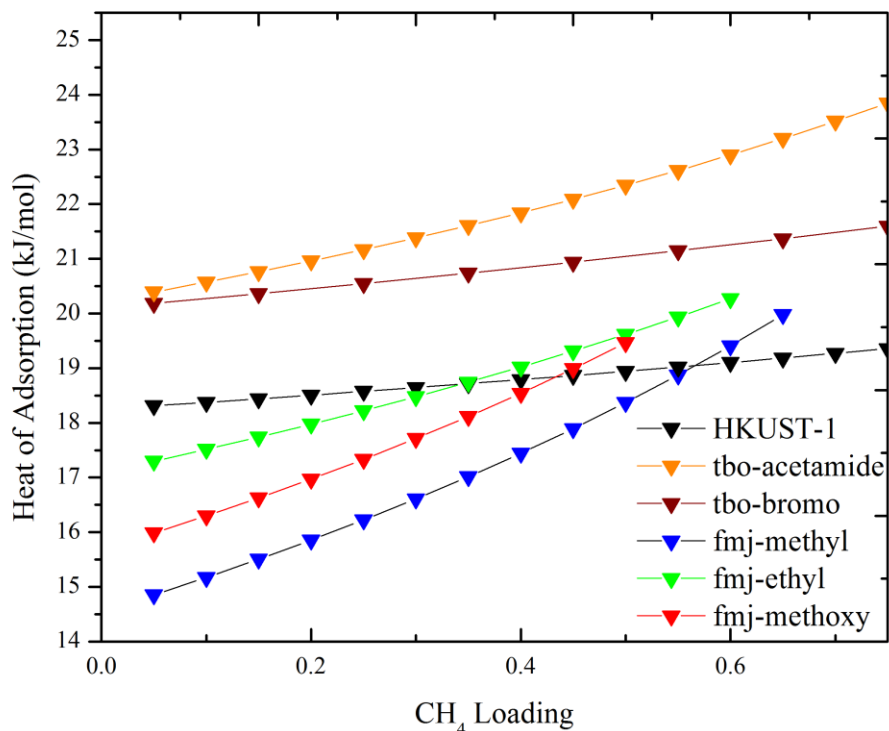
### **Adsorption Properties of fmj-methoxy**

Figure A.1 and Figure A.2 show the CO<sub>2</sub> and CH<sub>4</sub> isosteric heats of adsorption respectively. In Figure A.1, the fmj-methoxy material has higher CO<sub>2</sub> isosteric heat of adsorption than parent HKUST-1 material under low pressure regime. This result may be attributed to the presence of polar functional group in the adsorbent surface. Because there is the partial collapse of the structure, another reason for the high isosteric heat of adsorption is that the active sites may be exposed to the environment during the

activation, even if the functionality is impaired. In Figure A.2, the methane isosteric heat of adsorption is between the fmj-ethyl and fmj-methyl, and it is relatively lower than fmj-ethyl over all loading range. Considering the heat of adsorption for fmj-methoxy together, the heats of adsorption increase when the functional group becomes bulkier, following the order: acetamide > bromo > ethyl > methoxy > methyl. This may be attributed to the presence of methoxy functional group, but the partial decomposition has dramatic effect on the adsorption uptakes of fmj-methoxy.



**Figure A.1** Isosteric heat of adsorption as a function of CO<sub>2</sub> loading including fmj-methoxy



**Figure A.2** Isosteric heat of adsorption as a function of CH<sub>4</sub> loading including fmj-methoxy

Figure A.3 and Figure A.4 shows the selectivities of fmj-methoxy along with other material for 50:50 mixture and 5:95 mixture of CO<sub>2</sub> and CH<sub>4</sub>, respectively. Both figures show that the relatively high selectivities of CO<sub>2</sub>/CH<sub>4</sub>. This result may be attributed to the presence of polar functional group in the adsorbent surface, or the exposure of some active sites during the activation, even if the functionality is impaired.

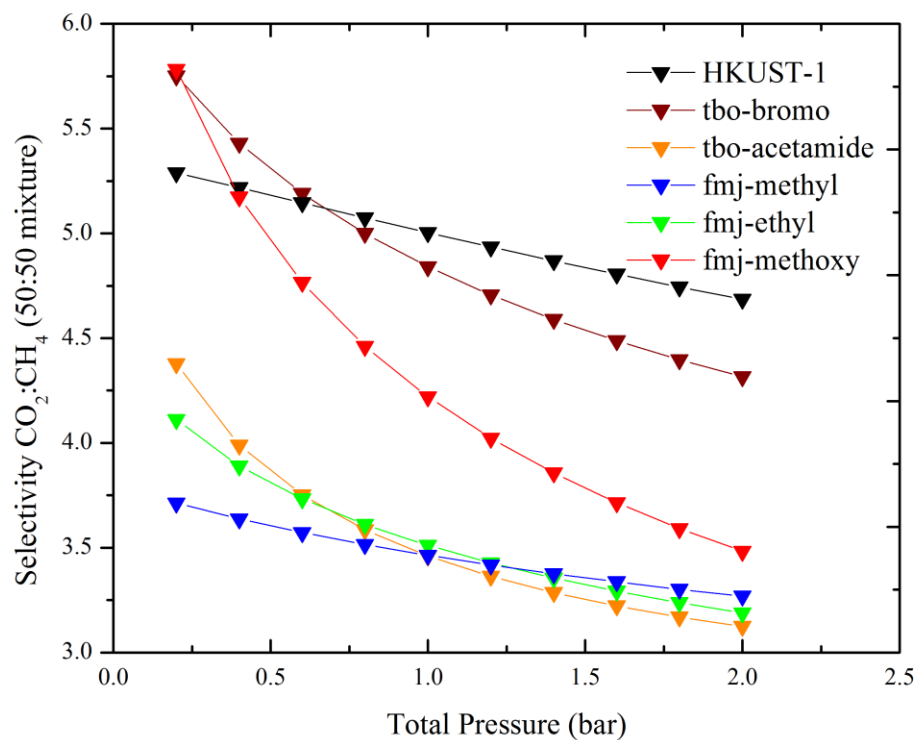


**Figure A.3** Selectivity by applying IAST for a 50:50 CO<sub>2</sub>/CH<sub>4</sub> gas mixture at 25°C including fmj-methoxy

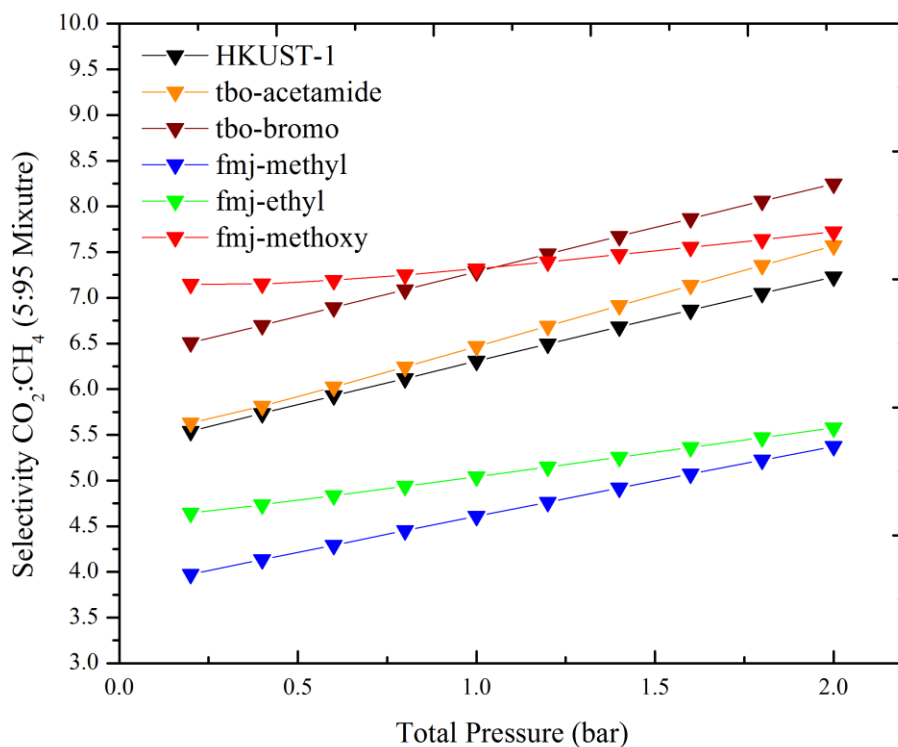


**Figure A.4** Selectivity by applying IAST for a 5:95 CO<sub>2</sub>/CH<sub>4</sub> gas mixture at 25°C including fmj-methoxy

### Conclusions

The fmj-methoxy material have obviously lower uptake than other functionalized materials. The partial decomposition of this material during the activation makes the comparison of the functional groups effect on the adsorption properties difficult. However, it still provides a relatively high isotheric heat of adsorption and CO<sub>2</sub>/CH<sub>4</sub> selectivity.

## APPENDIX B

### THE FORMATION OF OTHER MOFS

#### Introduction

MOF syntheses are generally conducted solvothermally with the use of conventional ovens, which consists of placing a reactant mixture inside a sealed vessel and heating in a conventional oven for 0.5 to 3 days; other synthesis methods also have been used recently.<sup>1-5</sup> The discovery of novel MOF materials mostly depends on the trial-and-error strategy, by varying the parameters of solvothermal synthesis, such as solvent, pH value, and reaction temperature. Previous studies showed that a simple reaction of stoichiometric amounts of cobalt hydroxide and succinic acid in water could form the five known phases via modifying the reaction temperature.<sup>6</sup> The multiple phases involving five Zn/BTB networks were obtained by optimization of the crystallization conditions including time, temperature and solvent.<sup>7</sup>

In chapter 3 and chapter 4, the BTC organic ligands with six different functional groups were synthesized and used to produce the six derivatives of HKUST-1 constructed with copper paddle-wheel clusters under different conditions. In order to obtain these desired structures: isostructural MOFs under the topology or fmj topology, we systematically vary the parameters of the synthesis conditions such as the temperature, solvent, pH value. During this process, we also obtain other phases in different conditions by using the bromo-BTC and methoxy-BTC with copper metal ions. Besides these six BTC ligands with different functional groups, I also synthesized hydroxyl-BTC and trimethyl-BTC. Unfortunately, each increase in the number of parameters raises the number of necessary reactions exponentially. We can not test every combination of

reaction variables. Some ligands are sensitive to the synthesis condition. Thus, I did not form the desired materials by using hydroxyl-BTC and trimethyl-BTC. However, the condensed MOF has been synthesized by using hydroxyl-BTC. The comparison of the synthesis conditions for forming these MOF materials can be used to examine the role of the reaction variables in the construction of MOF structures.

### Ligand Syntheses

All chemicals were obtained commercially (Fisher and Sigma Aldrich) and used without further purification. Besides the ligands we mentioned in Chapter 3 (acetamide-BTC, bromo-BTC, and nitro-BTC) and Chapter 4 (methyl-BTC, ethyl-BTC and methoxy-BTC), I also synthesized ligand hydroxyl-BTC and trimethylBTC (Figure B.1), in order to form the isostructural MOFs under fmj topology or tbo topology. Though systematic modification of synthesis conditions has been conducted via changing the solvent, synthesis temperature, pH value, and reaction time, I did not obtain the desired structure by using these two ligands. The synthesis procedures for hydroxyl-BTC and trimethyl-BTC are listed below.

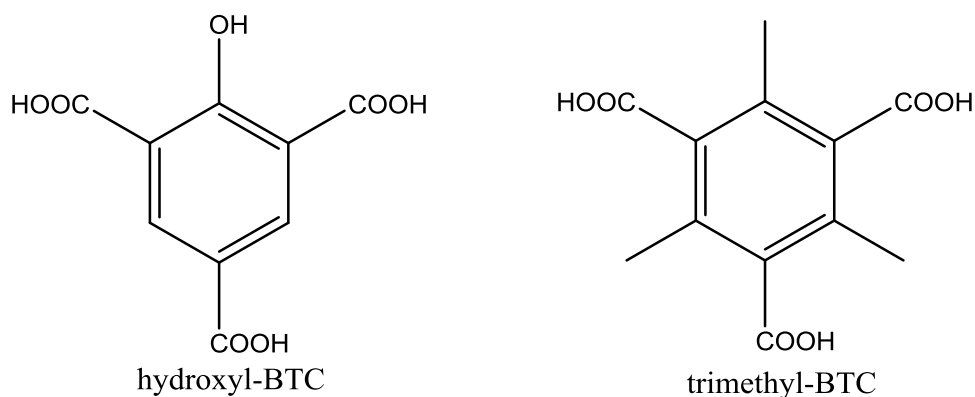


**Figure B.1** The structures of hydroxyl-BTC and trimethyl-BTC

**Preparation of hydroxyl-1,3,5-benzenetricarboxylic acid (hydroxyl-BTC, Figure B.2):** A mixture of 2-methoxy-benzen-1,3,5-tricarboxylic acid (4 g) and 48% HBr (83.3 mL) was placed in a 250 mL round bottom flask. The reaction mixture was heated to reflux at 150 °C for 48 h. After 48 h, the mixture was cooling down. The resulting heterogeneous mixture was added with water. Then, the mixture was extracted with diethyl ether for one day. Removal of the solvent (diethyl ether) in vacuo affords product hydroxyl-BTC (2 g). <sup>1</sup>H NMR (300 MHz, DMSO): 8.23 (s, 2H).

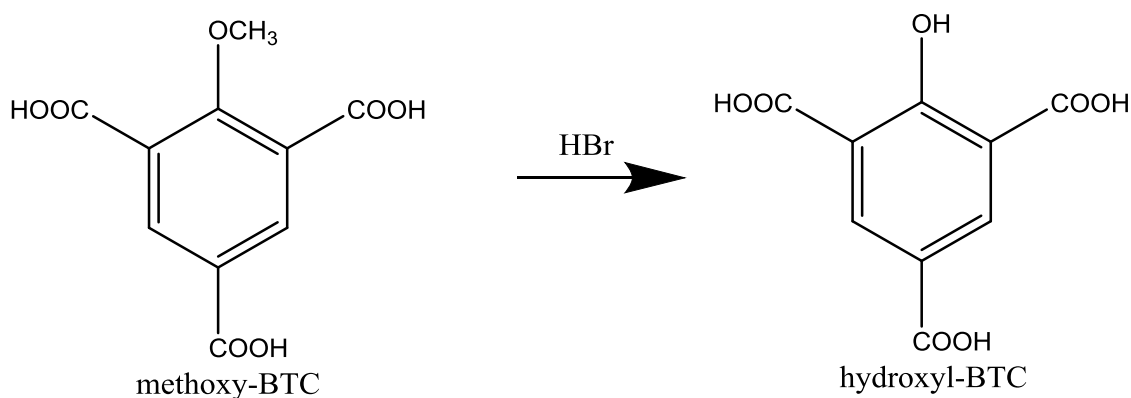


**Figure B.2** Synthesis procedure of hydroxyl-BTC

**Preparation of trimethyl-1,3,5-benzenetricarboxylic acid (trimethyl-BTC, Figure B.3):** A mixture of 1,3,5-tris (bromomethyl)-2,4,6-trimethylbenzene (10 g) and NaOAc (15 g) in DMF (80 mL) was stirred for 15 h at 30°C. the reaction mixture was poured into water and the white solid was filtrated. 7.9 g crude product A1 was obtained. A mixture of **A1** and lithium hydroxide hydrate in reagent grade ethanol was heated at reflux overnight. The resulting heterogeneous reaction mixture was cooled to room temperature, and evaporated to dryness. The resulting white solid was suspended in cold

water, filtered and washed with water, dried under heating to 150 °C in vacuo to provide **A2**.

A suspension of **A2** (0.9 g, 4.3 mmol) in reagent grade acetone (50 mL) was treated dropwise with Jones reagent (14 mL) at 40 °C. The mixture was stirred for 20 min at 4 °C, 20 min at room temperature, and 5 min at 30 °C. The resulting green heterogeneous mixture was poured into cold water (150 mL) and extracted with diethyl ether (50 mL) for three times. The combined organic fractions were extracted with water (50 mL), separated, and dried with anhydrous sodium sulfate. The tri-methyl BTC was obtained after the solvent was evaporated under reduced pressure. <sup>1</sup>H NMR (300 MHz, DMSO): 3.32 (s, 9H).

Jones Reagent preparation: 4.67 g Cr(VI)O<sub>3</sub> is dissolved in 4.67 mL H<sub>2</sub>SO<sub>4</sub>. The mixture solution is added very slowly to 14 mL water that has been cooled to 0°C while stirring.

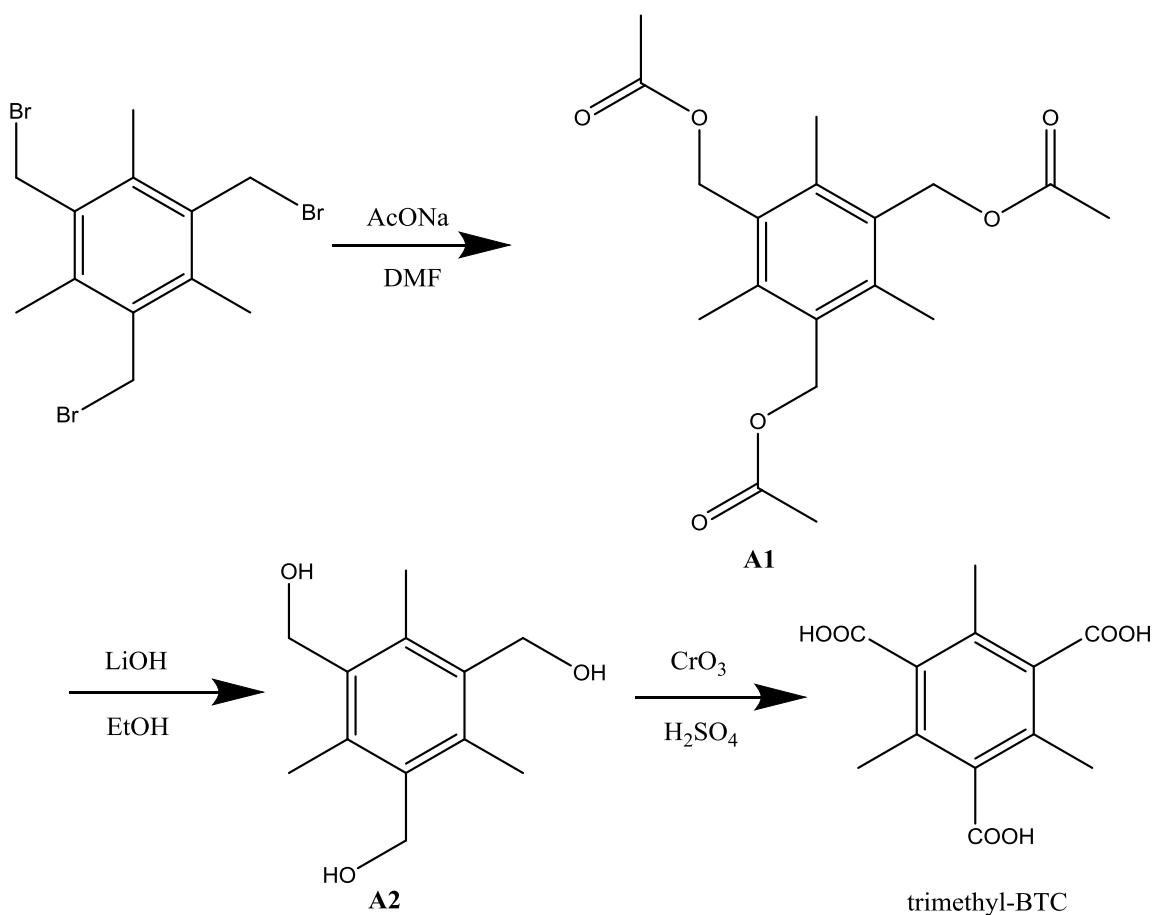


**Figure B.3** Synthesis procedure of trimethyl-BTC

### MOF Syntheses

**Synthesis of CuHOBTC-2:** A mixture of Cu(NO<sub>3</sub>)<sub>2</sub> · 3H<sub>2</sub>O (72.48 mg), hydroxyl-BTC (44 mg), and DMF (6 mL) with 1M HCl aqueous solution (0.15 mL) was placed in a 20 mL glass vial, and the resulting mixture was heated in a conventional oven at 120°C for 72 h and cooled to room temperature. The needle shape green crystal was formed.

**Synthesis of CuBrBTC:** A mixture of Cu(NO<sub>3</sub>)<sub>2</sub> · 3H<sub>2</sub>O (72.48 mg), bromo-BTC (57.8 mg) in DMF (3 mL) and water (3 mL) was placed in a 20 mL glass vial, and the resulting mixture was heated in a conventional oven at 120°C for 72 h and cooled to room temperature. The needle shape green crystal was formed.

## Structure Description

Single-crystal XRD data of MOFs (Cu(HOBTC)-2 and CuBrBTC) were collected on a single crystal Bruker APEX CCD diffraction system with CuK $\alpha$  radiation. The structures were solved by direct methods with the help of SHELX-97 and refined by full-matrix least-squared techniques using SHELXL-97.

The single crystal X-ray Crystallographic studies show that CuBrBTC, Cu(HOBTC), Cu(HOBTC)-2, have the same structural. Cu(HOBTC) and Cu(HOBTC)-2 are the same materials synthesized from different organic ligands, methoxy-BTC and hydroxyl-BTC. Figure B.4 and Figure B.5 show the structure of Cu(HOBTC) (or Cu(HOBTC)-2) and Cu(BrBTC) respectively.

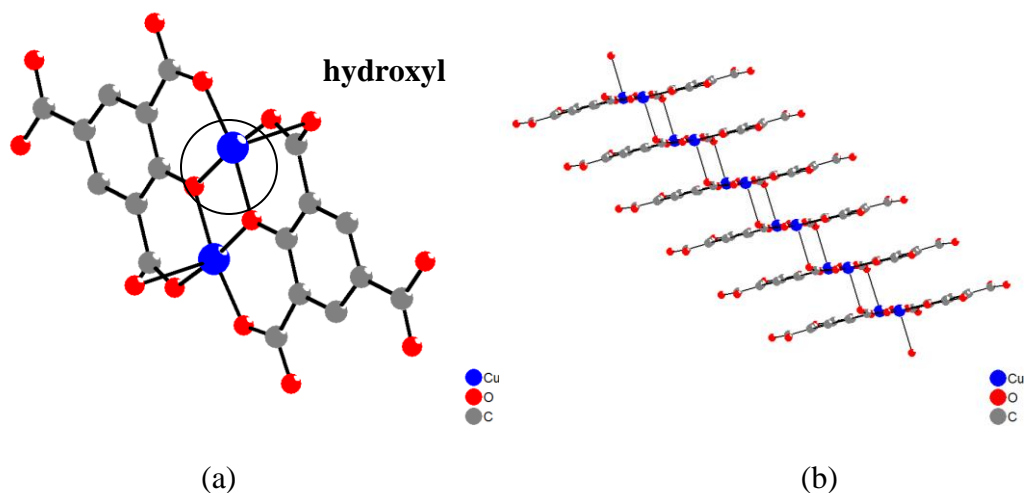


**Figure B.4** (a) Cu(HOBTC) (or Cu(HOBTC)-2) structure unit; (b) View of layers stacked in an ABAB manner of Cu(HOBTC) (or Cu(HOBTC)-2)

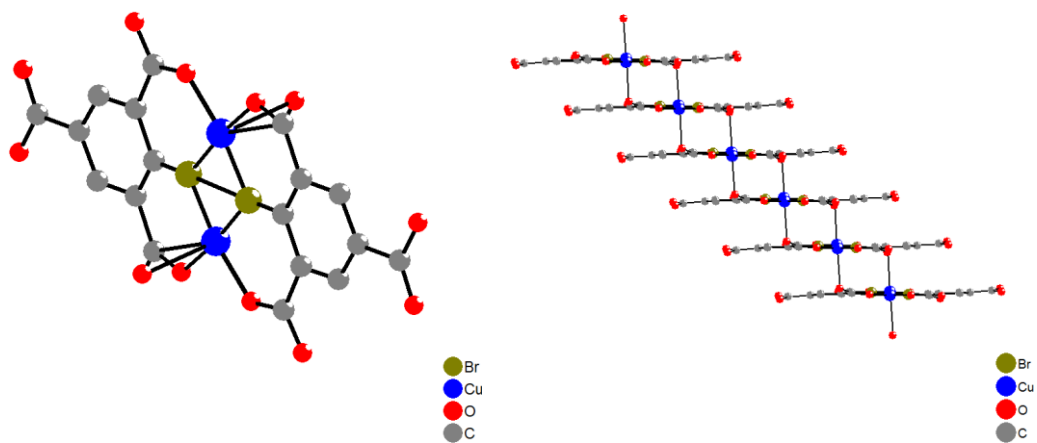


**Figure B.5** (a) CuBrBTC structure unit; (b) View of layers stacked in an ABAB manner of CuBrBTC

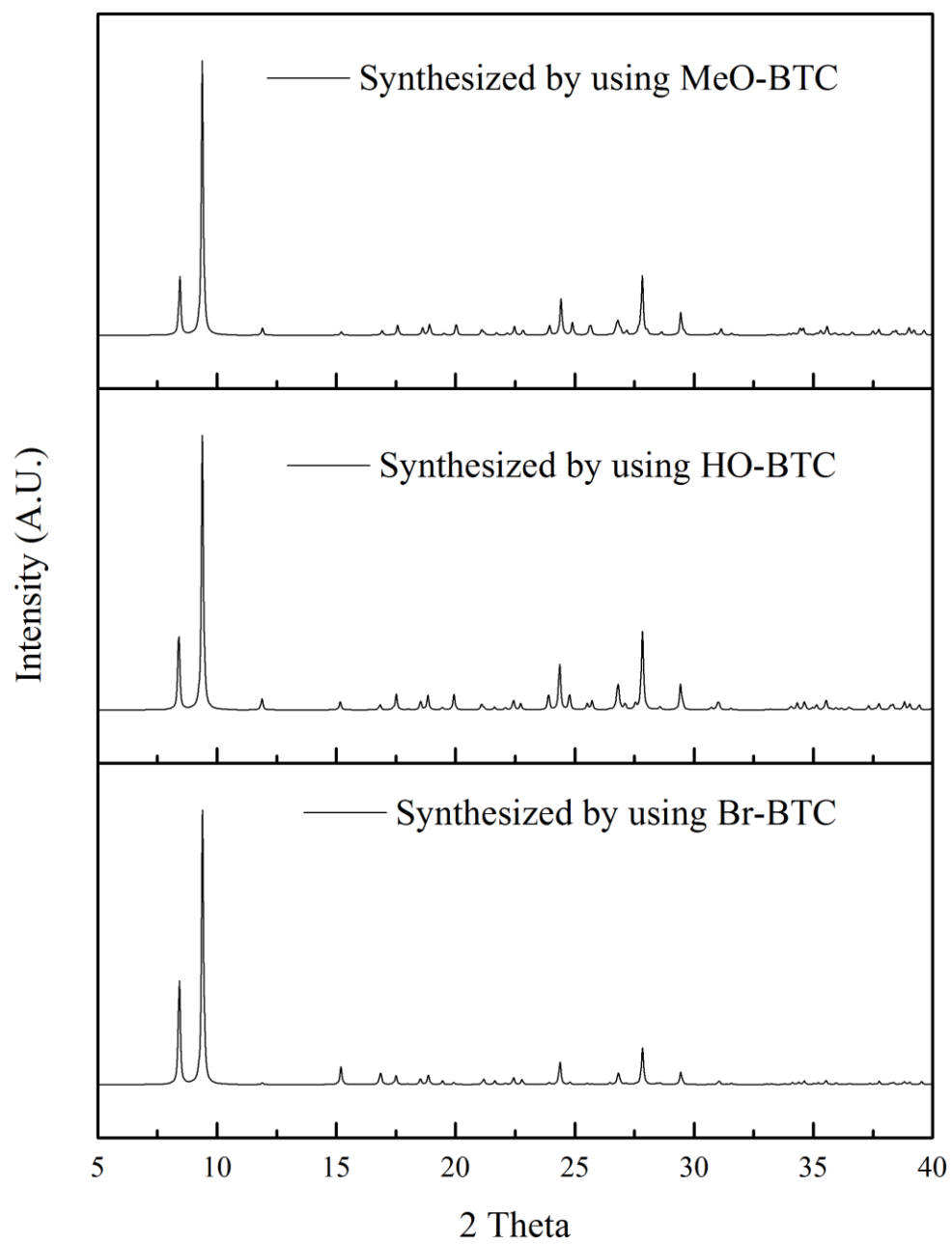


**Figure B.6** The simulated pXRD patterns for Cu(HOBTC) (top), Cu(HOBTC)-2 (middle), and CuBrBTC (bottom)

For convenience, I will use the Cu(HOBTC) as an example to describe the structure of this series of materials. Cu(HOBTC) is a needle-shaped blue crystal, whose structure is shown in Figure B.4. The carboxylate groups in Cu(HOBTC) are partially deprotonated. Two carboxyl groups and one hydroxyl group of one ligand are deprotonated and coordinate to two copper ions, which connect the two organic ligands together and form one layer. As shown in Figure B.4 (b), layers are stacked via the coordination between the copper ions and the oxygen atoms of the carboxylate groups to form 1D MOF materials.

Unfortunately, I did not obtain any of crystal structures by using trimethyl-BTC ligands. The probable reason may be is that steric effect of functional groups may have effect on the construction of MOFs, which make the formation of MOFs materials difficult by using this ligand than parent BTC ligands.

### **Conclusions**

The pH value has effect on synthesis conditions: the Cu(HOBTC) and Cu(HOBTC)-2 are both formed in the DMF solvent with addition of 1M HCl aqueous solution. Considering the results from Chapter 4 about the formation of fmj-methoxy, the low pH value can lead to the partially deprotonation of BTC ligands and then result in the formation of condensed materials Cu(HOBTC). Hydroxyl groups in hydroxyl-BTC ligand is easily coordinated with metal ions and under the acidic condition, the carboxylic groups are partially deprotonated. Similar to Cu(HOBTC), instead of forming the isostructural MOFs under tbo or fmj topology, hydroxyl-BTC has been used to form Cu(HOBTC)-2 under low pH condition. Considering the synthesis condition of the tbo-bromo (Chapter 3), tbo-bromo is synthesized in the DMF solvent, while CuBrBTC is

formed in the mixture solvent of DMF and water. Thus, the use of different solvent has effect on the formation of MOF materials and different solvent has different effect on the deprotonation of the organic ligands. The mixture of DMF and water leads to partial deprotonation of bromo-BTC and results in the formation of CuBrBTC. Unfortunately, I did not obtain any of crystal structures by using trimethyl-BTC ligands. The probable reason may be is that steric effect of functional groups may have effect on the construction of MOFs, which make the formation of MOFs materials difficult by using this ligand. The systematic variation of the synthesis conditions may leads to the formation of isostructural MOFs under tbo or fmj topology by using hydroxyl and trimethyl functionalized ligands. However, this process is time-consuming. The fully understanding about how the parameters affect the construction of MOFs may dramatically speed up this process.

## References

- 1 Loera-Serna, S. *et al.* Electrochemical behavior of [Cu<sub>3</sub>(BTC)<sub>2</sub>] metal–organic framework: The effect of the method of synthesis. *J. Alloys Compd.* **540**, 113-120 (2012).
- 2 Xu, L., Choi, E.-Y. & Kwon, Y.-U. Ionothermal synthesis of a 3D Zn–BTC metal-organic framework with distorted tetranuclear [Zn<sub>4</sub>(μ<sub>4</sub>-O)] subunits. *Inorganic Chem. Commun.* **11**, 1190-1193 (2008).
- 3 Klimakow, M., Klobes, P., Thünemann, A. F., Rademann, K. & Emmerling, F. Mechanochemical Synthesis of metal-organic frameworks: a fast and facile approach toward quantitative yields and high specific surface areas. *Chem. Mater.* **22**, 5216-5221 (2010).
- 4 Lu, C.-M., Liu, J., Xiao, K. & Harris, A. T. Microwave enhanced synthesis of MOF-5 and its CO<sub>2</sub> capture ability at moderate temperatures across multiple capture and release cycles. *Chem. Eng. J.* **156**, 465-470 (2010).
- 5 Lin, Z., Wragg, D. S. & Morris, R. E. Microwave-assisted synthesis of anionic metal-organic frameworks under ionothermal conditions. *Chem. Commun.*, 2021-2023 (2006).
- 6 Forster, P. M., Burbank, A. R., Livage, C., Férey, G. & Cheetham, A. K. The role of temperature in the synthesis of hybrid inorganic–organic materials: the example of cobalt succinates. *Chem. Commun.*, 368-369 (2004).
- 7 Caskey, S. R., Wong-Foy, A. G. & Matzger, A. J. Phase selection and discovery among five assembly modes in a coordination polymerization. *Inorg. Chem.* **47**, 7751-7756 (2008).

## APPENDIX C

### RAW DATA

#### Chapter 5: Tuning the Gas Adsorption Behaviors via Functionalization of BTC

#### Precursors

**Table C.1** Adsorption Data for HKUST-1 CO<sub>2</sub> and CH<sub>4</sub> Isotherm at 298 K

Pressure (bar)	CO <sub>2</sub> uptake (mmol/g)	Pressure (bar)	CH <sub>4</sub> uptake (mmol/g)
0.00112	0	0.00166	0
0.01489	0.08549	0.01596	0.02388
0.10349	0.55476	0.09935	0.12125
0.20559	1.04994	0.20131	0.21612
0.4015	1.91631	0.40203	0.39003
0.60342	2.70181	0.60155	0.54842
0.80254	3.37913	0.80134	0.69586
1.0034	3.97782	1.00193	0.83574
1.50066	5.1753	1.49879	1.15597
2.00273	6.10214	2.00219	1.45644
3.00072	7.42091	2.99738	1.99693
3.99925	8.2982	3.99805	2.48286
6.01476	9.35292	5.99672	3.34148
7.99498	9.95808	7.99632	4.06866
10.02318	10.36643	9.99605	4.68773
11.99912	10.66128	11.99618	5.21743
14.99979	10.99318	14.99672	5.87527
15.99926	11.08296	15.99725	6.06717
17.99873	11.24218	17.99779	6.4107
19.99619	11.37764	19.99873	6.7175

**Table C.2** Adsorption Data for tbo-bromo CO<sub>2</sub> and CH<sub>4</sub> Isotherm at 298 K

Pressure (bar)	CO <sub>2</sub> uptake (mmol/g)	Pressure (bar)	CH <sub>4</sub> uptake (mmol/g)
0.00139	0	0.00112	0
0.01155	0.0949	0.01676	0.03722
0.10122	0.78588	0.10215	0.16759
0.19984	1.4006	0.19984	0.28702
0.40377	2.48125	0.40283	0.51227
0.60062	3.33588	0.60102	0.71241
0.80655	4.08926	0.802	0.89842
1.0042	4.71652	1.00019	1.06963
1.49892	5.96036	1.49985	1.47037
2.00246	6.91912	1.99805	1.83347
3.00206	8.24779	2.99818	2.48546
4.00246	9.11004	3.99925	3.05142
5.99765	10.13725	5.99725	4.01742
8.01048	10.74622	8.00286	4.81568
9.99485	11.15574	9.99645	5.47865
12.01676	11.4678	11.99886	6.03162
14.99953	11.81163	14.99619	6.72384
15.99832	11.9084	15.99659	6.9203
17.99458	12.08167	17.99832	7.27751
19.99913	12.23091	19.99539	7.59786

**Table C.3** Adsorption Data for tbo-acetamide CO<sub>2</sub> and CH<sub>4</sub> Isotherm at 298 K

Pressure (bar)	CO <sub>2</sub> uptake (mmol/g)	Pressure (bar)	CH <sub>4</sub> uptake (mmol/g)
0.00206	0	0.00112	0
0.01462	0.04586	0.01596	0.04631
0.10322	0.36504	0.09854	0.25809
0.20372	0.87458	0.20986	0.45817
0.4031	1.7225	0.40283	0.75329
0.60355	2.51735	0.60369	1.02245
0.80241	3.22683	0.80254	1.25699
1.00406	3.85436	1.00286	1.46843
1.50413	5.09305	1.49905	1.93494

**Table C.3 Continued**

2.00126	6.02441	2.00126	2.34344
3.00032	7.2829	2.99845	3.02669
3.99792	8.07278	4.00139	3.58924
6.03213	9.04226	5.99685	4.47784
7.99966	9.6474	7.99658	5.16328
9.99578	10.10464	9.99912	5.71039
11.99511	10.47638	11.99658	6.16884
14.99712	10.94268	14.99939	6.73956
15.99806	11.08597	15.99712	6.90535
17.99993	11.34866	17.99859	7.20606
19.99672	11.59761	19.99873	7.47813

**Table C.4** Adsorption Data for fmj-methyl CO<sub>2</sub> and CH<sub>4</sub> Isotherm at 298 K

Pressure (bar)	CO <sub>2</sub> uptake (mmol/g)	Pressure (bar)	CH <sub>4</sub> uptake (mmol/g)
-8.1E-4	0	0	0
0.01509	0.05273	0.01336	0.02721
0.42201	0.8564	0.41319	0.48937
0.81223	2.50491	0.81357	0.833
1.22156	3.53389	1.21435	1.12558
1.61606	4.39649	1.61365	1.3823
2.00413	5.09799	1.99785	1.61175
4.00227	7.49771	3.99946	2.58924
5.99892	8.70742	5.99786	3.35999
8.00146	9.46812	7.99746	3.97474
10.00133	9.96081	9.99746	4.49053
13.9996	10.60828	13.99572	5.29403
20.00468	11.32826	19.99759	6.146

**Table C.5** Adsorption Data for fmj-ethyl CO<sub>2</sub> and CH<sub>4</sub> Isotherm at 298 K

Pressure (bar)	CO <sub>2</sub> uptake (mmol/g)	Pressure (bar)	CH <sub>4</sub> uptake (mmol/g)
-1.42E-4	0	9.27E-4	0
0.01322	0.01146	0.02031	0.0207
0.42188	1.3668	0.41827	0.37625
0.81771	2.89991	0.8133	0.66465
1.21582	4.01136	1.21488	0.91624
1.61338	4.82277	1.61525	1.14616
2.00413	5.50235	2.0052	1.35945
4.002	7.57976	3.99999	2.27609
5.99411	8.69671	6.0016	3.02552
8.00013	9.38081	7.99759	3.63693
9.99759	9.83506	9.99772	4.14372
13.99853	10.43133	13.99278	4.94434
19.9988	10.88252	19.99038	5.72408

**Table C.6** Adsorption Data for fmj-methoxy CO<sub>2</sub> and CH<sub>4</sub> Isotherm at 298 K

Pressure (bar)	CO <sub>2</sub> uptake (mmol/g)	Pressure (bar)	CH <sub>4</sub> uptake (mmol/g)
3.21E-4	0	9.89E-4	0
0.01622	0.05185	0.02077	0.01135
0.09935	0.27871	0.09453	0.04773
0.20011	0.49665	0.20171	0.09807
0.40003	0.82705	0.40203	0.18625
0.60422	1.08098	0.60168	0.26834
0.80521	1.28571	0.80027	0.34522
1.00393	1.45761	1.00406	0.41862
1.49905	1.79243	1.51161	0.58202
2.0038	2.0478	1.99912	0.72137
3.00206	2.406	3.00821	0.96205
4.00219	2.65483	4.00781	1.15355
5.99845	2.98904	6.00353	1.44582
8.02024	3.21625	8.00166	1.66131
9.99819	3.38452	9.99845	1.83053
11.99886	3.52021	12.00768	1.96684

**Table C.6** Continued

14.99832	3.68444	14.99659	2.14421
15.99605	3.72717	15.99538	2.18843
17.99873	3.81209	17.99579	2.3086
19.99632	3.89382	19.99338	2.37446

**Table C.7** Isothermic Heats of Adsorption Data for HKUST-1 as a Function of CO<sub>2</sub> or CH<sub>4</sub>

Loading

CO <sub>2</sub> loading (mmol/g)	Heat of Adsorption (kJ/mol)	CH <sub>4</sub> loading (mmol/g)	Heat of Adsorption (kJ/mol)
0.05	28.37679	0.05	18.31165
0.15	28.34094	0.1	18.37543
0.25	28.30275	0.15	18.44065
0.35	28.26295	0.2	18.50737
0.45	28.22182	0.25	18.57563
0.55	28.17951	0.3	18.6455
0.65	28.13609	0.35	18.71702
0.75	28.09161	0.4	18.79027
0.85	28.0461	0.45	18.86529
0.95	27.99959	0.5	18.94217
1.05	27.95207	0.55	19.02095
1.15	27.90355	0.6	19.10173
1.25	27.85403	0.65	19.18458
1.35	27.80351	0.7	19.26957
1.45	27.75196	0.75	19.35679
1.55	27.69939		
1.65	27.64577		
1.75	27.59108		
1.85	27.53532		
1.95	27.47846		

**Table C.8** Isothermic Heats of Adsorption Data for tbo-bromo as a Function of CO<sub>2</sub> or CH<sub>4</sub>

Loading

CO <sub>2</sub> loading (mmol/g)	Heat of Adsorption (kJ/mol)	CH <sub>4</sub> loading (mmol/g)	Heat of Adsorption (kJ/mol)
0.05	30.27904	0.05	20.18551
0.15	30.14045	0.15	20.3618
0.25	30.01866	0.25	20.54563
0.35	29.90447	0.35	20.73752
0.45	29.79475	0.45	20.93799
0.55	29.68798	0.55	21.14764
0.65	29.58323	0.65	21.36712
0.75	29.4799	0.75	21.59714
0.85	29.37758		
0.95	29.27594		
1.05	29.17476		
1.15	29.07383		
1.25	28.973		
1.35	28.87213		
1.45	28.77112		
1.55	28.66987		
1.65	28.56829		
1.75	28.46631		
1.85	28.36385		
1.95	28.26086		

**Table C.9** Isothermic Heats of Adsorption Data for tbo-acetamide as a Function of CO<sub>2</sub> orCH<sub>4</sub> Loading

CO <sub>2</sub> loading (mmol/g)	Heat of Adsorption (kJ/mol)	CH <sub>4</sub> loading (mmol/g)	Heat of Adsorption (kJ/mol)
0.05	24.35682	0.05	20.39481
0.15	25.18733	0.1	20.57624
0.25	25.63662	0.15	20.7652
0.35	25.94111	0.2	20.96218
0.45	26.16404	0.25	21.16769
0.55	26.33286	0.3	21.3823

**Table C.9** Continued

0.65	26.46227	0.35	21.60664
0.75	26.56113	0.4	21.84139
0.85	26.63524	0.45	22.08729
0.95	26.68861	0.5	22.34516
1.05	26.72412	0.55	22.6159
1.15	26.74393	0.6	22.90052
1.25	26.74968	0.65	23.20011
1.35	26.74265	0.7	23.5159
1.45	26.72384	0.75	23.84924
1.55	26.69406		
1.65	26.65396		
1.75	26.60406		
1.85	26.54478		
1.95	26.47648		

**Table C.10** Isothermic Heats of Adsorption Data for fmj-methyl as a Function of CO<sub>2</sub> orCH<sub>4</sub> Loading

CO <sub>2</sub> loading (mmol/g)	Heat of Adsorption (kJ/mol)	CH <sub>4</sub> loading (mmol/g)	Heat of Adsorption (kJ/mol)
0.05	24.14954	0.05	14.85349
0.15	24.52995	0.1	15.17207
0.25	24.79255	0.15	15.50567
0.35	24.99774	0.2	15.85538
0.45	25.16543	0.25	16.22241
0.55	25.30533	0.3	16.60811
0.65	25.42303	0.35	17.01396
0.75	25.5221	0.4	17.44159
0.85	25.60493	0.45	17.89284
0.95	25.67321	0.5	18.36975
1.05	25.72814	0.55	18.87463
1.15	25.7706	0.6	19.41003
1.25	25.80121	0.65	19.97888
1.35	25.82041		
1.45	25.82852		
1.55	25.82569		
1.65	25.81201		

**Table C.10** Continued

1.75	25.78746		
1.85	25.75195		

**Table C.11** Isothermic Heats of Adsorption Data for fmj-ethyl as a Function of CO<sub>2</sub> or CH<sub>4</sub>

Loading

CO <sub>2</sub> loading (mmol/g)	Heat of Adsorption (kJ/mol)	CH <sub>4</sub> loading (mmol/g)	Heat of Adsorption (kJ/mol)
0.05	24.21846	0.05	17.29608
0.15	24.87436	0.1	17.5135
0.25	25.21152	0.15	17.73961
0.35	25.42158	0.2	17.97494
0.45	25.55757	0.25	18.22008
0.55	25.64293	0.3	18.47565
0.65	25.69033	0.35	18.74235
0.75	25.70747	0.4	19.02091
0.85	25.69939	0.45	19.31216
0.95	25.66958	0.5	19.61699
1.05	25.62054	0.55	19.93639
1.15	25.55412	0.6	20.27143
1.25	25.47171		
1.35	25.37435		
1.45	25.26286		
1.55	25.13787		
1.65	24.99985		
1.75	24.84915		

**Table C.12** Selectivity CO<sub>2</sub>:CH<sub>4</sub> Data for HKUST-1

Total pressure (bar)	Selectivity CO <sub>2</sub> :CH <sub>4</sub> (50:50 mixture)	Selectivity CO <sub>2</sub> :CH <sub>4</sub> (5:95 mixture)
	0.02	5.34041
0.04	5.33617	5.38282

**Table C.12 Continued**

0.06	5.33126	5.40261
0.08	5.3259	5.42234
0.1	5.32021	5.44204
0.12	5.31427	5.4617
0.14	5.30812	5.48133
0.16	5.3018	5.50093
0.18	5.29534	5.5205
0.2	5.28876	5.54005
0.22	5.28207	5.55958
0.24	5.2753	5.57908
0.26	5.26845	5.59855
0.28	5.26153	5.61801
0.3	5.25455	5.63745
0.32	5.24752	5.65686
0.34	5.24045	5.67625
0.36	5.23334	5.69563
0.38	5.22619	5.71498
0.4	5.21902	5.73432
0.42	5.21183	5.75364
0.44	5.20461	5.77294
0.46	5.19738	5.79222
0.48	5.19014	5.81148
0.5	5.18289	5.83073
0.52	5.17563	5.84995
0.54	5.16836	5.86916
0.56	5.1611	5.88836
0.58	5.15383	5.90753
0.6	5.14656	5.92669
0.62	5.1393	5.94583
0.64	5.13204	5.96496
0.66	5.12479	5.98407
0.68	5.11755	6.00316
0.7	5.11032	6.02224
0.72	5.1031	6.0413
0.74	5.09589	6.06034
0.76	5.08869	6.07937
0.78	5.08151	6.09838
0.8	5.07434	6.11737
0.82	5.06718	6.13635
0.84	5.06005	6.15532
0.86	5.05293	6.17426
0.88	5.04583	6.1932
0.9	5.03874	6.21211

**Table C.12** Continued

0.92	5.03168	6.23101
0.94	5.02464	6.2499
0.96	5.01761	6.26877
0.98	5.01061	6.28762
1	5.00363	6.30646
1.02	4.99667	6.32529
1.04	4.98973	6.34409
1.06	4.98282	6.36289
1.08	4.97592	6.38167
1.1	4.96905	6.40043
1.12	4.96221	6.41918
1.14	4.95539	6.43791
1.16	4.94859	6.45663
1.18	4.94181	6.47533
1.2	4.93506	6.49402
1.22	4.92834	6.51269
1.24	4.92164	6.53135
1.26	4.91496	6.54999
1.28	4.90831	6.56862
1.3	4.90169	6.58724
1.32	4.89509	6.60584
1.34	4.88852	6.62442
1.36	4.88197	6.64299
1.38	4.87545	6.66154
1.4	4.86895	6.68008
1.42	4.86248	6.69861
1.44	4.85603	6.71712
1.46	4.84961	6.73562
1.48	4.84322	6.7541
1.5	4.83686	6.77257
1.52	4.83051	6.79102
1.54	4.8242	6.80946
1.56	4.81791	6.82788
1.58	4.81165	6.84629
1.6	4.80541	6.86469
1.62	4.7992	6.88307
1.64	4.79302	6.90144
1.66	4.78686	6.91979
1.68	4.78073	6.93813
1.7	4.77463	6.95645
1.72	4.76855	6.97476
1.74	4.76249	6.99306
1.76	4.75646	7.01134

**Table C.12** Continued

1.78	4.75046	7.02961
1.8	4.74449	7.04786
1.82	4.73854	7.0661
1.84	4.73261	7.08433
1.86	4.72671	7.10254
1.88	4.72084	7.12073
1.9	4.71499	7.13892
1.92	4.70917	7.15708
1.94	4.70337	7.17524
1.96	4.6976	7.19338
1.98	4.69185	7.21151
2	4.68613	7.22962

**Table C.13** Selectivity CO<sub>2</sub>:CH<sub>4</sub> Data for tbo-bromo

Total pressure (bar)	Selectivity CO <sub>2</sub> :CH <sub>4</sub> (50:50 mixture)	Selectivity CO <sub>2</sub> :CH <sub>4</sub> (5:95 mixture)
0.02	6.2316	6.35807
0.04	6.15321	6.37131
0.06	6.08685	6.3863
0.08	6.02777	6.40228
0.1	5.97385	6.41893
0.12	5.92391	6.43607
0.14	5.8772	6.45359
0.16	5.83317	6.47142
0.18	5.79146	6.48949
0.2	5.75175	6.50777
0.22	5.71383	6.52623
0.24	5.6775	6.54484
0.26	5.64261	6.56358
0.28	5.60902	6.58243
0.3	5.57664	6.60138
0.32	5.54536	6.62042
0.34	5.51511	6.63954
0.36	5.48581	6.65872
0.38	5.45739	6.67797
0.4	5.4298	6.69727
0.42	5.403	6.71662

**Table C.13** Continued

0.44	5.37693	6.73601
0.46	5.35156	6.75543
0.48	5.32684	6.77489
0.5	5.30275	6.79438
0.52	5.27924	6.8139
0.54	5.25631	6.83344
0.56	5.2339	6.853
0.58	5.21201	6.87257
0.6	5.19062	6.89216
0.62	5.16968	6.91177
0.64	5.1492	6.93138
0.66	5.12915	6.95101
0.68	5.10952	6.97064
0.7	5.09028	6.99027
0.72	5.07143	7.00992
0.74	5.05294	7.02956
0.76	5.03481	7.0492
0.78	5.01703	7.06885
0.8	4.99957	7.08849
0.82	4.98244	7.10814
0.84	4.96561	7.12778
0.86	4.94909	7.14741
0.88	4.93285	7.16704
0.9	4.9169	7.18667
0.92	4.90122	7.20629
0.94	4.8858	7.2259
0.96	4.87064	7.24551
0.98	4.85572	7.26511
1	4.84105	7.28469
1.02	4.82661	7.30427
1.04	4.8124	7.32384
1.06	4.79842	7.3434
1.08	4.78465	7.36295
1.1	4.77108	7.38248
1.12	4.75773	7.40201
1.14	4.74457	7.42152
1.16	4.73161	7.44102
1.18	4.71883	7.46051
1.2	4.70624	7.47998
1.22	4.69383	7.49944
1.24	4.6816	7.51889
1.26	4.66954	7.53832
1.28	4.65764	7.55774

**Table C.13** Continued

1.3	4.64591	7.57714
1.32	4.63434	7.59653
1.34	4.62292	7.6159
1.36	4.61166	7.63526
1.38	4.60054	7.6546
1.4	4.58958	7.67392
1.42	4.57875	7.69323
1.44	4.56806	7.71252
1.46	4.55751	7.7318
1.48	4.5471	7.75106
1.5	4.53681	7.7703
1.52	4.52666	7.78953
1.54	4.51662	7.80874
1.56	4.50671	7.82793
1.58	4.49693	7.8471
1.6	4.48726	7.86626
1.62	4.4777	7.8854
1.64	4.46826	7.90452
1.66	4.45893	7.92362
1.68	4.44971	7.94271
1.7	4.4406	7.96177
1.72	4.43159	7.98082
1.74	4.42268	7.99985
1.76	4.41388	8.01887
1.78	4.40517	8.03786
1.8	4.39656	8.05684
1.82	4.38805	8.07579
1.84	4.37964	8.09473
1.86	4.37131	8.11365
1.88	4.36307	8.13255
1.9	4.35493	8.15144
1.92	4.34687	8.1703
1.94	4.3389	8.18914
1.96	4.33101	8.20797
1.98	4.32321	8.22678
2	4.31548	8.24556

**Table C.14** Selectivity CO<sub>2</sub>:CH<sub>4</sub> Data for tbo-acetamide

Total pressure (bar)	Selectivity CO <sub>2</sub> :CH <sub>4</sub> (50:50 mixture)	Selectivity CO <sub>2</sub> :CH <sub>4</sub> (5:95 mixture)
0.02	5.23528	5.58062
0.04	5.05251	5.56541
0.06	4.91713	5.56168
0.08	4.8071	5.56398
0.1	4.71355	5.57014
0.12	4.63181	5.57904
0.14	4.55906	5.58999
0.16	4.49343	5.60255
0.18	4.43363	5.61639
0.2	4.37868	5.6313
0.22	4.32787	5.64709
0.24	4.28063	5.66365
0.26	4.23649	5.68085
0.28	4.1951	5.69861
0.3	4.15614	5.71686
0.32	4.11937	5.73554
0.34	4.08457	5.75461
0.36	4.05155	5.77402
0.38	4.02015	5.79372
0.4	3.99025	5.8137
0.42	3.9617	5.83393
0.44	3.93442	5.85437
0.46	3.9083	5.87501
0.48	3.88327	5.89583
0.5	3.85924	5.91682
0.52	3.83615	5.93795
0.54	3.81394	5.95921
0.56	3.79255	5.9806
0.58	3.77193	6.00209
0.6	3.75204	6.02369
0.62	3.73284	6.04538
0.64	3.71428	6.06715
0.66	3.69634	6.08899
0.68	3.67897	6.11091
0.7	3.66216	6.13289
0.72	3.64586	6.15492
0.74	3.63006	6.177
0.76	3.61474	6.19913
0.78	3.59986	6.2213

**Table C.14** Continued

0.8	3.58541	6.24351
0.82	3.57138	6.26575
0.84	3.55773	6.28802
0.86	3.54446	6.31031
0.88	3.53155	6.33263
0.9	3.51898	6.35497
0.92	3.50674	6.37732
0.94	3.49482	6.39968
0.96	3.4832	6.42206
0.98	3.47187	6.44445
1	3.46083	6.46684
1.02	3.45005	6.48924
1.04	3.43954	6.51164
1.06	3.42928	6.53404
1.08	3.41925	6.55645
1.1	3.40947	6.57884
1.12	3.3999	6.60124
1.14	3.39056	6.62363
1.16	3.38142	6.64602
1.18	3.37249	6.66839
1.2	3.36376	6.69076
1.22	3.35521	6.71312
1.24	3.34685	6.73547
1.26	3.33867	6.75781
1.28	3.33066	6.78013
1.3	3.32282	6.80244
1.32	3.31514	6.82473
1.34	3.30762	6.84701
1.36	3.30025	6.86927
1.38	3.29303	6.89152
1.4	3.28595	6.91375
1.42	3.27902	6.93596
1.44	3.27222	6.95815
1.46	3.26555	6.98032
1.48	3.25901	7.00248
1.5	3.2526	7.02461
1.52	3.2463	7.04672
1.54	3.24013	7.06881
1.56	3.23407	7.09088
1.58	3.22812	7.11292
1.6	3.22229	7.13495
1.62	3.21656	7.15695
1.64	3.21093	7.17892

**Table C.14** Continued

1.66	3.2054	7.20088
1.68	3.19998	7.22281
1.7	3.19464	7.24471
1.72	3.18941	7.26659
1.74	3.18426	7.28845
1.76	3.17921	7.31028
1.78	3.17424	7.33208
1.8	3.16935	7.35386
1.82	3.16455	7.37561
1.84	3.15984	7.39734
1.86	3.1552	7.41904
1.88	3.15063	7.44072
1.9	3.14615	7.46236
1.92	3.14174	7.48399
1.94	3.1374	7.50558
1.96	3.13313	7.52715
1.98	3.12893	7.54869
2	3.1248	7.5702

**Table C.15** Selectivity CO<sub>2</sub>:CH<sub>4</sub> Data for fmj-methyl

Total pressure (bar)	Selectivity CO <sub>2</sub> :CH <sub>4</sub> (50:50 mixture)	Selectivity CO <sub>2</sub> :CH <sub>4</sub> (5:95 mixture)
0.02	3.7993	3.8286
0.04	3.78787	3.84456
0.06	3.77723	3.86057
0.08	3.76712	3.87662
0.1	3.75741	3.89268
0.12	3.74804	3.90876
0.14	3.73895	3.92484
0.16	3.73012	3.94092
0.18	3.7215	3.957
0.2	3.71308	3.97308
0.22	3.70485	3.98915
0.24	3.69679	4.00522
0.26	3.68889	4.02128
0.28	3.68113	4.03734
0.3	3.67352	4.05339

**Table C.15** Continued

0.32	3.66604	4.06943
0.34	3.65869	4.08546
0.36	3.65146	4.10148
0.38	3.64434	4.11749
0.4	3.63734	4.13349
0.42	3.63043	4.14948
0.44	3.62364	4.16546
0.46	3.61694	4.18143
0.48	3.61033	4.19739
0.5	3.60381	4.21334
0.52	3.59739	4.22927
0.54	3.59105	4.2452
0.56	3.58479	4.26111
0.58	3.57861	4.27701
0.6	3.57251	4.2929
0.62	3.56649	4.30878
0.64	3.56054	4.32464
0.66	3.55467	4.34049
0.68	3.54886	4.35633
0.7	3.54312	4.37216
0.72	3.53745	4.38798
0.74	3.53185	4.40378
0.76	3.5263	4.41957
0.78	3.52083	4.43535
0.8	3.51541	4.45111
0.82	3.51005	4.46686
0.84	3.50475	4.4826
0.86	3.4995	4.49833
0.88	3.49431	4.51404
0.9	3.48918	4.52975
0.92	3.4841	4.54543
0.94	3.47907	4.56111
0.96	3.4741	4.57677
0.98	3.46917	4.59242
1	3.4643	4.60806
1.02	3.45947	4.62368
1.04	3.45469	4.63929
1.06	3.44996	4.65489
1.08	3.44527	4.67048
1.1	3.44063	4.68605
1.12	3.43603	4.70161
1.14	3.43148	4.71716
1.16	3.42697	4.73269

**Table C.15** Continued

1.18	3.4225	4.74821
1.2	3.41807	4.76372
1.22	3.41369	4.77921
1.24	3.40934	4.79469
1.26	3.40503	4.81016
1.28	3.40076	4.82562
1.3	3.39654	4.84106
1.32	3.39234	4.85649
1.34	3.38819	4.8719
1.36	3.38407	4.88731
1.38	3.37999	4.9027
1.4	3.37594	4.91808
1.42	3.37193	4.93344
1.44	3.36795	4.94879
1.46	3.36401	4.96413
1.48	3.3601	4.97946
1.5	3.35622	4.99477
1.52	3.35237	5.01007
1.54	3.34856	5.02536
1.56	3.34478	5.04063
1.58	3.34103	5.05589
1.6	3.33731	5.07114
1.62	3.33362	5.08638
1.64	3.32996	5.1016
1.66	3.32633	5.11681
1.68	3.32273	5.13201
1.7	3.31915	5.14719
1.72	3.31561	5.16236
1.74	3.31209	5.17752
1.76	3.3086	5.19266
1.78	3.30514	5.2078
1.8	3.30171	5.22292
1.82	3.2983	5.23802
1.84	3.29491	5.25312
1.86	3.29156	5.2682
1.88	3.28823	5.28327
1.9	3.28492	5.29833
1.92	3.28164	5.31337
1.94	3.27838	5.3284
1.96	3.27515	5.34342
1.98	3.27194	5.35842
2	3.26876	5.37342

**Table C.16** Selectivity CO<sub>2</sub>:CH<sub>4</sub> Data for fmj-ethyl

Total pressure (bar)	Selectivity CO <sub>2</sub> :CH <sub>4</sub> (50:50 mixture)	Selectivity CO <sub>2</sub> :CH <sub>4</sub> (5:95 mixture)
0.02	4.48241	4.59357
0.04	4.41543	4.59442
0.06	4.3616	4.59781
0.08	4.31525	4.60261
0.1	4.27398	4.60834
0.12	4.2365	4.61476
0.14	4.202	4.62171
0.16	4.16993	4.62908
0.18	4.1399	4.6368
0.2	4.11162	4.64482
0.22	4.08484	4.65308
0.24	4.05941	4.66156
0.26	4.03517	4.67023
0.28	4.01199	4.67907
0.3	3.98979	4.68805
0.32	3.96846	4.69717
0.34	3.94794	4.70641
0.36	3.92817	4.71576
0.38	3.90908	4.72521
0.4	3.89064	4.73475
0.42	3.87278	4.74438
0.44	3.85549	4.75408
0.46	3.83871	4.76384
0.48	3.82243	4.77368
0.5	3.80661	4.78357
0.52	3.79122	4.79352
0.54	3.77625	4.80352
0.56	3.76167	4.81357
0.58	3.74745	4.82366
0.6	3.7336	4.8338
0.62	3.72007	4.84397
0.64	3.70687	4.85418
0.66	3.69398	4.86442
0.68	3.68138	4.8747
0.7	3.66906	4.885
0.72	3.65701	4.89534
0.74	3.64521	4.90569
0.76	3.63367	4.91608
0.78	3.62236	4.92648

**Table C.16** Continued

0.8	3.61129	4.93691
0.82	3.60043	4.94736
0.84	3.58979	4.95782
0.86	3.57935	4.9683
0.88	3.56911	4.9788
0.9	3.55906	4.98932
0.92	3.5492	4.99985
0.94	3.53951	5.01039
0.96	3.53	5.02095
0.98	3.52066	5.03151
1	3.51148	5.04209
1.02	3.50246	5.05268
1.04	3.49359	5.06328
1.06	3.48487	5.07389
1.08	3.47629	5.0845
1.1	3.46785	5.09512
1.12	3.45955	5.10575
1.14	3.45138	5.11639
1.16	3.44334	5.12703
1.18	3.43543	5.13768
1.2	3.42763	5.14833
1.22	3.41996	5.15899
1.24	3.4124	5.16965
1.26	3.40495	5.18032
1.28	3.39762	5.19098
1.3	3.39039	5.20166
1.32	3.38326	5.21233
1.34	3.37624	5.22301
1.36	3.36931	5.23368
1.38	3.36249	5.24436
1.4	3.35575	5.25504
1.42	3.34911	5.26572
1.44	3.34256	5.27641
1.46	3.3361	5.28709
1.48	3.32973	5.29777
1.5	3.32344	5.30845
1.52	3.31723	5.31913
1.54	3.31111	5.32981
1.56	3.30506	5.34049
1.58	3.29909	5.35117
1.6	3.2932	5.36185
1.62	3.28738	5.37253
1.64	3.28163	5.3832

**Table C.16** Continued

1.66	3.27595	5.39387
1.68	3.27035	5.40454
1.7	3.26481	5.41521
1.72	3.25934	5.42588
1.74	3.25394	5.43654
1.76	3.2486	5.4472
1.78	3.24332	5.45786
1.8	3.23811	5.46851
1.82	3.23296	5.47917
1.84	3.22786	5.48981
1.86	3.22283	5.50046
1.88	3.21785	5.5111
1.9	3.21293	5.52174
1.92	3.20807	5.53237
1.94	3.20325	5.543
1.96	3.1985	5.55363
1.98	3.19379	5.56425
2	3.18914	5.57486

**Chapter 6: Adjusting Hydrothermal Stability via Functionalization of BTC****Precursors****Table C.17** Water Adsorption and Desorption Data for tbo-bromo

Adsorption		Desorption	
Humidity	Uptake (mmol/g)	Humidity	Uptake (mmol/g)
0	0	0.89408	24.55194
0.10631	13.89296	0.7956	24.29885
0.20489	19.66352	0.5988	23.73832
0.30344	19.07317	0.40178	22.89876
0.40185	19.60135	0.20496	20.69195
0.50025	20.03051	0	0.17729
0.59874	20.52664		
0.69713	21.91853		
0.79551	23.21351		
0.89408	24.55194		

**Table C.18** Water Adsorption and Desorption Data for tbo-acetamide

Adsorption		Desorption	
Humidity	Uptake (mmol/g)	Humidity	Uptake (mmol/g)
0	0	0.89394	21.31385
0.10636	13.37578	0.7956	20.61254
0.20501	11.74502	0.59876	16.97827
0.30337	12.396	0.4018	13.64475
0.4019	12.92013	0.20503	12.79983
0.50019	13.49527	0	1.89134
0.59876	14.17984		
0.69727	17.84143		
0.7956	20.23377		
0.89394	21.31385		

**Table C.19** Water Adsorption and Desorption Data for fmj-methyl

Adsorption		Desorption	
Humidity	Uptake (mmol/g)	Humidity	Uptake (mmol/g)
0	0	0.83931	11.21494
0.11266	6.9889	0.79109	11.60405
0.20951	7.81622	0.59719	11.43521
0.3065	8.44308	0.40337	11.1122
0.40361	8.90738	0.20936	10.49294
0.50033	9.60769	0	5.03247
0.59717	10.89728		
0.69425	10.92984		
0.79103	11.1029		
0.83931	11.21494		

**Table C.20** Water Adsorption and Desorption Data for fmj-ethyl

Adsorption		Desorption	
Humidity	Uptake (mmol/g)	Humidity	Uptake (mmol/g)
0	0	0.83943	11.80056
0.1128	6.06051	0.79081	11.69232
0.2095	7.26016	0.59699	11.30727
0.30657	7.84406	0.40345	10.90184
0.4035	8.52667	0.20945	9.88512
0.50029	9.05244	0	4.26436
0.59702	9.65687		
0.69421	9.87997		
0.79109	11.57942		
0.83943	11.80056		

**Table C.21** Water Adsorption Data for fmj-methoxy

Humidity	Uptake (mmol/g)
0	0
0.10629	5.59259
0.20492	6.73071
0.30346	7.39502
0.40186	7.99147
0.50032	8.57741
0.59868	8.89105
0.69721	9.45602
0.7957	9.67319
0.89399	10.45571